IPP-Report

Max-Planck-Institut
für Plasmaphysik

Henning Thomsen

A Dynamics Investigation into Plasma Edge Turbulence

IPP 15/1
Juli 2002

A Dynamics Investigation into Edge Plasma Turbulence

Reprint of the

INAUGURALDISSERTATION

zur

Erlangung des akademischen Grades eines

doctor rerum naturalium (Dr. rer. nat.)

der

Mathematisch-Naturwissenschaftlichen Fakultät

der

Ernst-Moritz-Arndt-Universität Greifswald

vorgelegt von
Henning Thomsen

Greifswald, im Januar 2002

Minor typesetting changes made with respect to the original.
See also: http://web.ub.uni-greifswald.de/eDiss/2002/6/index.html

Preface: Controlled nuclear fusion

The long term goal of the research on controlled nuclear fusion is to provide a facility in which exothermal nuclear fusion reactions can take place and, in the longer term, to open a technical solution to a new source of energy with large and widely spread resources and the prospect of safe and clean energy production.

Subsequently, the aims of the ongoing nuclear fusion research will briefly be described. For a more detailed introduction, the reader is referred to the standard topical literature: [Kadomtsev 1992; Harms et al. 2000; Gross 1984; Teller 1981; Pinkau and Schumacher 1982].

The fusion of two nuclei can release a large amount of energy, provided that the sum of masses of the reacting nuclei is larger than the sum of masses of the produced nuclei (the mass defect Δm leads to a release of binding energy $\Delta E = \Delta m c^2$). The reaction between two hydrogen isotopes deuterium (D) and tritium (T)

$$ {}^{2}_{1}\mathrm{D} + {}^{3}_{1}\mathrm{T} \rightarrow {}^{4}_{2}\mathrm{He}\,(3.5\,\mathrm{MeV}) + {}^{1}_{0}\mathrm{n}\,(14.1\,\mathrm{MeV}) \tag{0.1} $$

is regarded as most suitable for energy production technology. The essential condition for fusion reactions is a sufficiently high kinetic energy of the reacting species in order to overcome (tunnel through) the Coulomb barrier.

Achieving a positive energy balance between the energy released by the fusion reactions and the energy needed for maintaining these reactions is very difficult. The thermonuclear fusion is regarded as a promising way to reach this goal. A deuterium and tritium plasma (D-T plasma) is heated to a temperature of $10\,\mathrm{keV} \approx 10^8\,\mathrm{K}$. This is about the optimal temperature for the fusion reaction Eq. (0.1). In order to reach a positive energy balance, enough reactions have to take place (high density) and the heat insulation of the plasma has to be as high as possible (long energy confinement time). The product of density n and energy confinement time τ_E must be larger than

$$ n \cdot \tau_E > 10^{20}\,\mathrm{sm}^{-3}. \tag{0.2} $$

This is known as the Lawson criterion Wesson [1997]. The maximum achievable densities at high temperatures are in the order of $10^{20}\,\mathrm{m}^{-3}$ and the energy confinement time must be $\tau_E > 1\,\mathrm{s}$. Once the fusion reaction is started, the D-T plasma is heated by the alpha-particles produced in the reaction. The process is self-sustained as long as deuterium and tritium fuel is provided and the helium ash is removed.

The hot plasma must be confined in a way that the Lawson criterion is fulfilled. A particularly good confinement is possible within specific magnetic configurations like tokamaks and stellarators.A present drawback of these magnetic configurations lies in the fact, that the confinement times are much lower (by a factor of 10–100) than expected from diffusion theory. An enhanced particle and energy transport, the anomalous transport, is observed in the experiment, which nowadays is attributed to the turbulent processes in the plasma (at least for the plasma boundary). The underlying physics of this turbulence is far from being completely identified and this field is a vital research area.

This thesis is intended to contribute to the basic understanding of the turbulent processes in tokamaks and stellarators from the experimental point of view. Due to the strong toroidal magnetic fields in tokamaks and stellarators, the turbulent dynamics has a strong asymmetry parallel (toroidal) versus perpendicular (poloidal and radial) direction. The main focus of this work is concentrated on the turbulent dynamics parallel to the magnetic field, where until now only a small data basis exists, especially for very long scale lengths in the order of tens of meters.

Contents

1. Introduction: Essentials

Firstly, the principles of magnetic confinement in tokamaks and stellarators are introduced in Section 1.1. The role of the plasma boundary and the turbulent transport is briefly reviewed in Section 1.2. An introduction to drift wave turbulence theory is given in Section 1.3 and means of active control of plasma edge turbulence is discussed in Section 1.4. The further outline of this thesis is presented in Section 1.5.

1.1. The magnetic configuration in stellarators and tokamaks

To protect the hot plasma from cooling down and the plasma facing materials from melting, an excellent thermal insulation is required. A particularly good and efficient insulation is achieved by the confinement of the plasma in a magnetic field. The principle of the magnetic confinement of a plasma is based on the fact that in a magnetic field, the Lorentz force restricts the motion of charged particles perpendicular to the magnetic field. Charged particles with a perpendicular velocity component are forced to gyro motion. However, particles can still move freely parallel to the magnetic field. In order to avoid end losses by particles flowing along the magnetic field lines towards a solid boundary, a configuration with closed magnetic field lines seems to be most appropriate. Magnetic configurations in which the field lines do not enter or leave the plasma confinement region are called closed field line configurations. The simplest closed magnetic system is obtained by bending the field lines to a torus. However, the plasma confinement in such a simple magnetized torus is not stable since curvature and a radial magnetic field gradient is introduced (as a result of Maxwell's equations). These terms lead to the well-known charge-separating curvature drift and $\nabla\mathbf{B}$ drift. As a result a vertical electrical field is generated. This electric field is perpendicular to the magnetic field and therefore the $\mathbf{E} \times \mathbf{B}$-force moves the plasma outwards.

It is possible to avoid the vertical electric field by twisting the magnetic field lines in poloidal direction (see Fig. 1.1). (Pfirsch-Schlüter) currents parallel to the magnetic field balance the charge accumulation and the plasma is confined. A measure for the twist of the magnetic field lines is the rotational transform ι

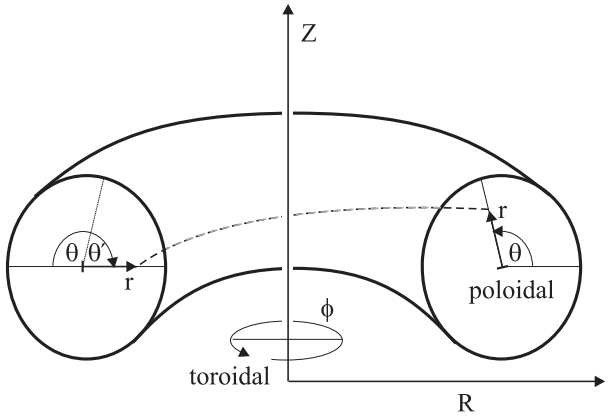

Figure 1.1.: *The toroidal coordinates (r, ϕ, θ) and the cylindrical coordinates (R, ϕ, Z) for a toroidal device. The dashed line illustrates the effect of a rotational transform with $\iota = \theta'/\pi$ on a magnetic field line during a half toroidal circulation.*

that is defined by the poloidal turn θ_N made by a magnetic field line during N revolutions in toroidal direction divided by the toroidal angle:

$$\iota = \lim_{N\to\infty} \frac{\theta_N}{2\pi N}. \tag{1.1}$$

Generally, $\iota = \iota(r)$ is a function of the minor radius r. Often, only the central value of the rotational transform $\iota(0) = \iota_0$ is quoted. The (global) magnetic shear s is defined as

$$s(r) = \frac{r}{\iota}\frac{d}{dr}\iota(r). \tag{1.2}$$

For non-rational ι one single field line ergodically covers a surface, the magnetic flux surface. The magnetic surfaces are radially nested so that no field line connects the inner plasma with the surrounding walls.

Plasmas in closed magnetic field configurations generally consist of two distinct regions, the plasma core (or confinement zone), where the magnetic flux surfaces are closed and the plasma edge (or scrape-off layer), where the magnetic field lines are intersected by solid material like a limiter or the wall of the vacuum vessel (cf. Sec. 1.2). The junction between these two regions is called last closed magnetic flux surface (LCFS). The plasma boundary is not uniquely defined in the literature. In this work the term plasma boundary is used to describe the region from the outer 1—2 cm of the plasma core to the outer scrape-off layer.

Many different concepts exist for the realization of a confinement by closed magnetic configurations [Teller 1981; Gross 1984; Harms et al. 2000]. The two most advanced approaches for magnetically confined plasmas are the tokamak and the stellarator.

1.1.1. Tokamaks

In the tokamak concept, the toroidal magnetic field is provided by coils arranged around the torus, whereas the poloidal component is generated by a large toroidal current flow in the plasma. The tokamak principle has been used successfully in magnetic fusion research during the last few decades [Wesson 1997]. Many tokamak devices with different sizes exist worldwide. The required toroidal currents (for large tokamak devices this current is in the order of 10 MA) is inductively produced. The plasma acts as the secondary winding of a transformer and a current ramp in the primary transformer winding induces a constant loop voltage around the torus which drives the current. Since the induced voltage is based on a temporal change in magnetic flux produced by the current ramp in the primary winding, a DC-current can only be provided for a limited time. However, other methods of driving a plasma current are an area of current research [Fisch 1987; Kikuchi 1993].

The large current in tokamak plasmas provides a source of free energy for instabilities, which grow most easily at magnetic surfaces with rational values of the rotational transform. One of such a magneto-hydrodynamic (MHD) instability is the ideal kink-type instability which is capable of terminating the plasma confinement (low-q disruption [Wesson 1997, Sec. 7.8]) . In order to avoid this instability the safety factor $q = 1/\iota$ should fulfill the Kruskal-Shafranov criterion: $q \geq 1$ in the center of the plasma and $q \geq 2.5$ at the edge of the plasma. For the plasma boundary the value of the safety factor q_{95} at 95% of the closed magnetic flux surfaces is usually considered as a good measure for local changes in the magnetic configuration. Another instability connected to the plasma current is the vertical instability. It cannot be avoided in non-circular, elongated plasma shapes and a feedback stabilization is necessary. This instability will be covered in more detail in Sec. 3.5.2.

The tokamak line has been very successful over the past years and these devices are the most advanced for thermonuclear fusion research. The largest tokamak is the Joint European Torus (JET), which has a major radius of 2.96 m, toroidal magnetic fields up to 3.4 T, plasma currents of up to 4.8 MA. During the deuterium-tritium campaign 1997, peak fusion powers of up to 16 MW (a record in fusion generated power) were reached [Keilhacker et al. 1999]. The poloidal plane of the JET tokamak is shown below in Fig. 1.3b.

1.1.2. Stellarators

In the stellarator concept [Spitzer 1981; Boozer 1998; Wakatani 1998] the magnetic configuration is produced by external coils only. An intrinsic feature of this concept is the possibility of steady state operation. In contrast to tokamaks current disruptions do not occur due to the lack of current-driven plasma insta-

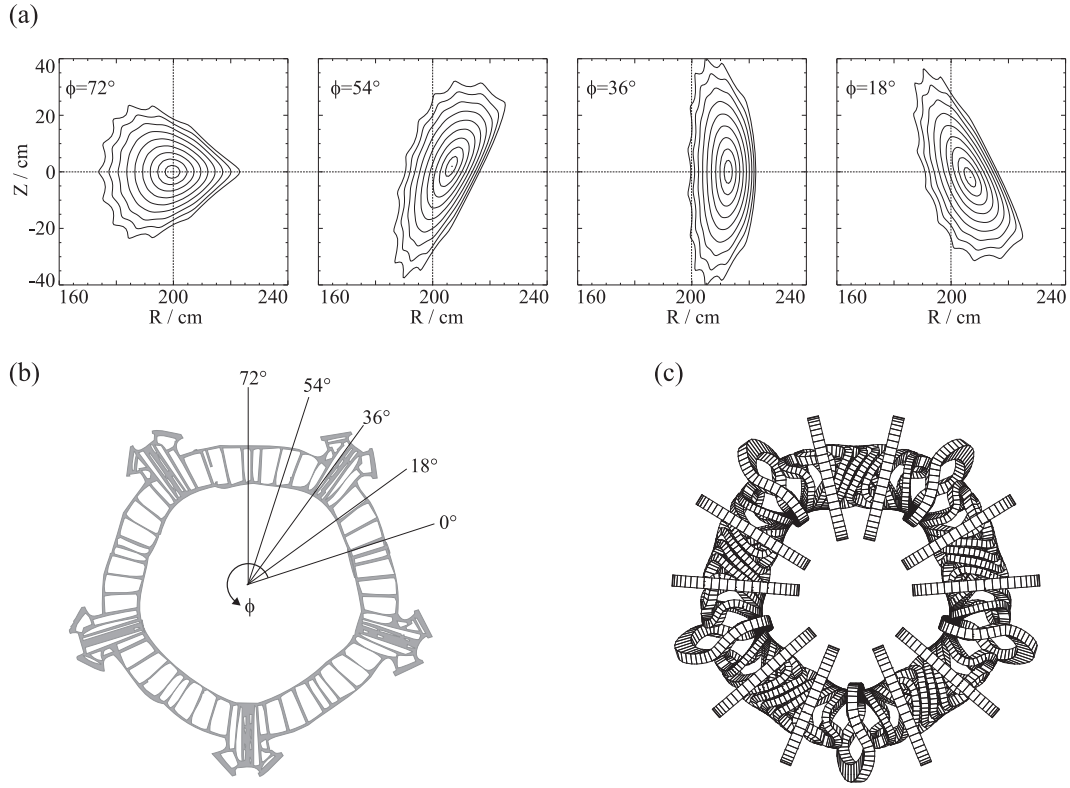

Figure 1.2.: *(a) Poloidal cuts through magnetic flux surfaces at the toroidal angles $\phi = 72°, 54°, 36°, 18°$ on the Wendelstein 7-AS stellarator. Due to the toroidal five-period symmetry, the flux surfaces are identical for a shift in toroidal angle by integer multiples of $\Delta\phi = 72°$. (b) Top view on W7-AS with the positions of the poloidal cuts from (a). (c) The 45 non-planar and 10 planar coils that generate the magnetic confinement field in W7-AS.*

bilities. The helical twist of the magnetic field lines can either be provided by pairs of helically wound coils around the torus (Wendelstein 7-A, LHD), or by a modular coil system (Wendelstein 7-AS, Wendelstein 7-X) [Wakatani 1998].

The magnetic field geometry (and thus the plasma shape) in stellarators is generally more complicated than the geometry in the axially symmetric tokamaks. In particular, the geometry of the poloidal cross sections varies strongly along a toroidal circumfence. Poloidal cuts through magnetic flux surfaces for different toroidal positions are shown in Fig. 1.2 for the Wendelstein 7-AS stellarator (W7-AS). Since poloidal sections of the magnetic surfaces have a non-circular shape, it is useful to introduce an effective radius r_{eff}. The effective radius is defined as the radius, which the respective flux surface would have in an ideal torus with the same volume and aspect ratio (the latter defined as the ratio between major and minor radius).

The perturbation of axial as well as helical symmetry in stellarators leads to the formation of magnetic islands. In a stellarator with m periods (W7-AS has $m = 5$) the perturbation in the magnetic field is m-periodic. This leads to a break-up of the magnetic flux surfaces at radii with a resonant rotational transform $\iota = m/n$ (with n a small integer). The plasma degenerates at these positions into helical filaments, called magnetic islands. The largest islands are those with the lowest values of n and m.

On the W7-AS 45 non-planar coils for the confining magnetic field and 10 additional planar coils for superimposing a purely toroidal field are installed [see Fig. 1.2(c)]. The non-planar coils create a magnetic field with rotational transform $\iota_0 = 0.398$ at the effective radius $r_{eff} = 0$ (ι_0: central rotational transform). The superposition of the toroidal field allows to scan the central rotational transform over a relatively large range, $\iota_0 = [0.25 \cdots 0.9]$. The variation of ι_0 causes a variation of the edge magnetic field topology as well. For $\iota_0 \geq 0.5$ magnetic islands are created in the plasma edge and consequently the effective plasma radius is reduced.

1.2. Plasma boundary physics

For magnetic confinement fusion, the plasma boundary is of great importance since particles and energy are constantly transported radially outward from the core plasma into the plasma boundary. The physical background for these transport processes are illuminated in Sec. 1.2.2. Plasma boundary physics is an extremely wide area. For the tokamak configuration, and comprehensive overview is given in the book written by Stangeby [2000].

1.2.1. The plasma boundary

Due to the particle and energy out-flux from the plasma core, severe requirements arise for the plasma boundary. The plasma boundary should provide a sink for the alpha particle exhaust from the fusion reaction and prevent the plasma core from infiltration of edge impurities which are created by particle bombardment of the target plates. Both, the impurities and the helium ash can severely degrade the quality of the confinement if their concentration in the core plasma is too high [Kadomtsev 1992, Sec. 3.10]. Furthermore, a large percentage (in the order of 10%) of the energy from the fusion reaction is carried through the scrape-off layer towards plasma facing components.

Generally, two concepts are common to define the scrape-off layer: One possibility is the introduction of a solid material into the plasma which is capable of withstanding the heat load. This concept is called a limiter configuration. Another possibility is to reshape the plasma cross-section by additional magnetic

fields which permits a larger separation between solid materials and the core plasma. This is the divertor configuration. Both concepts are described in some more detail below.

In Fig. 1.3(a), a sketch of a simplified plasma boundary layer is shown. The transport physics in the scrape-off layer (SOL) is largely determined by the distance between the two plasma contactors along a magnetic field line (this distance is referred to as connection length), since the particle dynamics parallel to the magnetic field lines is generally orders of magnitude larger than the dynamics perpendicular to the magnetic field. The width of the SOL is determined by the ratio between parallel and radial transport of particles and energy. Experimentally, the SOL width is found to be of the order of 1—2 cm for most tokamaks and stellarators. In real tokamak or stellarator geometry, the detailed physics is generally very complicated, and a noteworthy fact is that the connection length can differ severely in the scrape-off layer.

A sketch of the poloidal plane of the JET tokamak is shown in Fig. 1.3(b). The field lines are diverted by currents through external toroidal coils. In the poloidal plane the magnetic field lines have a figure-eight shape. The X-point is the location in the poloidal plane where the poloidal magnetic field vanishes. The (magnetic) separatrix is the magnetic flux surface passing through the X-point. This divertor configuration has some advantages over the limiter configuration:

1. The heat load from the core plasma can be distributed over a larger area. Hence, the erosion of the target plates and therefore the impurity influx is reduced.

2. Due to the distance between the target plates and the bulk plasma introduced by the diversion of the field lines, the impurity flux into the core plasma is further reduced.

3. Ions and especially the alpha particles from the fusion reaction are neutralized at the target plates. The divertor region can be pumped in order to remove the neutralized helium (from the fusion reaction) and neutral impurities.

1.2.2. Transport in the plasma boundary

Different models apply for particle and heat transport parallel and perpendicular to the magnetic field. The transport along the magnetic field lines is determined by the thermal speed of the species and Coulomb collisions. The parallel transport and sheath physics is dicussed in Sec. 2.1.

The radial transport in magnetically confined plasmas can be divided into three contributions, classical, neoclassical and the anomalous diffusion. For a review of classical diffusion in homogenous magnetic fields and neoclassical diffusion in

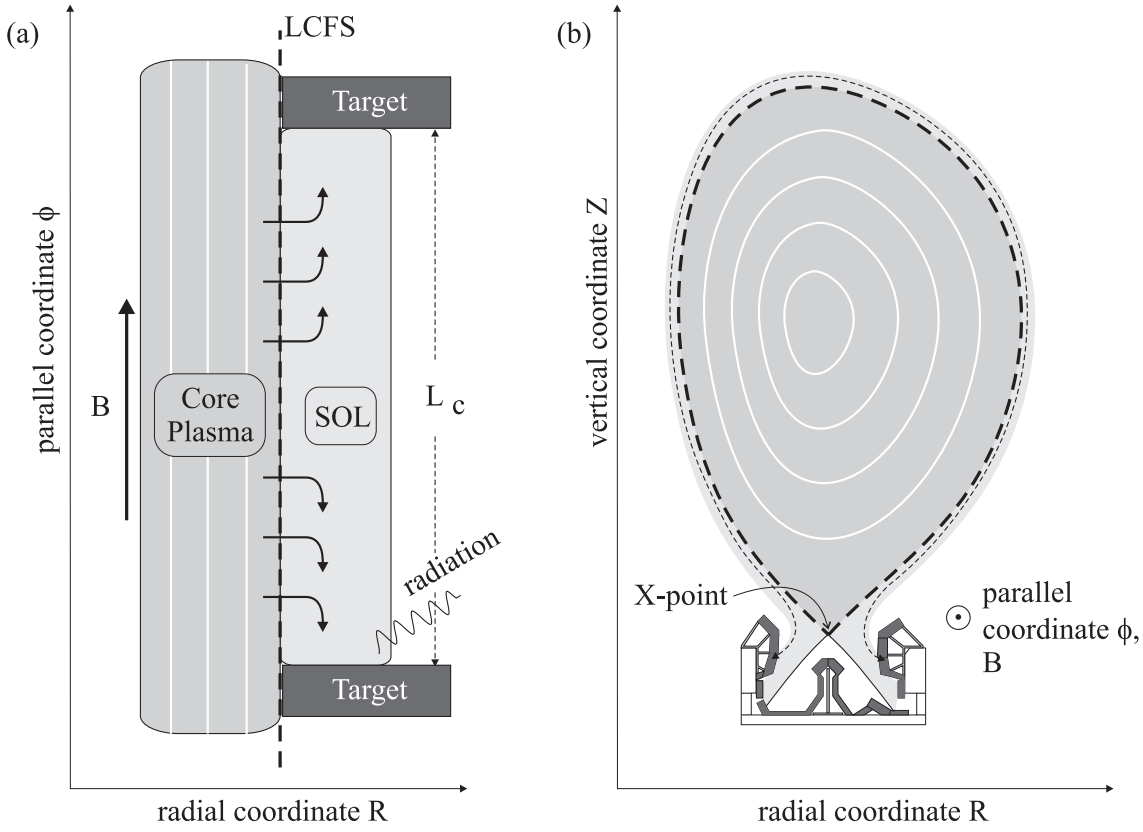

Figure 1.3.: *(a) A simplified (slab) geometry for the transport physics in the plasma boundary and (b) a sketch of the poloidal plane of the actual geometry for the JET tokamak with Mark II Gas-Box divertor. The magnetic flux surfaces (white) in the core plasma (dark grey) have no contact to any solid material. The outward transport of particles and energy in this region with closed magnetic flux surfaces is determined by the radial transport and recombination radiation. The last closed flux surface (LCFS, dashed line) indicates the junction between the core plasma and the scrape-off layer (SOL, light grey). In the SOL the magnetic field lines start and end on the inner and outer target plates. Following the magnetic field, the distance between the inner and outer plates plates is the connection length L_c (at JET: $L_c \approx 66$ m for an edge safety factor $q_{95} \approx 2.7$).*

toroidal magnetic configurations, see Refs. [Wagner 1994; Hinton and Hazeltine 1976]).

Generally, the radial transport in the plasma boundary is found to be much larger than predicted by classical or neoclassical diffusion. The missing contribution is referred to as anomalous diffusion. A self-consistent physical picture of anomalous transport is still missing. However, it is now widely accepted, that anomalous transport can be attributed to turbulent fluctuations in plasma parameters, in particular in plasma potential, density, temperature and magnetic field [Liewer 1985; Wagner and Stroth 1993; Hidalgo 1995; Bickerton 1997; Endler 1999].

From the theoretical point of view, fluctuations in the plasma parameters can be described by fluctuating electric fields that do not perturb the magnetic configuration (electrostatic turbulence), or by fluctuations in the magnetic field perpendicular to the flux surfaces (magnetic turbulence). In principle, a combination of both is possible as well.

In case of magnetic turbulence, the stochastic radial displacement of the magnetic field lines in conjunction with the parallel electron flow is responsible for an enhanced transport [Bickerton 1997]. Experimentally, magnetic turbulence is found to be important for the perpendicular transport in reversed field pinches [Fiksel et al. 1996]. However, in tokamaks and stellarators electrostatic turbulence is considered to be responsible for the anomalous transport, especially for the plasma edge [Wagner and Stroth 1993; Endler 1999]. Therefore, the present work is restricted to electrostatic turbulence only.

1.2.3. Electrostatic turbulence and transport

The idea behind the electrostatic transport is largely based on $\mathbf{E} \times \mathbf{B}$-drift. The electric field $\mathbf{E}$ is caused by electric potential Φ only, $\mathbf{E} = -\nabla\Phi$, since magnetic fluctuations are not considered, $\nabla \times \mathbf{E} = -\partial\mathbf{B}/\partial t = 0$.

If we assume a potential perturbation Φ that is poloidally and radially localized in a magnetized plasma with a geometry as shown in Fig. 1.4, the plasma in the vicinity of the perturbation rotates around the potential structure in the plane perpendicular to the magnetic field $\mathbf{B}$ due to $\mathbf{E} \times \mathbf{B}$-drift with the velocity

$$\mathbf{v}_E = \frac{-\nabla\Phi \times \mathbf{B}}{B^2}. \tag{1.3}$$

If the potential $\Phi(t)$ is time-dependant (i.e. fluctuating), the corresponding $\mathbf{E} \times \mathbf{B}$-drift velocity is fluctuating as well. Let us distinguish between the fluctuating and the stationary part during a time period ΔT. Generally, the observed fluctuations in the plasma boundary of tokamaks and stellarators have frequencies $\omega \ll 1\,\mathrm{MHz}$ and therefore timescales in the order of several μs. ΔT is long

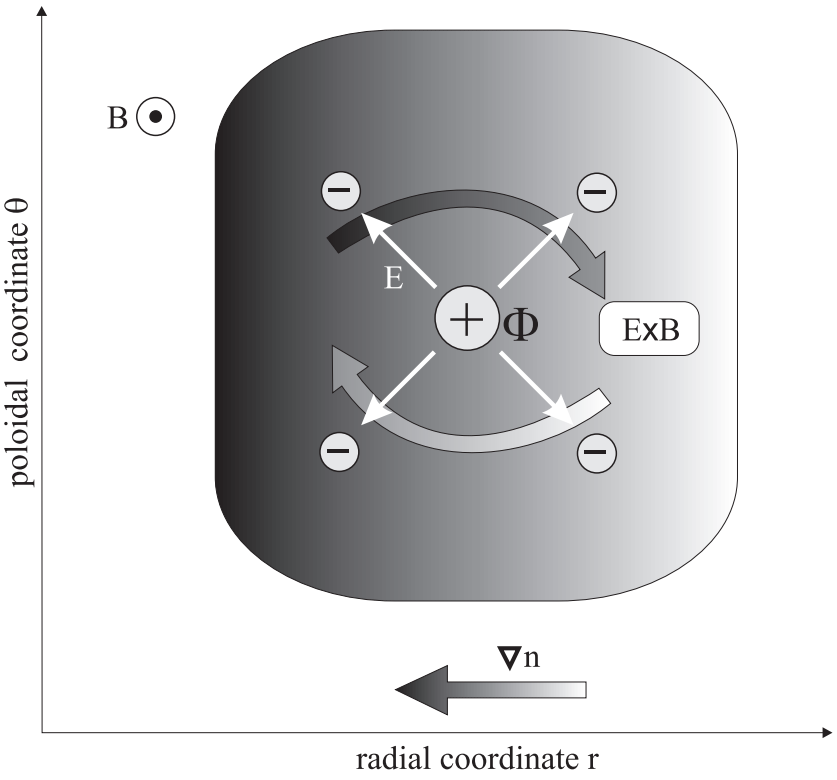

Figure 1.4.: *Sketch of the general idea behind electrostatic transport in magnetized plasmas. The magnetic field* $\mathbf{B}$ *is in toroidal direction (perpendicular to the plane shown). Assuming a positive perturbation in electric potential* Φ*, an electric field* $\mathbf{E} = -\nabla\Phi$ *builds up (white arrows). In conjunction with the magnetic field* $\mathbf{B}$*, the plasma is rotating around the perturbation by the* $\mathbf{E} \times \mathbf{B}$*-drift. Since a radial gradient in the plasma density* ∇n *towards the plasma core is generally present in the plasma boundary, the* $\mathbf{E} \times \mathbf{B}$*-drift is in principle capable of net plasma transport that flattens the gradient, provided that the local plasma rotation ends after approximately one half turn.*

compared to the timescale of the fluctuations. The mean value of the potential $\Phi(t)$, denoted by $\langle\Phi\rangle$, is given by

$$\langle\Phi\rangle = \frac{1}{\Delta T}\int_0^{\Delta T} \Phi(t)\,dt\,, \tag{1.4}$$

and the fluctuating part $\tilde{\Phi}$ of the potential is

$$\tilde{\Phi} \equiv \Phi(t) - \langle\Phi\rangle\,. \tag{1.5}$$

Let us now consider the transport that is associated with the fluctuating part of the potential. The particle and energy flux, $\tilde{\mathbf{\Gamma}}$ and $\tilde{\boldsymbol{Q}}$, respectively, are given by the equations [Ross 1989]

$$\tilde{\mathbf{\Gamma}} = n\tilde{\mathbf{v}}_E \tag{1.6}$$

$$\tilde{\boldsymbol{Q}} = \frac{3}{2}k_B T n\tilde{\mathbf{v}}_{\mathbf{E}}\,, \tag{1.7}$$

where k_B is Boltzmann's constant. The plasma density and temperature are denoted by n and T, respectively. Since the mean value of $\tilde{\Phi}$ is zero, the mean of the associated $\mathbf{E}\times\mathbf{B}$-velocity $\langle\tilde{\mathbf{v}}_E\rangle = \langle -(\nabla\tilde{\Phi}\times\mathbf{B})/B^2\rangle$ is zero as well. Moreover, for stationary density ($n \equiv \langle n\rangle$) and temperature ($T \equiv \langle T\rangle$) there are no net (i.e. average) particle and energy fluxes $\langle\tilde{\mathbf{\Gamma}}\rangle$ and $\langle\tilde{\mathbf{Q}}\rangle$ associated with the potential fluctuations. Non-vanishing average fluxes are only possible for the case that density and temperature have a fluctuating component, which is correlated with the potential fluctuations. The correlation requirements for a net particle transport can obtained by Fourier transform of $n(t)$ and $\Phi(t)$ [Powers 1974],

$$\langle\tilde{\Gamma}_\omega\rangle \propto \gamma_{n\Phi}(\omega)\sin[\alpha(\omega)]\,n_0\,\Phi_0\,. \tag{1.8}$$

$\tilde{\Gamma}_\omega$ is the contribution to the fluctuation induced flux for a single frequency component ω. n_0 and Φ_0 are the root mean values of the density and the potential, respectively. The cohereny $\gamma_{n\Phi}(\omega)$ and the phase $\alpha(\omega)$ between the density and potential fluctuations at this frequency are important for the associated transport[1]. Maximum radial transport is obtained for maximum coherency $\gamma_{n\Phi}^{max}(\omega) = 1$ and a phase of $\alpha_{max}(\omega) = \pi/2$ between density and potential fluctuations. In App. A.1 the calculation is shown for linear waves. Similar conditions apply for the maximum energy transport. However, the situation is more complicated since the product of three fluctuating parts yield the energy flux. This issue is discussed in more detail in Ref. [Pfeiffer et al. 1998].

Sometimes, the fluctuation-induced radial particle transport is described as a diffusive process [Liewer 1985],

$$\langle\tilde{\Gamma}_r\rangle = -D_\perp\left(\nabla\langle n\rangle\right)_r\,. \tag{1.9}$$

[1] Coherency and phase are discussed in more detail in Sec. 2.2.

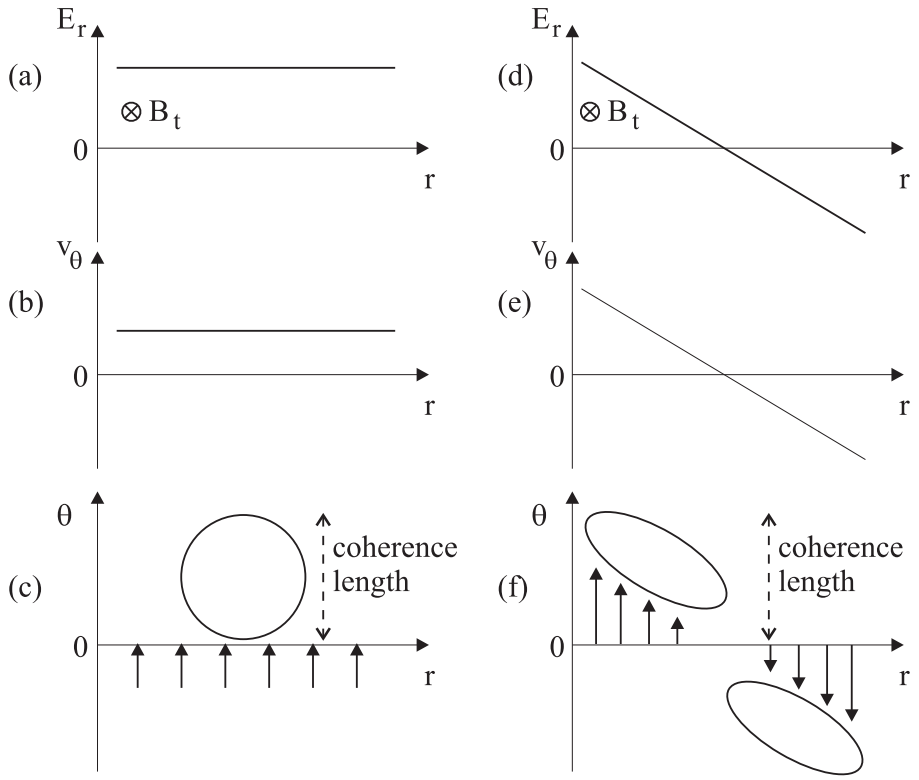

Figure 1.5.: *Effect of velocity shear flow on turbulence. A constant radial electric field E_r in a background toroidal magnetic field B_t(a) leads to a radially constant poloidal* $\mathbf{E} \times \mathbf{B}$*-velocity v_θ (b). A turbulent eddy (shown in the poloidal-radial plane) is moved along in poloidal direction with velocity v_θ (c). For a radially varying electric field (d), the radial profile of the associated poloidal* $\mathbf{E} \times \mathbf{B}$*-velocity is sheared in radial direction (e). Turbulent structures are decorrelated in radial direction and may break up (f).*

The anomalous diffusion coefficient $D_\perp$ is usually a function of the radial position. Note, that the assumption of a diffusive process for the turbulent flux in Eq. (1.9) is only a model construction: The transport associated with electrostatic turbulence is actually of convective nature.

1.2.4. Turbulence suppression by shear flow

The effect of radial electrics field on electrostatic transport was recently found to play a key role for the understanding of improved confinement modes and anomalous transport reduction [Biglari et al. 1990; Itoh and Itoh 1996; Burrell 1997; Terry 2000]. The basic idea is sketched in Fig. 1.5. We consider a coherent vortex structure in the poloidal-radial plane, which is often referred to as a turbulent

eddy, Fig. 1.5(c). The extent in the poloidal-radial plane is given by the cohence length [see Fig. 1.5(c)]. Let us assume the presence of a radial electric field with $E_r(r) \propto r$. Such a field causes a poloidal $\mathbf{E} \times \mathbf{B}$-velocity flow $v_\theta(r) \propto r$ which is sheared in radial direction as shown in Fig. 1.5(d,e). The turbulent eddy is elongated by the shear flow and eventally torn apart, if the poloidal elongation exeeds the coherence length, cf. Fig. 1.5(f). Since the electrostatic transport is greatly affected by the coherence and phase between the density and potential fluctuations, the decorrelation caused by the shear flow can yield a significant reduction of fluctuation induced transport [Burrell 1997].

1.3. Drift wave turbulence theory and simulation

In this section, the model for drift wave turbulence is described. Drift wave turbulence can account for the observed microscopic fluctuations and the anomalous particle and energy transport in the plasma boundary [Horton 1999; Scott 2001].

1.3.1. Linear drift waves

Drift waves generally occur in magnetized plasmas with a pressure gradient perpendicular to the magnetic field. Since this requirement is nearly always met, the drift wave mechanism is often referred to as universal instability. Here, the general mechanism of a linear drift wave is considered for a localized positive potential Φ in the geometry of Fig. 1.4. The drift mechanism is discussed in more detail, e.g. in the books by Chen [1984] and Nishikawa and Wakatani [1999]

Normally, the densities of electrons n_e and ions n_i will self-consistently adjust to the potential Φ due to Poisson's equation

$$\nabla^2 \Phi = -\frac{e}{\epsilon_0}(Z n_i - n_e), \tag{1.10}$$

with ϵ_0 being the dielectric constant and Z denoting the ion charge. In the following, singly charged ions are considered, only ($Z = 1$).

Since the electron mobility parallel to the magnetic field is very high with respect to the slow ion dynamics, the assumptions of a fixed ion background (temperature $T_i = 0$ and parallel velocity $u_i = 0$) and an arbitrarily fast parallel electron dynamics (electron mass $m_e \to 0$) are generally justified. In this approximation, only the electron density is perturbed by the potential and follows a local Boltzmann distribution

$$n_e = n_{e0} \exp\left(\frac{e\Phi}{k_B T_e}\right), \tag{1.11}$$

with the unperturbed density n_{e0} and the electron temperature T_e. For a small potential perturbation Φ_1 (with respect to $k_B T_e/e$), the density perturbation

$n_1 = n_e - n_{e0}$ is small and the linearization of Eq. (1.11) reads to be

$$\frac{n_1}{n_{e0}} = \frac{n_e - n_{e0}}{n_{e0}} = \frac{e\Phi_1}{k_B T_e}. \tag{1.12}$$

Eq. (1.12) is referred to in the literature as the adiabatic electron response. It is assumed, for example, in the renowned drift wave model by Hasegawa and Mima [1977]. Relation (1.12) implies, that the perturbation of the density n_1 is in phase with a perturbation in the electric potential Φ_1. Within the scope of the simple model presented here, Eq. (1.12) essentially describes the parallel electron dynamics.

We consider only perturbations which are small compared to typical length scales of the spatial and temporal slowly changing background. Since the plasma is magnetized, the wave numbers of the perturbations perpendicular ($k_\perp$) and parallel ($k_\parallel$) to the magnetic field show a strong anisotropy,

$$k_\parallel \ll k_\perp \,. \tag{1.13}$$

The perpendicular dynamics is characterized by drifts known from single particle and fluid descriptions of the plasma, as the $\mathbf{E} \times \mathbf{B}$-drift, the diamagnetic drift and the polarization drift [Chen 1984; Goldston and Rutherford 1995]. The gyro-motion of the particles in the magnetic field is neglected. The typical perpendicular spatial scales under consideration are given by the drift scale

$$\rho_s = \frac{\sqrt{m_i T_e}}{eB}\,, \tag{1.14}$$

which is the Larmor radius of ions taken at the electron temperature ($T_i = 0$ was assumed) [Scott 2001]. Moreover, the considered frequencies ω in this drift wave model are small compared to the gyro-frequencies for ions and electrons $\omega \ll \Omega_i \ll \Omega_e$.

The perpendicular drifts are derived from the momentum equations of ions and electrons

$$m_i n_i \left(\frac{\partial}{\partial t} + \mathbf{u}_i \cdot \nabla\right) \mathbf{u}_i = +e n_i \left(-\nabla\Phi + \mathbf{u}_i \times \mathbf{B}\right) \tag{1.15}$$

$$0 = -e n_e \left(-\nabla\Phi + \mathbf{v}_e \times \mathbf{B}\right) - k_B T_e \nabla n_e \,, \tag{1.16}$$

In these equations the temperature contribution to the pressure is neglected for the electrons and the ion pressure $p_i = n k_B T_i$ is zero since we assumed $T_i = 0$. The left hand side of Eq. (1.16) is zero, since electron inertia is neglected. The perpendicular electron dynamics is described by the sum of $\mathbf{E} \times \mathbf{B}$- and diamagnetic drift velocities[2]

$$\mathbf{v}_\perp = \mathbf{v}_E + \mathbf{v}_{de}\,, \tag{1.17}$$

[2]This result is obtained by calculating the cross-product of Eq. (1.16) with $\mathbf{B}$

whereas the perpendicular ion dynamics is described by the sum of $\mathbf{E} \times \mathbf{B}$- and polarization drift velocities

$$\mathbf{u}_\perp = \mathbf{u}_E + \mathbf{u}_{pi} \,. \tag{1.18}$$

The ion diamagnetic drift velocity does not contribute because $p_i = 0$ and the electron polarization drift velocity is zero since $m_e = 0$. If the plasma is quasi-neutral,

$$n \equiv n_e \approx n_i, \tag{1.19}$$

the continuity equations for ions and electrons

$$\frac{\partial n_i}{\partial t} + \nabla \cdot (n_i \, \mathbf{u_i}) = 0 \tag{1.20}$$

$$\frac{\partial n_e}{\partial t} + \nabla \cdot (n_e \, \mathbf{v_e}) = 0 \tag{1.21}$$

can be combined and one gets for the total current density $\mathbf{j} = en(\mathbf{u_i} - \mathbf{v_e})$ the expression

$$0 = \nabla \cdot \mathbf{j} = \nabla_\perp \cdot \mathbf{j}_\perp + \nabla_\parallel \cdot \mathbf{j}_\parallel \,. \tag{1.22}$$

Eq. (1.22) associates the parallel electron dynamics with the perpendicular ion dynamics: The only term contributing to the perpendicular divergence of the total current is the ion polarization velocity:

$$\nabla_\perp \cdot \mathbf{j}_\perp = ne \nabla_\perp \cdot (\mathbf{u}_E - \mathbf{v}_E + \mathbf{u}_{pi} - \mathbf{v}_{de}) = ne \nabla_\perp \cdot \mathbf{u}_{pi}. \tag{1.23}$$

This last equation is valid since the $\mathbf{E} \times \mathbf{B}$-velocities of ions and electrons cancel and the divergence of the electron diamagnetic drift vanishes [Scott 2001]. The parallel dynamics is determined by the electrons only (cf. Eq. 1.12). Hence, Eq. (1.22) describes the coupling between electron and ion dynamics.

From the ion continuity equation [Eq. (1.21)] a dispersion relation for the drift waves can be calculated in Fourier representation when considering linear waves with frequency ω and wave number $\mathbf{k}$. Then, a time derivative in real space corresponds to a multiplication by $i\omega$ in Fourier space, and a spatial derivate corresponds to a multiplication by $i\mathbf{k}$. For simplicity let us consider the $\mathbf{E} \times \mathbf{B}$-velocity only $\mathbf{u}_i = \mathbf{v}_E$. The radial component of $\mathbf{v}_E$ from Eq. (1.3) is $v_r = E_\theta / B_0 = -ik_\theta \Phi / B_0$. Accordingly, Eq. (1.21) reads

$$i\omega n_i - i \frac{k_\theta}{B_0} \frac{d}{dr} (n_i \Phi) = 0 \,. \tag{1.24}$$

With the assumption of quasi neutrality (1.19) and adiabatic electron response (1.12), we obtain as the dispersion relation

$$\omega = k_\theta \frac{k_B T_e}{e n_{e0} B_0} \frac{dn_1}{dr} \equiv k_\theta v_{de} \,, \tag{1.25}$$

with v_{de} being the diamagnetic drift velocity for electrons. Since the frequency ω is real, the wave is linearly stable (no growth or damping). According to Eq. (1.25) linear drift waves propagate with a poloidal phase velocity $v_p \equiv \omega/k_\theta$ equal to the electron diamagnetic velocity. This velocity is slightly altered when further drifts (i.e. the ion polarization drift) in Eq. (1.25) are considered (cf. Ref. Scott [2001]).

Due to the anisotropy caused by the magnetic field, the parallel phase velocity is significantly larger [from Eq. (1.13): $k_\parallel \ll k_\theta$ and hence $v_\parallel = \omega/k_\parallel \gg v_p = \omega/k_\theta$]. Parallel to the magnetic field, drift waves propagate with phase velocities near electron thermal velocity [Nishikawa and Wakatani 1999]. Note that the interaction between the parallel dynamics of the electrons (1.12) and the perpendicular dynamics of the ions (1.18) is the key ingredient to the drift wave dynamics. In case of adiabatic electron response (1.12), $\tilde{\Phi}$ and $\tilde{n}$ are always in phase. Hence, no net transport is connected to the linearly stable drift waves (cf. Sec. 1.2.3)

1.3.2. Instability of drift waves

The simple drift wave model presented above is easily extended by adding non-adiabatic corrections to Eq. (1.12). Non-adiabatic terms $i\delta_k$ give rise to destabilization of the drift waves, since they introduce a phase shift between density and potential

$$\frac{n_1}{n_{e0}} = \frac{e\Phi}{k_B T_e}\left(1 - i\delta_k\right). \tag{1.26}$$

There are a couple of effects that may lead to such non-adiabatic electron dynamics along the magnetic field lines:

- Electron collisions with ions or neutrals (resistivity),
- Kinetic effects (Landau damping),
- Coupling to shear Alfvén waves,
- Particle trapping in magnetic wells,
- Finite ion radius,
- Magnetic field curvature.

It can be shown that drift waves are stabilized in slab geometry by magnetic shear [Ross and Mahajan 1978; Tsang et al. 1978; Gudzar et al. 1978] and it was discussed in the literature whether the contribution of (linearly unstable) drift wave turbulence to the anomalous transport in the plasma edge can be significant

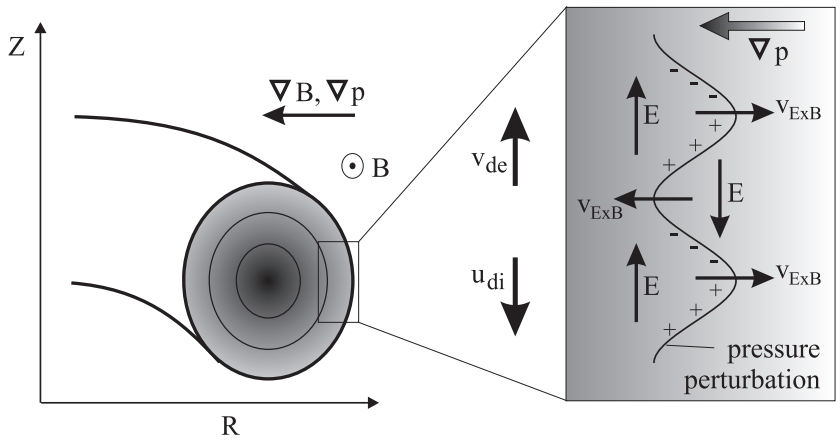

Figure 1.6.: *Geometry of the curvature driven ballooning instability. The diamagnetic drift is in opposite direction for electrons and ions. A pressure perturbation leads to a build-up of charge separation and hence electric fields* $\mathbf{E}$*. In regions of unfavorable curvature, the* $\mathbf{E} \times \mathbf{B}$*-drifts due to the charge separation enhance the initial perturbation.*

or not[3] (see discussion in Ref. [Scott 1990]). However, even if all modes in the model system are linearly stable, nonlinear destabilization is possible [Hirshman and Molvig 1979]. Nowadays, it is widely approved that a linearly stable system can be nonlinearly unstable and emerge into a turbulent, nonlinearly saturated state [Scott 1990, 1992].

1.3.3. Interchange instability and resistive ballooning modes

The interchange instability occurs in regions of the magnetic configuration in which magnetic field gradient and curvature point in the same direction as plasma pressure gradient (so-called 'unfavorable curvature'). The geometry for curvature driven instabilities is shown in Fig. 1.6, following Rosenbluth and Longmire [1957]. The diamagnetic drifts of ions $\mathbf{u}_{di}$ and electrons $\mathbf{v}_{de}$ trigger the instability: Assuming a pressure perturbation as shown in Fig. 1.6, these drifts lead to charge separation and the resulting electric field causes $\mathbf{E} \times \mathbf{B}$-drifts, which amplify the initial perturbation. The phase between potential and density is $\pi/2$, hence the associated plasma transport is maximal (cf. Sec. 1.2.3). The transport takes place as convective cells, i.e. by vortices elongated along the magnetic field. If the gradients of pressure and magnetic field point in opposite directions ('favorable' curvature), an initial perturbation is damped. In toroidal geometry, these modes are therefore damped on the high-field side (predominantly favorable cur-

[3] In fact, in toroidal geometry with a sheared magnetic field, drift waves are linearly unstable due to curvature [Chen and Cheng 1980].

vature) and grow on the low-field side. They are often called ballooning modes. Resistivity and high plasma-β[4] can destabilize these ballooning modes. The ballooning instability is discussed in more detail in Refs. [Nishikawa and Wakatani 1999; Zeiler 1999; Scott 2001].

The distinction between drift waves and curvature driven modes should be clarified here, following the discussion in Ref. [Scott 1997b, Sec. 4.1]. The source of free energy is the pressure gradient for ballooning modes as well as for drift waves. Curvature can act as a catalyst on drift waves and alter the phase shift between density and potential in a non-adiabatic way. However, the mechanism of resistive ballooning modes is different: The destabilization of the ballooning modes is driven by the relaxation of the pressure gradient in a plasma region with unfavorable magnetic curvature, whereas drift waves are destabilized by the parallel electron dynamics.

1.3.4. Nonlinear drift wave turbulence simulation: State of the art

Nowadays, modern simulation codes for the plasma edge take either the two fluid Braginskii equations or kinetic (Vlasov) equations as a starting point [Biskamp et al. 2000]. Since these equations are too complex to solve – especially in complex magnetic geometries – a set of reduced equations is used in numeric simulation codes [Zeiler et al. 1997; Jenko 1998; Jenko and Scott 1999; Scott 2001]

Collective phenomena described by these equations are often referred to as drift waves. Additionally to instabilities described in the previous subsections (i.e. the pressure gradient-driven drift wave instability and resistive ballooning modes that appear when curvature is included), the ion temperature gradient (ITG, η_i) modes can be derived from the model equations as well. Recent numeric simulations investigate nonlinear drift wave turbulence in a three-dimensional simulation domain [Biskamp and Zeiler 1995; Drake et al. 1995; Scott 1997b; Jenko and Scott 1998; Xu et al. 2000; Scott 2000]. Zeiler et al. conclude from their simulations, that turbulence in the core plasma is due to ITG modes, whereas in the plasma boundary the relevant process is the nonlinear drift wave instability. In the far edge the transport is dominated by resistive ballooning [Zeiler et al. 1998]. Since this work focuses on the turbulence in the plasma boundary, the reader is referred to the literature for more information on ITG modes [Horton 1999].

It was pointed out that nonlinear collisional drift wave turbulence in three dimensions has a significantly different behavior compared to similar studies in two dimensions [Biskamp and Zeiler 1995]. This finding stresses the interest in the three dimensional structure of the turbulence which is investigated in this

[4]The plasma β is the ratio of plasma pressure and magnetic pressure [Wesson 1997]

thesis. One result from the three-dimensional numeric drift wave codes should be highlighted here, since it has a considerable effect on the turbulence properties parallel to the magnetic field: Three-dimensional numerical drift wave turbulence simulations for the case of an unsheared magnetic field show that the radial transport is dominated by convective cells, i.e. toroidally elongated fluctuation structures which are aligned with the magnetic field (zero parallel wave number) [Biskamp and Zeiler 1995; Scott 1997a]. If magnetic shear is added in the models, the dominant structures in the evolving drift wave turbulence are reported to have a finite parallel wave number [Zeiler et al. 1996; Scott 1997a].

Compared to the complexity of the magnetic configuration in real tokamaks and stellarators, the implemented geometry in most simulation codes is fairly simple. To overcome this restriction, computations with realistic tokamak divertor geometries [Xu et al. 2000] and stellarator geometry [Kendl 2000] are in progress. First results from simulations by Xu et al. [2000] apparently stress the importance of geometric effects, since poloidal asymmetries in fluctuation properties were observed. Moreover, a new destabilization mechanism of resistive ballooning modes in X-point geometry was proposed [Myra et al. 2000].

Many more effects which influence the turbulence in the SOL are possible [Hidalgo 1995; Endler 1999]. There are for instance atomic processes (ionization, impurity radiation) and the sheath physics in front of the target plates [Stangeby 1986] that could decisively alter turbulence properties. The identification of significant contributions is a necessary step towards a better understanding of plasma edge turbulence. As for now, only few – if any – of these effects are included in the three-dimensional simulation codes.

1.3.5. From simulation to experiment

Although the main results from the different plasma turbulence codes are similar, it is necessary to identify the most important mechanisms of turbulence which are relevant for todays and future magnetic confinement devices. A close comparison between theoretical and experimental results would be a relevant contribution for achieving this objective.

One major intention of this work is to provide experimental results that can give insight into the turbulent mechanisms which are responsible for the anomalous transport. Much experimental work was already done over the past years, and data from fluctuation diagnostics provided new insights. For the plasma boundary region, electrostatic probes have proven to be a very useful tool because of the high spatial and temporal resolution.

A lot of the experimental research on anomalous transport was devoted to the characterization of the fluctuations in the most accessible region, the plasma boundary. The gained knowledge is already rather comprehensive for density and potential fluctuations in the radial and poloidal plane [Wootton et al. 1990; Endler

et al. 1995; Endler 1999]. Only few studies exist that cover the temperature fluctuations [Balbin et al. 1992; Giannone et al. 1994], which can be responsible for a significant fraction of the anomalous heat transport, confer Eq. (1.7). On Wendelstein 7-AS the work is in progress in order to improve the database on this important aspect by means of fast swept Langmuir probes [Pfeiffer et al. 1998; Schubert 2002]. Another important topic is the characterization of the turbulence in the plasma boundary parallel to the magnetic field. The progress in theory as well as plasma turbulence codes, namely the implementation of three-dimensional simulations, stressed the crucial role of the parallel dynamics within the three-dimensional turbulence in the plasma boundary. The present work focuses on the characterization of plasma turbulence parallel to the magnetic field, in order to contribute from the experimental side to the question, what physical mechanisms are relevant to plasma boundary turbulence.

At this point it is important to comment on the fluctuation measurements in various confinement devices, which differ greatly in size (major radii from 0.33 m at Keda Tokamak-5C [Kan et al. 1997] to 2.96 m at JET [Rebut et al. 1985]) and magnetic configuration (stellarators and tokamaks). Generally, the fluctations in the plasma boundary of the various magnetic confinement devices for fusion research are observed to have similar properties [Liewer 1985; Carreras 1992; Wagner and Stroth 1993]. The review by Stroth [1998] deals specifically with the differences and similarities of transport in stellarators and tokamaks. In particular, these two configurations differ from the toroidal plasma current, aspect ratio and magnetic shear. Nonetheless, the edge turbulence phenomena for tokamaks and stellarators are found to be similar and the conclusion was drawn that the differences between the two configurations are probably not fundamental components for the theoretical understanding of the observed anomalous transport [Stroth 1998].

1.4. Active control of plasma edge turbulence

Since the understanding of turbulence in the plasma boundary made significant progress over the past decades, different methods have been invented in order to modify the turbulence. Heat and particle removal to a material surface is partially governed by the perpendicular transport properties in the edge. There are two different aspects of the interest in modifying the plasma edge turbulence and therefore the anomalous transport. On one hand, decreasing the plasma edge turbulence probably leads to an improvement in edge energy confinement, and hence in core plasma heat insulation. On the other hand, the scrape-off layer should provide a sink for impurities and helium ash. Therefore, the outward particle transport for these species should be as high as possible. Since the parallel heat flux in the scrape-off layer towards the target plates is very large,

the deposition area on the targets should be as large as possible. This can be achieved by a large outward transport in the SOL.

The achievement of both goals, i.e., low outward energy transport just inside the last closed flux surface in conjunction with high particle transport of impurities and helium ash, will be very difficult if possible at all. Nonetheless, attempts are made in order to achieve any improvement in terms of impurity control and core plasma confinement.

Two qualitatively different methods of modifying plasma turbulence in magnetic confinement devices by means of electric fields are known:

1. Edge biasing: The principle is to bias electrodes that are inserted into the plasma edge or target plates with a voltage (relative to the vessel or another electrode, respectively target plate) in the order of some 10 to some 100 Volts. Reviews on the methods of edge biasing are given in Refs. [Boileau 1993; Weynants and van Oost 1993]. Edge biasing changes the profile of the radial electric field in the plasma boundary, as reported by Weynants et al. [1992], Lafrance et al. [1997] and Riccardi et al. [2000]. This can lead to a modification of the plasma edge turbulence due to shear flow decorrelation as discussed in Sec. 1.2.4 and by Terry [2000].

2. Feedback control: Basically, a control signal is used as input for a gain and phase-delay network. The output from this network is then used to drive the plasma actively and eventually leads to a modification of the plasma turbulence. It is shown in various non-confining plasma devices that dominant single and multi-mode instabilities can be modified – and also damped – by application of feedback schemes [Thomassen 1971; Sen 1994; Klinger et al. 2001]. Recent experiments combined spatial and temporal methods for actively driving and controlling drift wave turbulence in linear devices [Schröder et al. 2001]. However, in the plasma boundary of tokamaks and stellarators the plasma turbulence is fully developed, in the sense that the observed fluctuation spectra have no mode structure. Thus, a feedback sceme adopted to single unstable modes seems not very promising. Nonetheless, partiallly successful experiments on the TEXT tokamak are reported [Richards et al. 1994; Uckan et al. 1995], which utilize two electric probes for modifying turbulence in a spatio-temporal feedback scheme.

In the present work, special attention is devoted to the fact, that active probing experiments (either single signals, waves or feedback) can be viewed as a new diagnostic tool that can explore plasma boundary turbulence from a different point of view.

1.5. Overview over the work

As already pointed out above, this thesis is intended to contribute to the identification of basic physical mechanisms underlying the plasma turbulence and the plasma transport in the plasma boundary of tokamaks and stellarators. The work is organized as follows: In chapter 3, the experimental methods and the necessary data analysis tools are presented. Chapter 4 describes the findings from experiments conducted on the JET tokamak, where parallel correlation studies were carried out, which illuminate the parallel turbulence properties. In chapter 5, experiments in Wendelstein 7-AS and their results are presented. Those experiments utilize an active probe set-up and the extensive equipment of Langmuir probe arrays for fluctuation measurement purposes.

2. Methods and data analysis

In this chapter the methods of measurement and influencing of plasma parameters by means of plasma contactors (Section 2.1) as well as statistical methods and their application for the analysis of fluctuation data (Sections 2.2 and 2.3) are described. For a review on plasma turbulence diagnostics (and to some extent also data analysis) the reader is referred to the review by Bretz [1997].

2.1. Plasma contactors and electrostatic probes

The importance of the plasma boundary in tokamaks and stellarators was already mentioned in Sec. 1.2. A wide field of literature exists on plasma sheaths which form near a plasma contactor. Subsequently, the physics of plasma contactors is discussed within the framework of common simplifications used for plasma boundary phenomena in tokamaks and stellarators [Stangeby 2000, 1986]. For diagnostic purposes, an important application of plasma sheath theory is the interpretation of data obtained from electrostatic probes, the Langmuir probes. The ease of use of Langmuir probes is opposed to the difficulty to gain correct values of the plasma parameters from such measurements, especially in tokamak or stellarator environments: The plasma is fully ionized, the electrons and ions are assumed to have similar temperatures and strong magnetic fields apply. The simple probe theory discussed in this section turns out to be appropriate for the interpretation of fluctuation measurements of plasma properties and active probing with non-stationary signals. The thesis by Weinlich [1995] deals in more detail with the problems arising in probe theory in strong magnetic fields.

2.1.1. Plasma contactors and basic sheath physics

An electrically insulated plasma contactor (a conducting solid material) in a plasma is considered, see Fig. 2.1. Due to higher mobility compared to ions, an excess of electrons reaches the surface of the contactor and leads to a negative charge of the solid. Thereby, the influx of electrons is reduced and at the same time the ions in the plasma are attracted by the negative contactor. The rarefaction of the electron density at constant ion density shields the negative charge of the solid material and a potential sheath is formed. This sheath has a thickness in the order of the Debye length $\lambda_D = \sqrt{(\epsilon_0 k_B T_e)/(n_0 e^2)}$ [Chen 1984, Sec. 1.4].

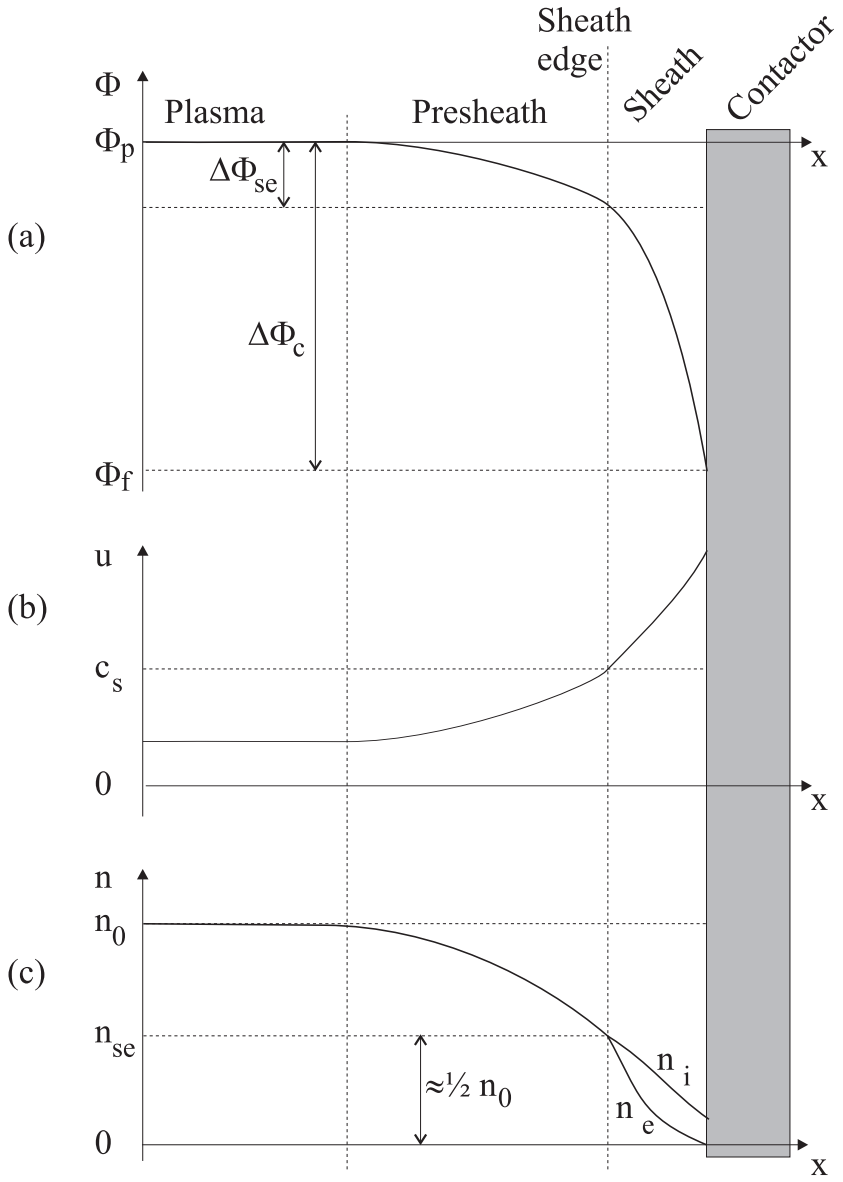

Figure 2.1.: *Schematic of the variation of (a) electric potential Φ, (b) ion flow velocity u and (c) plasma density n near a plasma contactor. (a) The contactor charges up to the floating potential Φ_f, which is negative with respect to the plasma potential Φ_p. (b) The ions are accelerated in the electric field of the presheath towards ion sound velocity c_s at the sheath edge. (c) The sheath is not quasi-neutral but the ion density n_i exceeds the electron density n_e. The density at the sheath edge n_{se} has approximately half the value of the upstream density far from the contactor n_0.*

It is kinetically sustained by an equivalent flux of ions and electrons towards the plasma contactor. An electric potential in the order of $\Delta\Phi_{se} \approx -0.7 k_B T_e/e$ exists at the junction between sheath and plasma, cf. Fig. 2.1(a). The associated electric field reaches into the plasma and the ions are accelerated towards the sheath edge. This region is called pre-sheath. Following Bohm's criterion, the ions must have a velocity u_{se} at the sheath edge of at least the ion sound velocity

$$c_s = \sqrt{k_B(T_e + T_i)/m_i}, \tag{2.1}$$

cf. Fig. 2.1(b) and Chap. 2 of Ref. [Stangeby 2000]. Due to the equilibrium between electron and ion fluxes, the contactor establishes a stable potential, the floating potential Φ_f. The difference between floating and plasma potential is given by the potential drop Φ_c over the sheath [Stangeby 1986]:

$$\Phi_c = \frac{1}{2}\frac{k_B T_e}{e} \ln\left[\left(2\pi\frac{m_e}{m_i}\right)\left(1+\frac{T_i}{T_e}\right)(1-\gamma_e)^{-2}\right] \tag{2.2}$$

T_e and T_i are plasma temperatures far from the sheath and γ_e is the secondary electron emission coefficient.

2.1.2. Estimation of plasma parameters with a Langmuir probe

Langmuir probes (small plasma contactors with an external circuit [Chen 1965; Matthews 1994]) are in common use to estimate the plasma potential, density and temperature in the plasma boundary.

As outlined above, a floating Langmuir probe measures the potential Φ_f, which differs from the plasma potential by the potential drop over the sheath,

$$\Phi_f = \Phi_p + \Phi_c. \tag{2.3}$$

Assuming a deuterium plasma with $T_e = T_i$ and a plasma contactor with no secondary electron emission $\gamma_e = 0$, the potential difference between probe and plasma can be calculated from Eq. (2.2) to be $\Phi_c = -2.8\, k_B T_e/e$. For measurements of plasma potential fluctuations $\tilde{\Phi}_p$, temperature fluctuations are often neglected in Eq. (2.3) and we obtain $\tilde{\Phi}_f = \tilde{\Phi}_p$.

If a voltage (bias) is externally applied to the plasma contactor, the fluxes of electrons and ions towards the plasma contactors balance. For sufficiently strong negative bias, the electrons cannot reach the contactor surface. The remaining ion current towards the plasma contactor is called ion saturation current $I_{i,sat}$. For singly charged ions (deuterium plasma) the ion saturation current density $j_{i,sat}$ towards the plasma contactor is given by [Stangeby 1986]

$$j_{i,sat} = 0.5\, e n_0 c_s \tag{2.4}$$

Here, the Bohm-criterion accounts for the ion sound velocity c_s and the factor 0.5 is due to the reduced density at the sheath edge compared to the upstream value outside the presheath, cf. Fig. 2.1 and Ref. [Stangeby 2000]. For the common assumption, that fluctuations in temperature (which affect the ion sound velocity c_s) are small, fluctuations in the ion saturation current are equal to fluctuations in the plasma density $\tilde{I}_{i,sat} \propto \tilde{n}_0$.

When increasing the bias towards positive voltages, more and more electrons with sufficiently high kinetic energy to cross the potential barrier account for electron current. Under normal conditions, the electrons have a Maxwellian velocity distribution and the electron current density rises exponentially with the potential Φ of the probe [Stangeby 1986],

$$j_e(\Phi) = j_{e,sat} \exp\left(\frac{e(\Phi - \Phi_p)}{k_B T_e}\right), \qquad \text{for } \Phi < \Phi_p. \tag{2.5}$$

Using Eq. (2.5) the electron temperature can be estimated from a measurement of the current-voltage characteristic. In reasonable approximation, the ion current only adds a constant offset (the ion saturation current) to the characteristic. For a bias voltage $\Phi > \Phi_p$, the sheath vanishes and the electron current is determined by the electron saturation current density

$$j_{e,sat} = \frac{1}{4} e n_0 \overline{c}_e (1 - \gamma_e), \tag{2.6}$$

with the average electron speed

$$\overline{c}_e = \left(\frac{8 k_B T_e}{\pi m_e}\right)^{1/2} \tag{2.7}$$

(electrons are assumed to have a Maxwellian velocity distribution, cf. Ref. Stangeby [2000]). In magnetized plasmas the value for the electron saturation regime is frequently not reached [Matthews 1994] due to effects described in the next subsection.

2.1.3. Natural collection length of a plasma contactor

In the present case with strong magnetic fields (ion gyro radius in the order or less than the dimensions of the plasma contactor $\rho_i \leq d$) in tokamaks and stellarators, the sheath theory is complicated due to the constrained movement of charged particles perpendicular to the magnetic field lines. Since the motion parallel to the magnetic field is fast, a flux tube[1] would be cleared from plasma in a very short time, if no perpendicular flux into the flux tube takes place. Only (anomalous) viscosity can account for drawing a cross-field current $j_\perp = e n v_\perp$

[1] A flux tube consists of the magnetic field lines which have contact to a plasma contactor

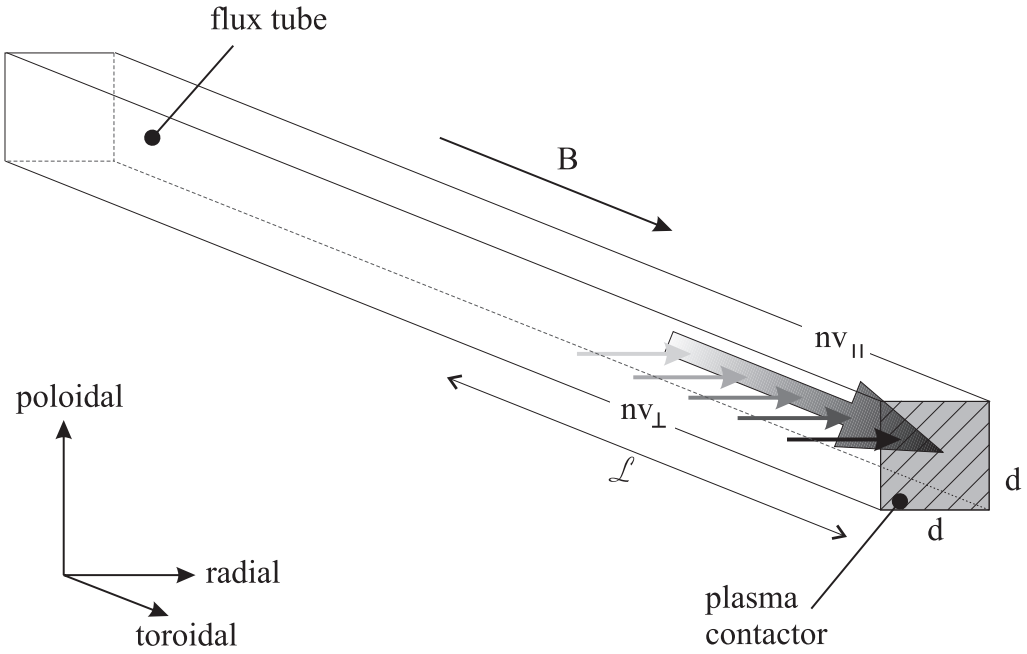

Figure 2.2.: *A plasma contactor (grey) with dimension $d \times d$ is located in a magnetized plasma with a strong magnetic field* $\mathbf{B}$ *perpendicular to the surface of the contactor. The perpendicular influx $nv_\perp$ is balanced by the losses parallel to the magnetic field $nv_\parallel$. The parallel scale of the disturbance by the plasma contactor is given by the natural collection length $\mathcal{L}$. Note that the disturbance is less strong far away from the plasma contactor. This is indicated by the brighter colors for the arrows denoting the direction of $nv_\perp$.*

[Matthews 1994] for a non-rotating plasma column[2]. In a steady state situation, the perpendicular current balances the parallel current. However, the perpendicular motion of charged particles in the magnetic field is hindered and therefore the perpendicular current density is limited. The influx from the unperturbed plasma will take place along a certain length of the flux tube parallel to the magnetic field, as shown in Fig. 2.2. In the literature this scale length is referred to as the natural collection length [Stangeby 1986]. Generally this scale is different for electrons and ions. It is possible to estimate the natural collection length $\mathcal{L}$ in a simple model from particle balance,

$$v_{\parallel}\, d^2 = v_{\perp} \mathcal{L}\, 4d\,. \tag{2.8}$$

Ions that enter the sheath must obey the Bohm-criterion $v_{\parallel} = c_s$. The (anomalous) perpendicular particle diffusion coefficient $D_{\perp}$ determines the perpendicular velocity $v_{\perp} = D_{\perp}/r = 2D_{\perp}/d$ [Stangeby 1986]. Since the anomalous transport is directed radially outwards, the influx on the right-hand side of Eq. (2.8) has to be replaced by $v_{\perp}\mathcal{L}\, d$. We finally obtain

$$\mathcal{L}_i \approx \frac{c_s}{2}\frac{d^2}{D_{\perp}}\,. \tag{2.9}$$

Considering Langmuir probes in ion saturation collection, the probe tip diameter is $d = 2$ mm and for the typical SOL values $D_{\perp} = 1\,\mathrm{m^2/s}$ and $c_s \approx 5 \cdot 10^4\,\mathrm{ms^{-1}}$ ($T_i = T_e = 20\,\mathrm{eV}$) one obtains $\mathcal{L}_i \approx 0.1\,\mathrm{m}$. The same holds reasonably well for the case of floating potential measurements, but for bias voltages larger than the plasma potential, the natural collection length is determined by the faster electron velocity according to Eq. (2.7), i.e. $v_{\parallel} = \overline{c}_e \approx 3 \cdot 10^6\,\mathrm{ms^{-1}}$ for $T_e = 20\,\mathrm{eV}$. This leads to an electron collection length of $\mathcal{L}_e \approx 6\,\mathrm{m}$. Due to such a large collection length, the parallel electron flow is likely to be collisional. This could explain the frequently observed reduction of the electron saturation current in magnetized plasmas [Stangeby 1986].

2.1.4. Consequences from the natural collection length on fluctuation studies in parallel direction

Stangeby [1986, p. 80ff] notes that the dimension of the probe head itself should be inserted in Eq. (2.9) as dimension d, since the whole object acts as a plasma contactor. This would lead to extremely long collection lengths for the ion currents as well as for the electron currents. The dimensions of the probe head are typically 10 times the dimensions of the probe tips, and therefore the collection lengths would be 100 times longer. Since the measured quantities ($\tilde{\Phi}_f$ and

[2] In principle, poloidal plasma rotation could account for perpendicular influx of plasma into the flux tube.

$\tilde{I}_{sat}$) are inherently averaged over the collection length parallel to the magnetic field, the interpretation of fluctuation measurements parallel to the magnetic field could be strongly affected. However, it is possible to optimize the probe design for fluctuation studies focusing on dynamics parallel to the magnetic field. Two different types of Langmuir probes are used:

1. Target probes are integrated into the divertor targets. Since the sheath is determined by the large plasma facing materials (like the divertor target plates), small Langmuir probes do not affect the sheath.

2. Poloidal probe arrays are introduced in the scrape-off layer from the outside. The probe tips are on the radially innermost position. Typical probe head dimensions are in the order of a few cm and hence the head acts as a limiter. However, since the perpendicular velocity in the particle balance [Eq. (2.8)] is due to the anomalous transport which is directed radially outwards, the plasma at the probe tips is not disturbed by the probe head. The relevant natural collection length for the tips of a poloidal probe array is indeed given by the tip dimensions only.

In conclusion, Langmuir probes in strong magnetic fields yield a good spatial resolution for ion saturation and floating potential measurements in parallel direction. The electron saturation current has very elongated collection volumes parallel to the magnetic field and should not be used for fluctuation studies in parallel direction. Conversely, for active probing, and hence the creation of non-local perturbations of the plasma, the electron-saturation branch is most important.

2.2. Statistical data analysis

In general, the observations made on a turbulent system yield multiple time series of fluctuating quantities. These time series can be analyzed by means of statistical data analysis. This standard approach is appropriate, since the statistical properties of a turbulent signal are usually reproducible, whereas the detailed properties do not seem to be predictable [Frisch 1995]. In a probabilistic description of turbulence, the time series are generated by a stochastic process. A single time series is just one realization of an infinite set of time series, which are possible for the generating process. The infinite set of time series that might have been observed is the so-called ensemble. In this work ergodicity is assumed for the process, which means that the ensemble average over different realizations is equivalent to a time average over a single time series [Chatfield 1996]. In the following, the basic data analysis methods used in this thesis are described. Introductionary texts on data analysis of time series are e.g. the books by Chatfield [1996] and Pécseli [2000]. For information on the discrete implementation of the functions introduced in this section, cf. Ref. [Press et al. 1992].

2.2.1. Fourier space analysis: Spectrum and Coherency

It is often useful to look at the spectra of time series in order to identify periodic signals in the data. The Fourier transform and its inverse are given by the equations

$$X(f) = \int x(t) \cdot \exp(-i\,2\pi\,ft)\,dt \tag{2.10}$$

and

$$x(t) = \int X(f) \cdot \exp(i\,2\pi\,ft)\,df. \tag{2.11}$$

The auto-power spectrum of a time series $x(t)$ is given by the product of the Fourier transform $X(f)$ with its complex-conjugate $X^*(f)$,

$$P_{xx}(f) = \langle X^*(f) \cdot X(f) \rangle. \tag{2.12}$$

The auto-power spectrum P_{xx} is also known as power density spectrum. The brackets $\langle \ldots \rangle$ denote an ensemble average over a number of realizations. For a single realization, the standard deviation of $P_{xx}(f)$ is 100% at each frequency [Press et al. 1992, chapter 13.4]). In the present case of discrete (sampled) data and with the assumption of an ergodic process, the ensemble average is equivalent to a summation over M neighboring frequencies. Usually, this averaging is implemented by a 'binning' of the time series in blocks of M data points. The average value of each block is then used for the further analysis. Both methods, summation over neighboring frequencies and time series 'binning', reduce the standard deviation of the discrete spectrum to $(100/\sqrt{M})\%$ [Press et al. 1992, chapter 13.4]. Spectra from time series with a sampling rate ΔT have a limit frequency, the so-called Nyquist frequency $f_{Ny} = 2/\Delta T$ [Chatfield 1996].

When considering two time series $x(t)$ and $y(t)$, the cross-power spectrum P_{xy} is defined analogously to the auto-power spectrum

$$P_{xy}(f) = \langle X^*(f) \cdot Y(f) \rangle. \tag{2.13}$$

Since P_{xy} is a complex function, it is common to write amplitude $|P_{xy}|$ and phase Φ_{xy} with

$$P_{xy}(f) = |P_{xy}(f)| \cdot \exp(i\Phi_{xy}(f)) \tag{2.14}$$

separately. The cross-coherency spectrum can be derived from the cross-power spectrum. It is defined as

$$\gamma_{xy}(f) = \frac{|P_{xy}(f)|}{\sqrt{P_{xx}(f)P_{yy}(f)}}. \tag{2.15}$$

The amplitude of the coherency is restricted to the range $0 \leq \gamma_{xy}(f) \leq 1$ and it measures the linear correlation between the spectral components of the two time series $x(t)$ and $y(t)$.

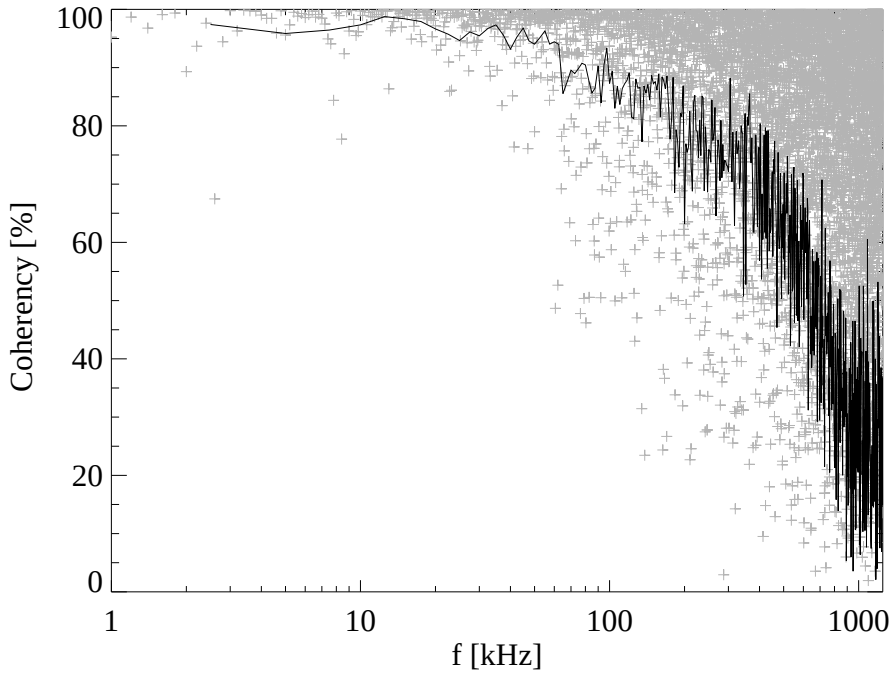

Figure 2.3.: *Semi-logarithmic plot of the cross-coherency spectrum calculated from two floating potential signals of two poloidally separated probe tips versus the frequency. The ensemble average is $M = 2$ (+) and $M = 25$ (straight line). The strong asymmetry of the coherency for $M = 2$ towards higher coherency especially for frequencies greater 100 kHz can be explained with the fact that the Fourier components of the neighboring frequencies have random phases. Hence, the ensemble average does not only decrease the amplitude of stochastic noise but also the mean value [Endler 1994]. Data from W7-AS discharge #50232*

Note here, that the average over neighboring frequencies is necessary for obtaining an estimate of the coherency with a sufficient statistical significance. Let us consider the case of a sampling frequency $f_s = 2.5\,\mathrm{MHz}$ and a time series of 100 ms corresponding to a data block of 25000 points. When averaging over two neighboring frequencies, $M = 2$, the coherency analysis would yield 6250 frequencies with a frequency resolution of $\Delta f = 200\,\mathrm{Hz}$ (Fig. 2.3). The frequency range would start at 0 Hz and end at the Nyquist frequency $f_{Ny} = 0.5 \cdot f_s = 1.25\,\mathrm{MHz}$. However, the standard deviation for each frequency is $(100/\sqrt{M})\% \approx 70\%$. For an averaging over $M = 25$ neighboring frequencies, the standard deviation is reduced to 20%, but the frequency resolution is now $\Delta f = 2500\,\mathrm{Hz}$. In this thesis an averaging over $M = 25$ neighboring frequencies is usually chosen.

2.2.2. Real space analysis: Correlation function

One of the most important tools for the description of fluctuating parameters is the cross-correlation function

$$K(\tilde{x}, \tilde{y}, \tau) = \langle \tilde{x}(t) \cdot \tilde{y}(t+\tau) \rangle \,, \tag{2.16}$$

where $\tilde{x}(t)$ and $\tilde{y}(t)$ are zero-mean fluctuation time series. This function provides information about the amplitude correlation between the two input time series for a time lag τ. A normalization to the auto-correlation functions $K(\tilde{x}, \tilde{x}, \tau)$ and $K(\tilde{y}, \tilde{y}, \tau)$ for $\tau = 0$ leads to the normalized cross-correlation function

$$C(\tau) = \frac{K(\tilde{x}, \tilde{y}, \tau)}{\sqrt{K(\tilde{x}, \tilde{x}, 0) \cdot K(\tilde{y}, \tilde{y}, 0)}} \in [-1, 1] \,. \tag{2.17}$$

Eq. (2.17) is referred to as cross-correlation function in this thesis.

For the correct normalization of the cross-correlation function, zero-mean data is required and an appropriate pre-processing prior to correlation analysis is necessary. A moving average is subtracted from the original data. The length of the averaging window is 1 ms. This filter also reduces the influence of perturbations and coherent oscillations below 1 kHz.

2.2.3. Two-dimensional correlation function

Multi-pin poloidal probe arrays have already been used for fluctuation diagnostics. Important features of fluctuations – like life time, poloidal scale length and poloidal group velocity – can be derived from raw data. In Fig. 2.4 a typical two-dimensional correlation function $C(\theta, \tau)$ is shown. The correlation function of the signals from the different probe tips with respect to one reference probe is grey scale coded, the vertical axis is the poloidal direction θ and the horizontal axis denotes the time lag τ. The reference probe is arbitrarily chosen, but for symmetry reason a central probe is preferred. A remarkable (and generally observed) feature of the diagram is the inclination of the contours. This inclination is associated with a non-zero group velocity of fluctuations in poloidal direction. A quantitative evaluation is possible by applying a least-square fit to the two-dimensional cross-correlation data. Following Bleuel [1998] an appropriate fit-function for W7-AS data is

$$C(\theta, \tau) = \frac{A}{\cosh(\tau/\tau_L)} \cdot \exp\left[-\left(\frac{\theta - v_g \cdot \tau}{l_\theta} \right)^2 \right] + \text{Offset}, \tag{2.18}$$

with fit parameters v_g (poloidal group velocity), τ_L (life time of the fluctuations) and l_θ (poloidal scale length, respectively correlation length).

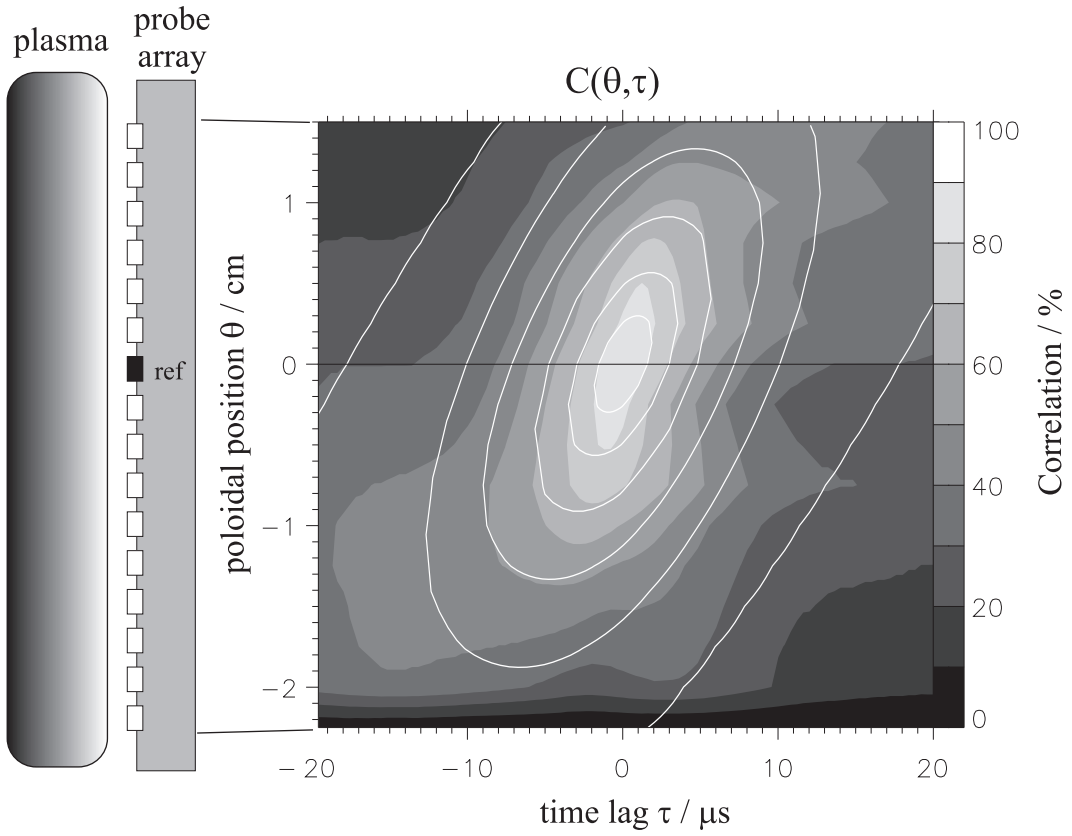

Figure 2.4.: *Contour plot of a two-dimensional cross-correlation function. The amplitude of the cross-correlation is grey scale coded. Simultaneously sampled signals (channels) from a set of poloidal probe tips (left) are used to calculate the cross-correlation function with respect to one (arbitrary) reference channel (indicated by the horizontal black line). A fit of Eq. (2.18) to the data is plotted in white lines. The results of this fit is a poloidal group velocity* $v_g \approx 880\,ms^{-1}$ *and a poloidal scale length* $l_\theta \approx 1.2\,cm$ *and a life time* $\tau_L \approx 7\,\mu s$*. (Data from W7-AS discharge #50232.)*

The assessment of fluctuation life time and scale length by correlation analysis are not absolute, but only relative measures.[3] Note, that the life time of fluctuation events estimated from the width of the auto-correlation function is usually too small compared to the life time estimated by the above method. This is due to the non-zero group velocity of the fluctuations [Endler 1994, p. 48ff].

2.2.4. Local wave number and wave number average

Consider two time series obtained from a synchronous measurement of two probes separated by a distance Δx. Following the definition by Smith and Powers [1973], the local wave number $k(f)$ for a frequency f can be calculated from the phase-shift $\Delta\Phi_{12}(f)$ between the two signals as

$$k(f) = \frac{\Delta\Phi_{12}(f)}{\Delta x}\,. \tag{2.19}$$

If several probe tips are available (e.g. a poloidal probe array), a better way to determine the local wave number is to fit the phases of the signals from several probe tips. This method is described in more detail in Sec. 2.2.5.

Since the local wave number is a function of frequency, it can be helpful to define an average (local) wave number. It is useful to statistically weight the spectral contribution $k(f)$ of the wave number with the corresponding component of the cross-power spectrum $P_{12}(f)$ [Beall et al. 1982],

$$\overline{k} = \frac{\int k(f)\cdot|P_{12}|(f)\,df}{\int|P_{12}|(f)\,df}\,. \tag{2.20}$$

For sufficiently small probe tip separation (i.e. high coherency between the two time series), the local wave number average is a good approximation for the conventional mean wave number obtained from spatial Fourier transform [Carlson 1991].

2.2.5. The lock-in technique

In this subsection, a different approach to fluctuation data is described. It is particularly useful for analyzing actively driven probe signals, but can also give valuable insight into any other fluctuation data with high spatial and temporal resolution. The analysis is based on a single frequency reference in the coherency and phase spectra, and is therefore comparable with the conceptual idea of a lock-in amplifier [Horowitz and Hill 1990].

[3] It was pointed out in Ref. [Grulke et al. 2001], that the life time estimated by correlation analysis is systematically too large.

Consider a poloidal probe array with a constant probe tip distance $\Delta d = 2.5\,\mathrm{mm}$, which is in use on the Wendelstein 7-AS (Fig. 2.5). The coherency and phase evolution between the signals from an arbitrarily chosen reference probe tip and all other probe tips are shown in Fig. 2.5 for a chosen frequency component $f_0 = 60\,\mathrm{kHz}$. Such a representation reveals important features of the fluctuation data: First of all, the poloidal scale length of the fluctuations can be estimated from the width of the coherency curve. The local slope of the phase evolution is equivalent to the local poloidal wave number $k_\theta(f_0)$. Since the phase is arbitrary for vanishing coherency, the slope of the phase is trustworthy only at poloidal positions with sufficiently high coherency. For the practical fit procedure, the amplitude of the coherency for the different poloidal positions is used as statistical weight. The fit to the data in Fig. 2.5 and also the local poloidal wave number $k_\theta(f_0)$, were obtained in that way.

It is possible to calculate the poloidal phase velocity from the wave number, $v_p(f_0) = 2\pi\, f_0/k_\theta(f_0)$. A rising or falling slope indicates the propagation direction[4]. A steeper slope of the phase corresponds to a lower phase velocity.

It is important to keep in mind that all features discussed above are valid only for the particular frequency f_0. A good example for dispersion effects is given by the observation, that the estimate of the group velocity of the same data (compare Fig. 2.4) gives a significantly lower value ($v_g \approx 880\,\mathrm{ms}^{-1}$) than the phase velocity at 60 kHz [$v_p(f_0) = 3700\,\mathrm{ms}^{-1}$].

2.3. Two point measurements

The characterization of spatial properties of the turbulence is of fundamental interest for the understanding of the anomalous transport in the plasma boundary, as already pointed out in Sec. 1.2.2. The radial and poloidal properties of plasma edge turbulence (spatio-temporal fluctuations in density, plasma potential and temperature) can be deduced to a high accuracy from measurements with poloidal and radial Langmuir probe arrays. The typical scale lengths in the direction perpendicular to the magnetic field (i.e. poloidal and radial) direction are of the order of mm to a few cm. Due to the anisotropy introduced by the magnetic field, the scale lengths in parallel direction (toroidal) are much larger, i.e. in the order of some meters.

Generally speaking, the distance between measurement volumes should be adapted to the expected scale lengths. In the case of Langmuir probes, the minimal useful toroidal distance is given by the natural collection length (see Sec. 2.1.3). The distance along a magnetic field line connecting the measuring

[4] In all analyzed W7-AS data, the propagation direction was in agreement with the direction of the $\mathbf{E} \times \mathbf{B}$-velocity. For different radial positions of the probe head, the $\mathbf{E} \times \mathbf{B}$-velocity shear region could be identified.

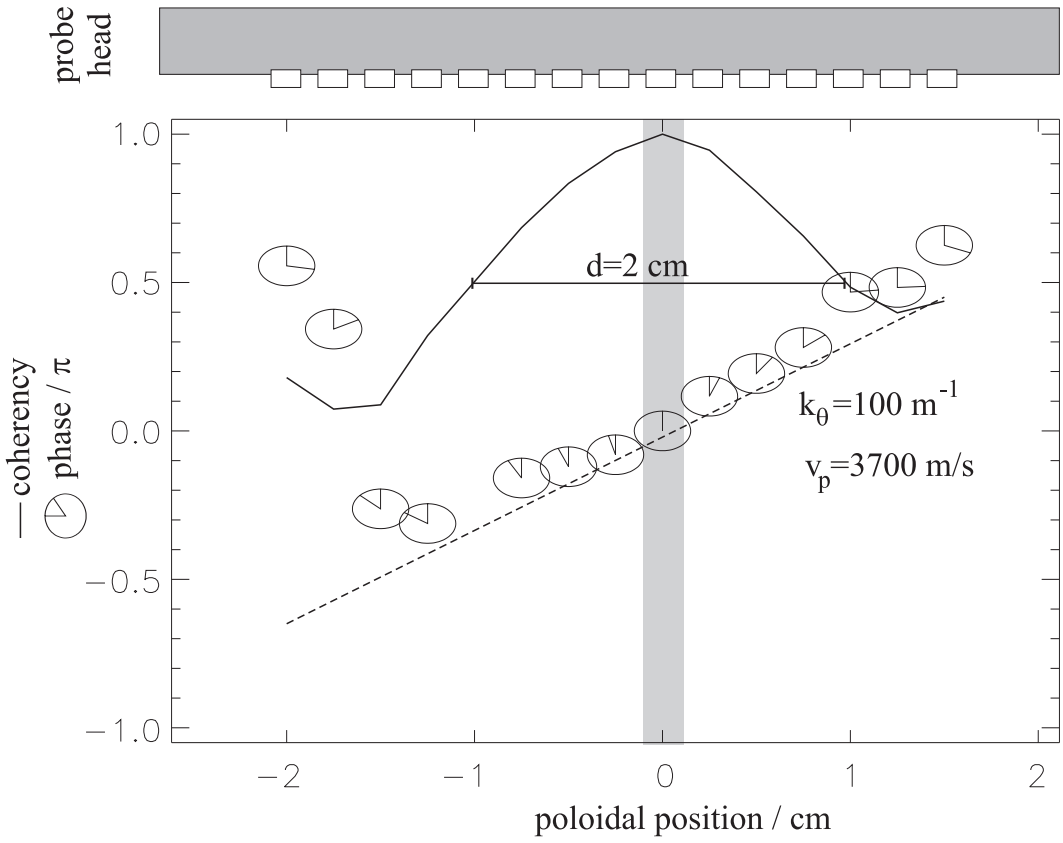

Figure 2.5.: *Top: sketch of a poloidal probe array with equidistant tip separation of 2.5 mm. Bottom: The coherency (solid line) and phases (clocks) are plotted versus the poloidal direction for frequency $f_0 = 60$ kHz. The reference probe for the analysis (poloidal position 0) is indicated by a grey box. From the coherency, a poloidal scale length $d = 2$ cm can be deduced (full width at half maximum). The gradient of the phase versus poloidal direction yields a phase velocity of $v_p = 3700\,ms{-}1$ (dashed line=fit). Data from W7-AS discharge #50232.*

positions is referred to as connection length.

2.3.1. Measurement along a magnetic field line

Fluctuating plasma parameters such as density, plasma potential and temperature are measured at two spatial points along a single magnetic field line. The data from these two channels are synchronously sampled by a fast analog-to-digital converter (typical sampling rate greater 250 kHz). Because of their high spatial and temporal signal resolution, mostly Langmuir probe arrays have been used. The probe tips measure the ion saturation current I_{sat} or floating potential Φ_f, depending on the external electric circuit.

The adjustment of the two probe arrays has to be chosen very carefully, based on magnetic field line calculations to assure the proper alignment along one field line. In order to have the highest possible correlation, two probes must be aligned within a small tolerable error, which is determined by the scale lengths of the turbulence. Experimentally, this is a difficult task, because a magnetic field line that starts on one fixed probe has to be found by another probe in the poloidal-radial plane at a certain toroidal distance. The radial direction can be 'scanned' by the movement of one reciprocating probe, and the poloidal displacement of the magnetic field line can be modified by small systematic changes in the magnetic field configuration.

2.3.2. Signals from one fixed and one moving probe

In the case that one input signal is collected by a probe at a fixed position and the other signal is from a reciprocating probe (e.g. performing a radial scan), it is useful to subdivide the data in sufficiently small blocks, such that each data block from the moving probe corresponds in a good approximation to a constant probe position z. The selected blocks should still be sufficiently long to provide good statistics in the frequency region of interest. The cross-correlation function $C(z, \tau)$ can be calculated for each data block. A typical outcome for $C(z, \tau)$ is shown in Fig. 2.6 as a contour plot. The horizontal axis is the time lag τ, the vertical axis represents the block number, respectively, the probe position z.

The interpretation of the results from such a measurement with one scanning probe and one fixed probe has to be done quite carefully. In particular, the same analysis as discussed in Sec. 2.2.3 for the interpretation of $C(p, \tau)$, e.g. the estimation of a group velocity from a fit function, is valid only with additional assumptions made:

- The plasma conditions must be stationary during the movement of the scanning probe.

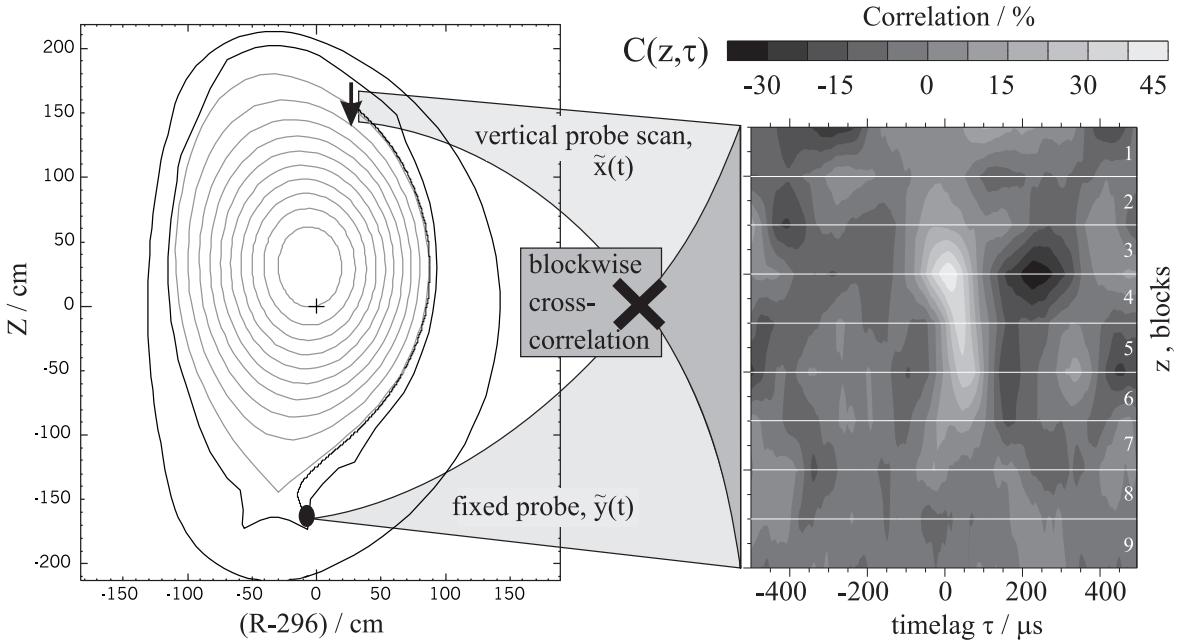

Figure 2.6.: *The cross-correlation function $C(z,\tau)$ of a signal $\tilde{x}(t)$ recorded from a moving probe and a signal $\tilde{y}(t)$ from a fixed probe. On the left hand side a poloidal plane on JET tokamak is sketched. The flux surfaces (grey) and the projection of the connecting field line (black) between one fixed probe (•, bottom) and a reciprocating probe (↓, top) are shown. On the right hand side a two-dimensional cross-correlation function is calculated (×) from $\tilde{x}(t)$ and $\tilde{y}(t)$ by subdividing the signals into 9 blocks (indicated by the white horizontal lines). The amplitude of the cross-correlation is grey-scale coded. Due to the movement of the top probe in z-direction, each block represents the cross-correlation function for another z. (Data from JET discharge #46796.)*

- The radial group velocity can be significantly modified by a poloidal shear velocity [Bleuel 1998, section II.2.3].

In this work, $C(z,\tau)$ is used for the identification of the maximal parallel correlation between a fixed and a reciprocating probe, only.

2.3.3. Two point scale length estimation

A rough estimate of the scale length is possible for data from two spatially separated measurement points: Let x be the distance between these two points and $C_{max}(x) = \max_{\tau}[C(x,\tau)]$ the maximum of the cross-correlation. Since the spatial resolution is poor, an assumption about the shape of the correlation along x has to be made in order to describe the scale length mathematically. One approximation can be a Gaussian (for a poloidal length scale estimate, this should be a good approach, at least for small poloidal background velocities, compare Eq. (2.18)):

$$C_{max}(x) \propto \exp\left(-\frac{x^2}{l_x^2}\right). \tag{2.21}$$

In this equation, l_x is a measure for the scale length (correlation length) for fluctuations along x.

2.3.4. Parallel wave number

The parallel wave number $k_{\|}$ is an important quantity for the study of the parallel dynamics of fluctuations. The parallel wave number relates the propagation direction of a wave front with the reference direction of the magnetic field lines. If the fluctuations do not propagate in direction parallel to the magnetic field only, then the parallel wave number has a non-zero value.

Up to now only two-point measurements were conducted for the study of $k_{\|}$ in tokamaks and stellarators. The difficulties in using an improved set-up with more than two probes aligned along a single field line arise from the large scale length of the fluctuations in parallel direction. Due to the small parallel wave number (large scale length), the distance between the sampling points has to be large. However, the alignment of the probes in the complicated geometry of tokamaks and stellarators is delicate already for two toroidally separated probes only.

Following the method by Ritz et al. [Ritz et al. 1988], the average parallel wave number $\overline{k}_{\|}$ can be estimated from the deviation $d_{\perp}$ between a line connecting two toroidally separated probes and the magnetic field line (see Fig. 2.7). For a vanishing time lag of the cross-correlation between the signals from the two probes, the probes are aligned along the wave front. For this situation, the

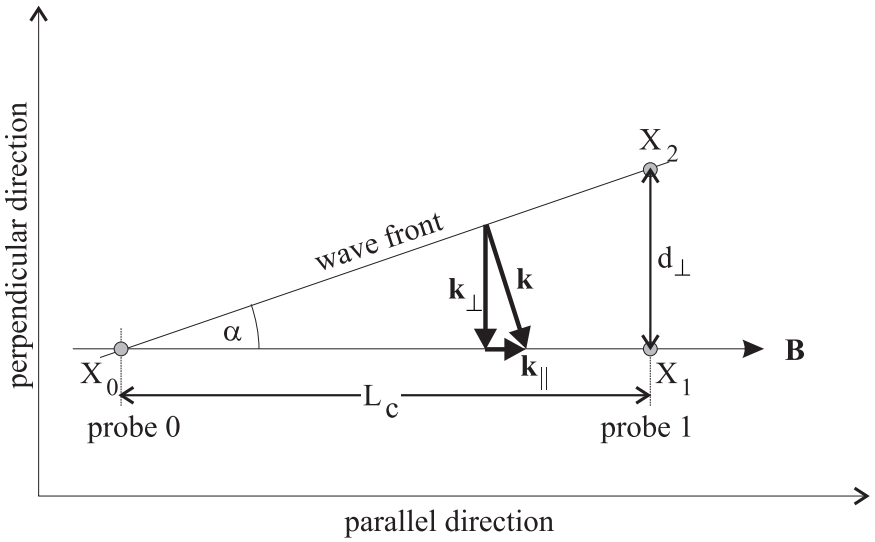

Figure 2.7.: *Geometry for the estimation of the parallel wave number $k_{||}$ from the connection length L_c, perpendicular wave number $k_\perp$ and distance $d_\perp$. The points X_0 and X_1 are located on the same magnetic field line, X_2 is on the same wave front passing X_0 and has a perpendicular distance $d_\perp$ from X_1. Experimentally, the wave front can be identified in parallel direction from the cross-correlation function between the signal from probe 0 at X_0 and a probe 1 at distance L_c scanning the perpendicular direction. When probe 1 is aligned (at X_2) along the wave front with X_0 , the maximum of the cross-correlation will be found at zero time lag $\tau = 0$.*

average parallel wave number is given by

$$\overline{k}_{||} = \frac{d_\perp \cdot \overline{k}_\perp}{L_c}, \tag{2.22}$$

with $k_\perp$ the average perpendicular wave number (2.20).

3. Three-dimensional structure of fluctuations in the plasma boundary

Experimentally, the plasma turbulence in the boundary of tokamaks and stellarators is found to be of quasi two-dimensional nature: The correlation lengths (and therefore the scale lengths of the turbulence) in the plane perpendicular to the magnetic field $\mathbf{B}$ are of the order of mm—cm, but parallel to the magnetic field, the measured correlation lengths are of the order of several meters.

Three-dimensional numerical drift wave turbulence simulations for the case of an unsheared magnetic field show that the radial transport is dominated by convective cells, i.e. toroidally elongated eddy-like fluctuation structures with a parallel wave number $k_{||} = 0$ [Biskamp and Zeiler 1995; Scott 1997a]. If magnetic shear is included in the model, the dominant structures in the evolving drift wave turbulence tend to have a finite parallel wave number [Zeiler et al. 1996; Scott 1997a].

Most of the parallel correlation measurements performed so far (see Sec. 3.1) are not suitable to check this prediction, because the realized connection lengths are presumably too short. One question to be addressed in this chapter is the distinction between

- two-dimensional dynamics with convective cells as dominant structures
- three-dimensional dynamics with toroidally structures of finite extend.

This chapter is organized as follows: In Section 3.1 an overview about the status of research for correlation measurements in parallel direction is given. The set-up for the measurements done in the JET tokamak is introduced in Section 3.2. The results from the experiments follow in Sections 3.3 and 3.4. In Section 3.5 the influence of perturbations on the parallel correlation measurements is investigated by means of a simple model approach. The results are discussed in Section 3.6.

3.1. Motivation for the parallel correlation measurements on JET tokamak

3.1.1. Status of research

Various experiments in different tokamaks and stellarators were devoted to parallel correlation measurements of fluctuating plasma parameters. High correlations in the direction parallel to the magnetic field are found for ion saturation currents and floating potential with connection lengths varying from 1—12 m.

On the TEXT tokamak, high coherencies up to 100% were reported for connection lengths of 1.2 m and a parallel wave number of $k_{\|} = 1.5 \pm 1\,\mathrm{m}^{-1}$ [Ritz et al. 1988]. In subsequent experiments on TEXT Upgrade, carried out by Winslow et al. [1997] and Bengtson et al. [1998], a coherency of about 60% was found for probe pairs separated 12 m. No significant coherency was found for a distance of 28 m, probably due to interference of limiters. The parallel wave number was reported to be $k_{\|} = 0.1 \pm 0.04\,\mathrm{m}^{-1}$.

Rudyj et al. [1989,1990] found maximum correlations of 80% and zero parallel wave number at a connection length of about 10 m in probe correlation measurements of ion saturation current fluctuations in the scrape-off layer on the ASDEX tokamak.

Correlation measurements on Wendelstein 7-AS stellarator were performed by Bleuel et al. [1996]. At a connection length of 6 m a maximal correlation of 92% was reported for ion saturation current and floating potential fluctuations [Bleuel et al. 1996]. The same high correlations were found 2 cm inside the last closed flux surface [Bleuel 1998]. Other experiments establishing a connection inside the LCFS along a distance of 32 m show a reduced correlation of about 40% for ion saturation current and floating potential [Bleuel et al. 1997; Bleuel 1998]. In order to achieve a long connection length of 32 m in the relatively small Wendelstein 7-AS device, it was necessary to perform the measurements inside the last closed flux surface. The connecting field line circulated 2 1/2 toroidal turns passing from the outboard side via the inboard side back to the outboard side. The parallel wave number was reported to be $k_{\|} = 0.01\,\mathrm{m}^{-1}$ [Bleuel et al. 1997].

A clear explanation for the observed lower correlation parallel to the magnetic field at a very large connection length could not be given, since there are a couple of effects involved:

- The reduced correlation for very long connection lengths could be an inherent feature of plasma boundary turbulence.
- Since the turbulence is sometimes strongly affected by curvature could be affected by curvature, the passage of the connecting magnetic field line

via the inboard side with predominantly favorable magnetic curvature on Wendelstein 7-AS could affect the turbulence and thus the coherency.

- The turbulent dynamics inside the last closed magnetic flux surface is based on different boundary conditions. Several properties of the plasma turbulence in the confinement zone are actually found to be different from those in the SOL [Zoletnik et al. 1999]. Therefore, the fact that the connecting magnetic field line is embedded in the confinement zone could be a reason for the observations.

3.1.2. Heuristic models

Subsequently, four heuristic models of the parallel properties of fluctuations in the plasma boundary are presented. Furthermore, their direct impact on two-point measurements is discussed. A common assumption for all four models is a constant poloidal velocity v_θ of the fluctuations. This is justified by the experimental observation, that fluctuation structures propagate with the $\mathbf{E} \times \mathbf{B}$-velocity of background plasma Endler [1999].

Firstly, filaments (fluctuation structures elongated in toroidal direction) are considered. An inclination of these filaments with respect to the magnetic field (which always defines the parallel direction) and hence a parallel wave number $k_\parallel \neq 0$ can be expected. Filaments with a zero parallel wave number correspond to the theoretically motivated picture of convective cells, which are expected for resistive ballooning modes in regions of unfavorable curvature (Sec. 1.3.3). Convective cells are also found to play an important role in numerical simulations of drift wave turbulence simulations, cf. Sec. 1.3.4. Experimentally, the direction of the filaments is determined by the maximum correlation between two probes, which is not necessarily the direction of the magnetic field line. The $\mathbf{X}$-direction indicated in Fig. 3.1 is given by the alignment of the two probes used for the two-point measurement. The simplest case of a constant pitch of the filaments parallel to the $\mathbf{X}$-direction is shown in Fig. 3.1(a). A two point measurement yields a cross-correlation function similar to the signal's auto-correlation function. The maximum cross-correlation would be observed for zero time lag $\tau_s = 0$.

A slight extension of this heuristic model assumes an equi-distributed spectrum of parallel wave numbers $k_\parallel$ and hence a spectrum of inclinations of the filaments [Fig. 3.1(b)]. This would also result in a cross-correlation function with the maximum at zero time lag. Relative to the auto-correlation the width of the cross-correlation function is significantly broadened.

A different concept is shown in Fig. 3.1(c), where fluctuation events preferably occur at a certain region along the $\mathbf{X}$-direction. This region could be, for example, the zone of unfavorable magnetic curvature. A non-zero time lag of the cross-correlation maximum is the result and the width of the cross-correlation function

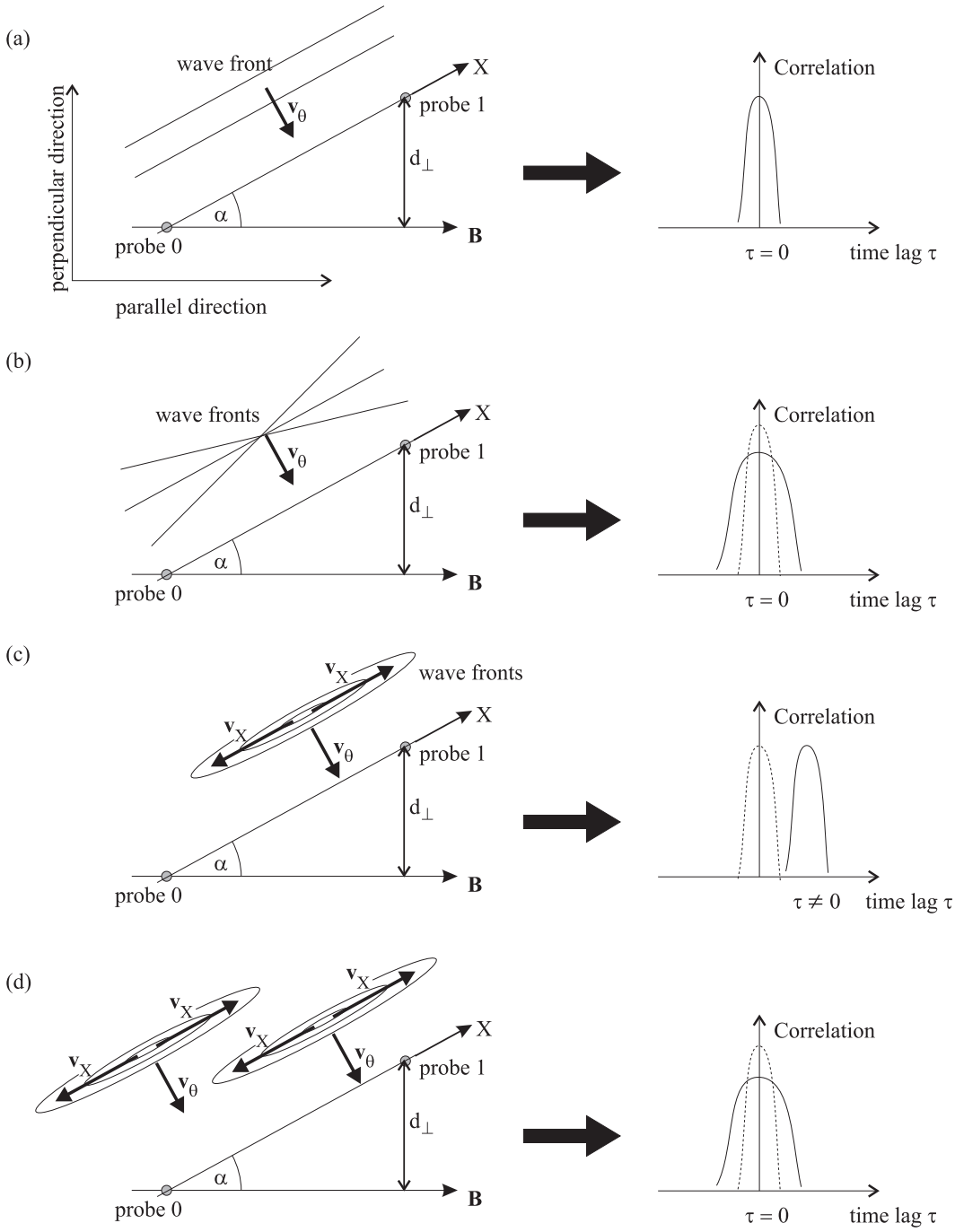

Figure 3.1.: *Heuristic models for the properties of fluctuations in parallel direction. The left column shows four different model assumptions and the right column the cross-correlation (solid line) and the auto-correlation (dashed line) functions, which would be obtained from two-point measurements for the respective models. The parallel coordinate (as defined by the magnetic field* $\mathbf{B}$*) is the horizontal axis, the vertical axis denotes the perpendicular direction. The two probes used for the two-point measurement are aligned in* $\mathbf{X}$*-direction.* v_θ *and* v_X *denote propagation velocities in poloidal direction and in* $\mathbf{X}$*-direction. See main text for details of the models.*

is again comparable with the width of the auto-correlation function.

A natural extension of this heuristic model would be to assume the presence of several fluctuation events distributed along the **X**-direction. They propagate with the velocities $\mathbf{v}_\theta$ in poloidal direction and $\mathbf{v}_X$ in parallel direction (with $\mathbf{v}_X \gg \mathbf{v}_\theta$). This is illustrated in Fig. 3.1(d). From the cross-correlation function, it is not possible to distinguish this case from the case of extended filaments with an equi-distributed spectrum of inclination angles [Fig. 3.1(b)].

3.1.3. Open questions

The main questions raised in the two previous subsections can be summarized the following way:

- What effect causes in W7-AS the observed reduction of the parallel correlation for a connection length of 32 m in comparison to the high correlations observed for connection length 6 m?
- Is the parallel wave number of the fluctuations non-zero, or are the fluctuations just aligned to the magnetic field?
- Which of the above described heuristic models for the fluctuations is closest to reality?

3.2. Set-up on JET tokamak

For the parallel correlation measurements on JET, two Langmuir probe systems were available (Fig. 3.2). One system consists of four probe tips on the outer and four on the inner vertical target plates of the Mark II Gas Box divertor [Matthews et al. 1996; Bertolini et al. 1997]. In the following, these probe tips are referred to as outer and inner divertor probes. The second system is a nine-pin reciprocating probe head installed at the top of the device [Davies et al. 1996]. Only three probe tips (operating in ion saturation collection) from the nine-pin head produced reliable signals. The data from the other six tips was not used for the analysis. Since the divertor probes were operated in ion saturation collection as well, only ion saturation data is used for the analysis. By usage of a field line tracing code, possible connections between these probe tips can be calculated in realistic field geometry (based on the magnetic equilibrium reconstruction by the EFIT code[1] [O'Brian et al. 1992]). The safety factor at 95% of the magnetic flux surfaces (q_{95}) is a good measure for the changes in the magnetic configuration

[1] EFIT= Equilibrium FITting is a computer code that translates measurements from magnetic diagnostics into plasma geometry and current profiles by solving the Grad-Shafranov equation.

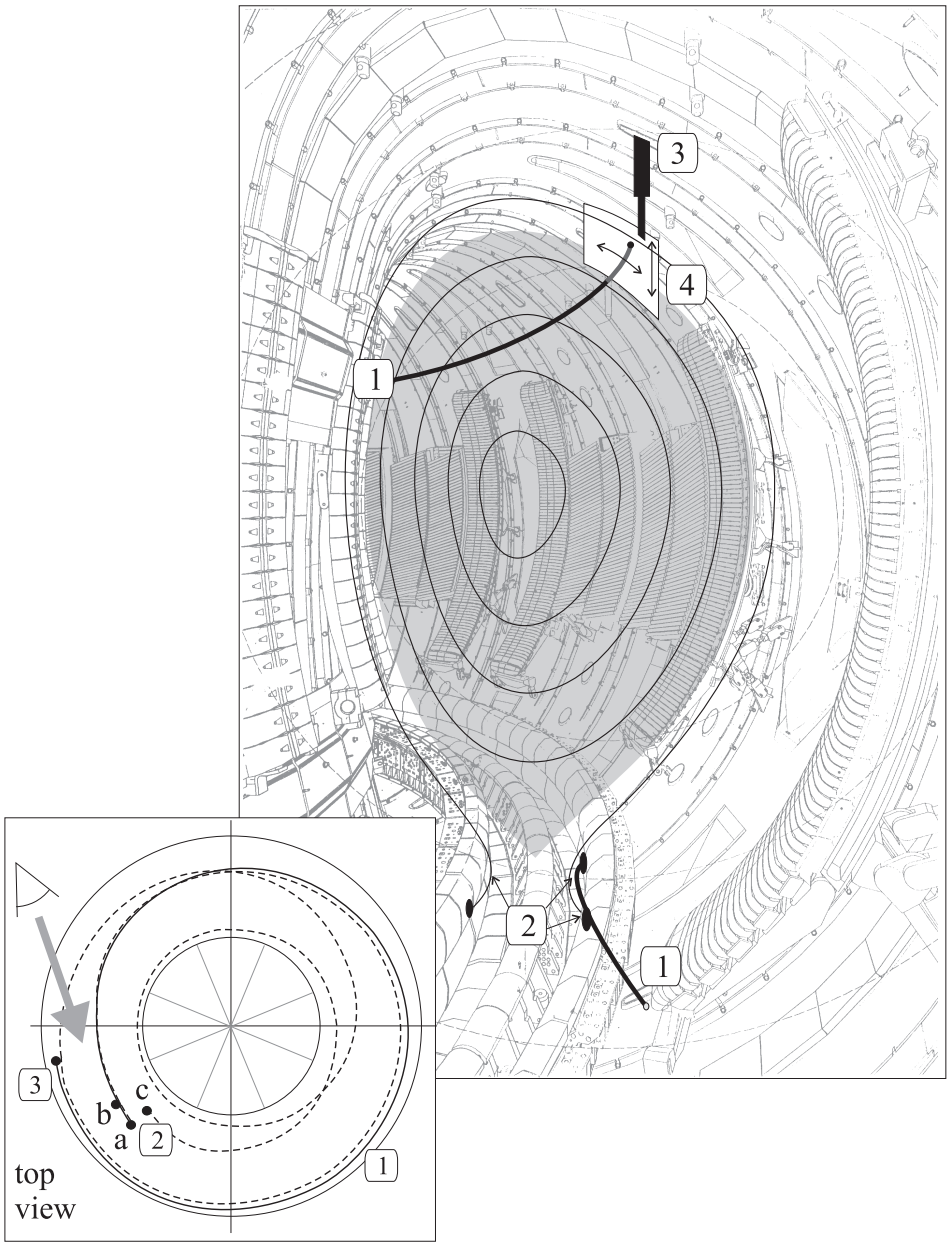

Figure 3.2.: *Sketch of a poloidal view into the JET tokamak with the magnetic flux surfaces. The confinement region is indicated as a grey shade. The outboard side (low B-field side) is on the right, the inboard side (high B-field side) on the left. (1) magnetic field line connecting the outer divertor target probes (2, right) with the reciprocating probe system (3). Poloidal displacement (4) of a magnetic field line (bold black) due to changes in the safety factor. By adjusting the magnetic configuration in conjunction with the radial scan during a reciprocation of the probe head, the connecting field line can be found in the white rhombical area. The inset figure shows the top view on JET tokamak. The 23 m connection (solid line between tip 2a and reciprocating probe 3) and the 66 m connection (dashed and solid line between tips 2a and 2b) are plotted. The 0.75 m connection is established between tips 2a and 2c.*

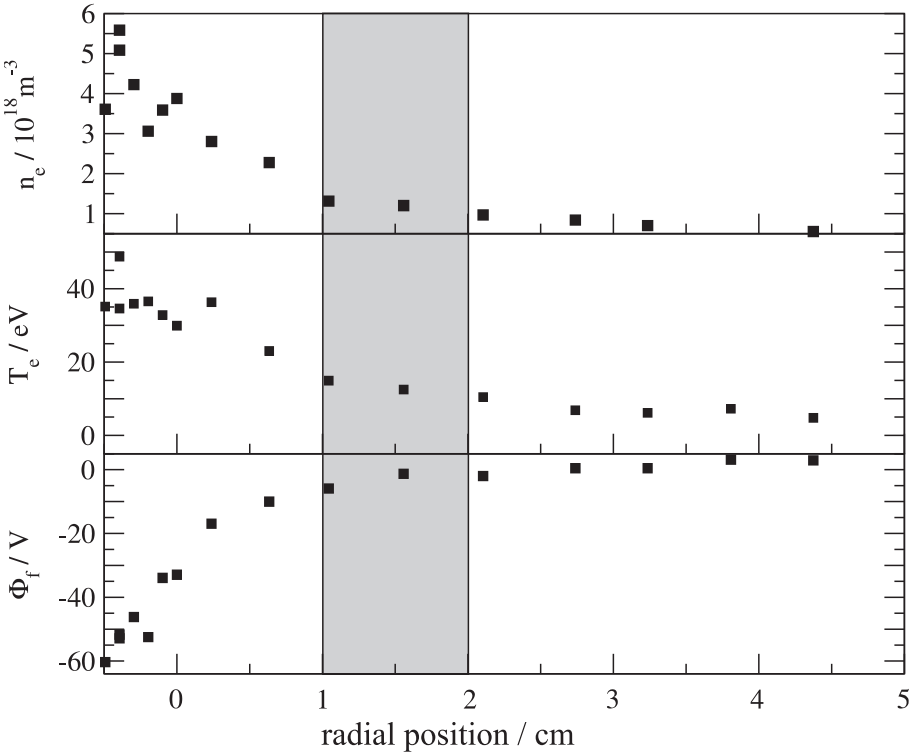

Figure 3.3.: *Density, electron temperature and floating potential versus the radial position of the reciprocating probe. The quantities are calculated from the Langmuir probe characteristics collected by a swept probe tip (sweep frequency 10 kHz) on the reciprocating probe head. The grey area denotes the position where the parallel correlation for the 23 m connection length was found. The radial scale is in midplane cm and 0 denotes the EFIT-calculated position of the separatrix.*

near the separatrix (see below). Three connection lengths are possible in the accessible safety-factor region (in-set Fig. 3.2):

- outer divertor probe - outer divertor probe : 0.75 m ($q_{95} = 2.7$)
- outer divertor probe - reciprocating system : 23 m ($q_{95} = 2.6$)
- inner divertor probe - outer divertor : 66 m ($q_{95} = 2.6$)

Experimentally, these connections can be achieved for slightly different plasma currents $I_{pla} = (2.4 \pm 0.1)$ MA at a constant toroidal magnetic field $B_{vac} = 2.0$ T. All measurements were performed in purely ohmic discharges and with the same magnetic configuration (except for the small variations in the plasma current).

For a basic characterization of the JET plasma boundary, a radial scan of density, electron temperature and floating potential is plotted in Fig. 3.3. The data is calculated from Langmuir probe characteristics of a swept tip on the

reciprocating probe head.

In Sec. 3.3, the experimental results of the 23 m connection between outer vertical target probe and reciprocating probe are described in some more detail. In Sec. 3.4 the results of the 75 cm and 66 m connections are presented.

3.3. Parallel correlation study on JET tokamak: The outboard connection (23 m)

From the results of the previous experiments on Wendelstein 7-AS by Bleuel [1998] (cf. Sec. 3.1) it was not clear whether the observed reduction of parallel correlation was caused by the long connection length itself, by the passage through the region of favorable curvature, or whether it is specific for long connection lengths in the confinement region.

Since the questions raised are – predominantly – caused by the limited size of the W7-AS, during this work experiments were conducted in the much larger JET tokamak. In JET, the world's largest tokamak, a long connection length of 23 m in the scrape-off layer can be achieved, which is completely embedded in the region of unfavorable magnetic curvature.

3.3.1. Results from field line tracing calculations

For different magnetic configurations, a field line starting at the outer divertor probe is traced along the torus outside up to the position of the reciprocating probe. The distance between these two probe positions along the field line is approximately 23 m. A typical result of the field line calculations is shown in figure 3.4. The field line tracing code (ORBITB) has as the fixed stop condition, that the radial coordinate of the field line is equal to the reciprocating probe position R_{probe} within a certain box in toroidal and vertical direction around the probe position. The actual poloidal displacement $d_\perp$ between the calculated field line and the top probe is estimated from the poloidal and toroidal component of the magnetic field at the probe position (B_{pol} and B_{tor}), the radial coordinate R_{probe} and the difference Δ_{tor} between the calculated end position (toroidal component) and the toroidal position of the reciprocating probe:

$$d_\perp = \Delta_{tor} \cdot \frac{B_{pol}}{B_{tor}} \cdot R_{probe}. \tag{3.1}$$

The magnetic configuration is calculated from magnetic measurements by means of the EFIT-code. The calculated poloidal displacement for several JET-discharges with different safety factors q_{95} is plotted in Fig. 3.5.

A variation of 0.01 in q_{95} leads to a poloidal displacement of the field line of 0.8 cm at the reciprocating probe (connection length 23 m). The discrepancy be-

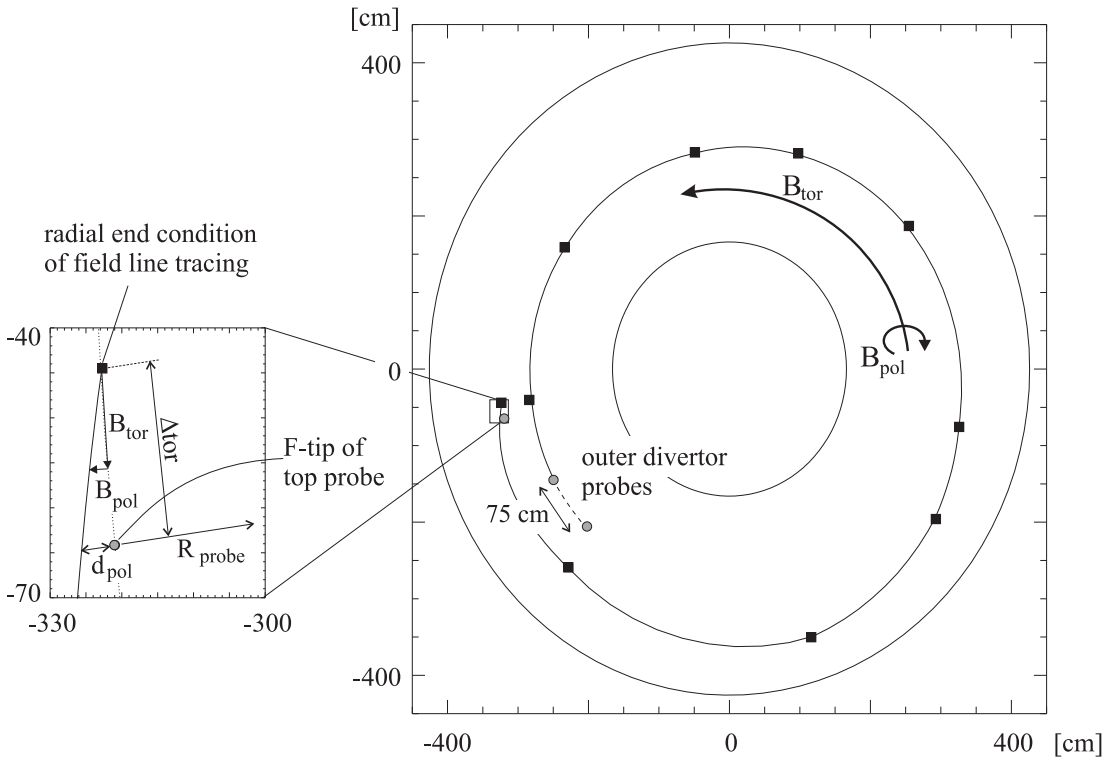

Figure 3.4.: *Result from field line tracing for the 23 m connection length for the (experimentally determined) magnetic configuration with the maximal parallel correlation value. The actual calculated positions from the ORBIT tracing program are the black squares, the connecting line is a sketch to help the eye. The 75 cm connection is plotted as dashed line. Data from ORBITB using EFIT data from JET discharge #47738, 60.89 s)*

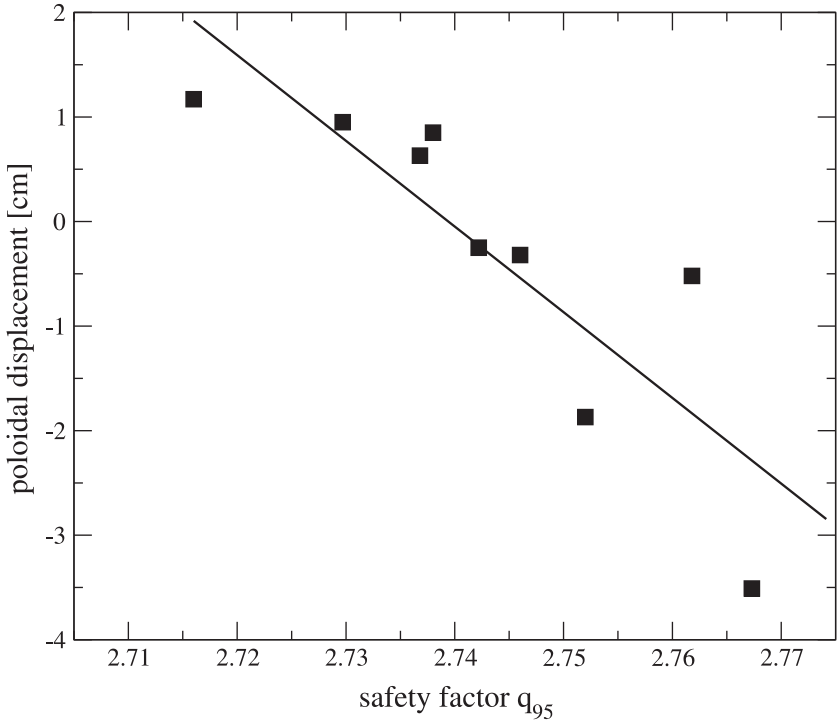

Figure 3.5.: *Poloidal displacement at the reciprocating probe system versus safety factor q_{95} for a field line starting at an outer divertor probe (23 m connection length). The squares are the results from EFIT calculation and field line tracing, the solid line is a linear fit. A variation of 0.01 in q_{95} leads to a poloidal shift of the field line of about 0.8 cm at the reciprocating probe.*

tween the points representing the EFIT-calculations for different discharges and the fitted line is probably caused by numerical uncertainties due a variation of other parameters of the magnetic configuration, namely the vertical plasma position. The vertical instability – which is specific for a tokamak with an elongated shape – is most likely to be responsible for such a deviation. It's influence on the parallel correlation measurements will be discussed separately in Sec. 3.5. The poloidal displacement $d_\perp$ is especially important for the estimation of the parallel wave number. This analysis is presented in Sec. 3.3.5.

3.3.2. Connection on the outboard side

For the comparison with the results from Bleuel [1998] and to find the answers to the questions raised in Sec. 3.1, the outboard 23 m connection between one fixed outer divertor probe and the reciprocating probe is most revealing. This connection length is completely embedded in the region of unfavorable curvature

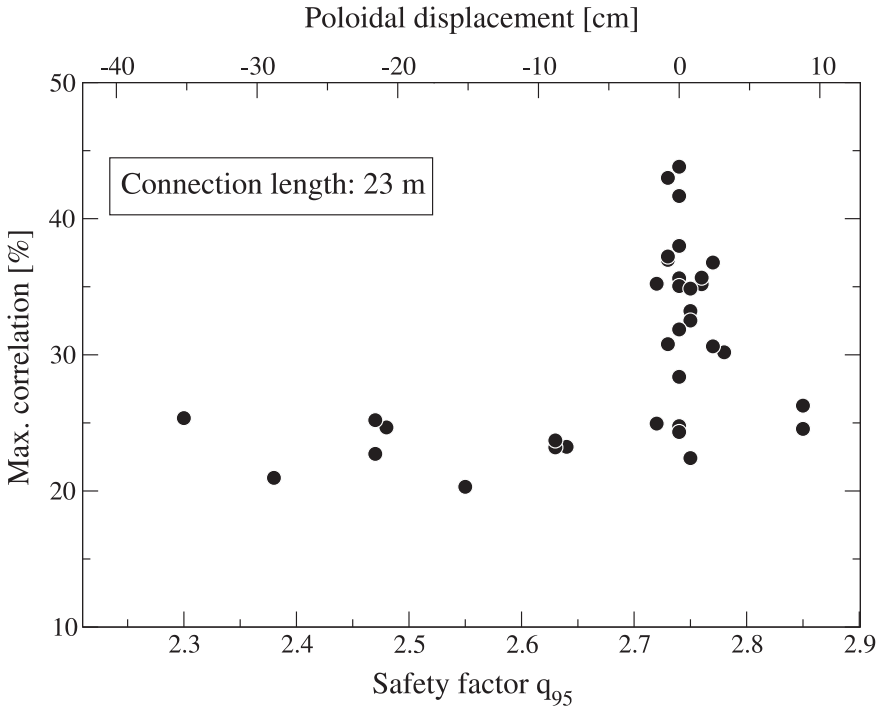

Figure 3.6.: *Maximum correlation of radial scans versus the safety factor q_{95} for a desired connection length of 23 m. The actual magnetic connection is clearly established for $q_{95} \approx 2.73$. The relatively high background correlation of about 20% is due to accidental correlations between the unrelated fluctuation events within the comparatively short time windows used for the correlation analysis.*

in the scrape-off layer.

A large scan of the safety factor from $q_{95} = 2.2$ to $q_{95} = 2.9$ was performed as well as a finer scan around $q_{95} = 2.75$ in order to find the maximum correlation between the two probes. In order to find the best alignment between the outer divertor probe tip and the reciprocating probe, several nearly identical pulses with only minute changes in the plasma current were performed. The plasma shape remained unchanged in the various discharges and therefore the safety factor q_{95} is to a good approximation proportional to the poloidal displacement.

In each pulse, the reciprocating probe was used to collect radially resolved fluctuation data, while the connecting field line was shifted poloidally from one pulse to the next one. The actual poloidal shift was estimated afterwards from the safety factor q_{95} calculated by the EFIT equilibrium code. These measurements result in spatially highly resolved scans in poloidal and radial directions at a connection length of 23 m. 200 ms data were recorded during the movement of the reciprocating probe. This time interval was sub-divided into windows of 10 ms. The movement of the probe is approximately 8 mm during that time. The time

windows (or data blocks) represent different radial positions, but the variation of the background plasma parameters during one such data block is relatively small. The cross-correlation functions between data from tips of the divertor and the reciprocating probe systems were calculated for each corresponding time window.

In Fig. 3.6 the result of such a poloidal scan is shown. Each point in the graph is representing the maximum correlation during a reciprocation between one tip of the movable probe and one tip in the outer divertor. It is clearly seen that a connection between the two distant probes is established at a safety factor of $q_{95} \approx 2.73$. The maximal cross-correlation is approximately 42%. The respective radially resolved two-dimensional cross-correlation function has already been shown in Fig. 2.6.

3.3.3. Background level correlations

The rather high background level of the cross-correlation function (cf. Fig. 3.6) can be understood, presuming burst-like fluctuation events ('blobs') in the fluctuations Theimer [1997]; Endler [1999]; Beyer et al. [2000]. Even if two of these events are not related to each others but occur within an arbitrary time delay of t_{12}, the cross-correlation function would show a high correlation at time lag $\tau = t_{12}$. A high background correlation level could therefore be due to the occurrence of several fluctuation events during one time window of the correlation analysis. In Figures 3.7(a-c) the cross-correlation functions of signals from the top and the outer divertor probe are plotted for three different discharges together with their auto-correlation functions. For safety factors not matching the connection between the top probe and the outer divertor probe [Figs. 3.7(a) and (c)], the maximal correlation is found at time lags $\tau_s \neq 0$ with $|\tau_s| \gg 0$ [Fig. 3.7(e)]. For the matching safety factor $q_{95} \approx 2.74$ the maximum correlation is observed for $\tau_s \approx 0$ [Fig. 3.7(b)].

The life time of fluctuations is of the order of the width of the auto-correlation function[2], some 10 μs. The life time of a fluctuation event determines the maximum time lag occurring in a cross-correlation function, which physically be related to the same event. Maxima in the cross-correlation function at time lags $\tau_s > 100\,\mu$s can therefore be regarded as spurious correlations.

An error of the correlation maxima shown in Fig. 3.6 can be estimated the following way. Since the length of the sub-windows used for the correlation analysis is indeed arbitrary within a certain range, a time sub-window of 10 ms is generally used here. The time sub-windows should be not too long, otherwise the radial movement of the reciprocating probe – and hence the change due to

[2]Since no measurement on the JET tokamak with a poloidal probe array with sufficient spatial resolution exits, a better estimate for the life time is not at hand. Generally, the estimate for the life time from the width of the auto-correlation function will be too small, compare Sec. 2.2.3 and reference [Endler 1994, p. 48ff].

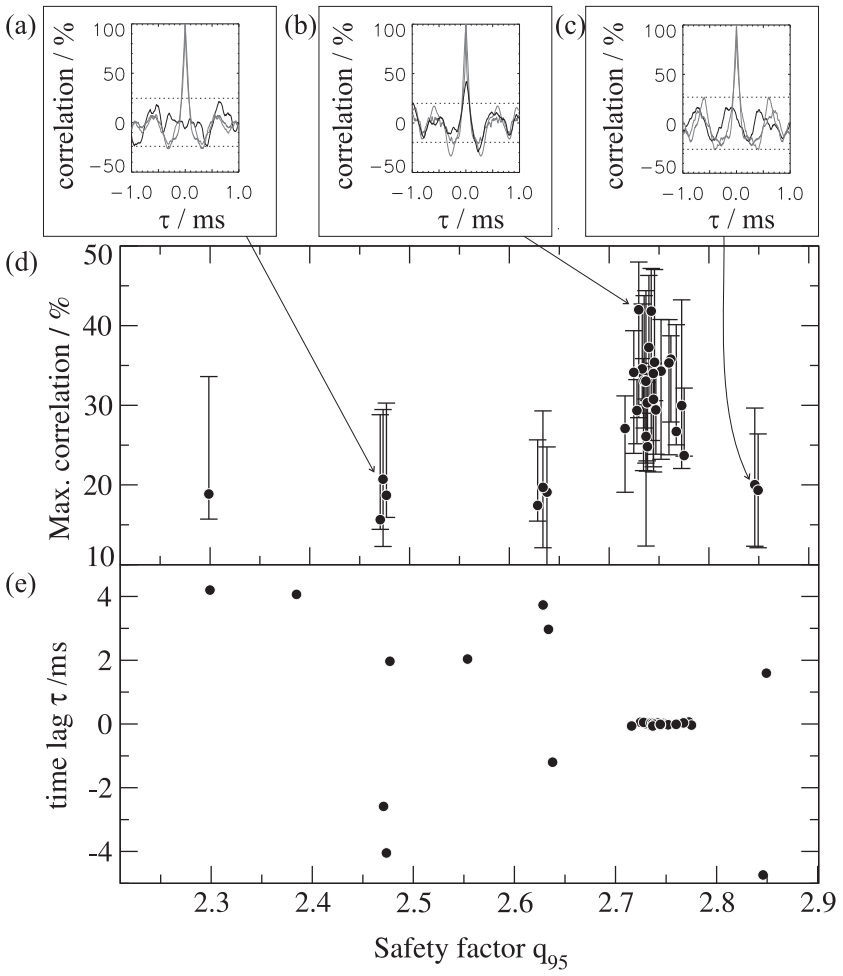

Figure 3.7.: *(a,b,c) Cross-correlation (black line) and auto-correlation functions (grey lines) for three different discharges. The relatively high background level correlation is caused by random correlation for large time lags $|\tau| \gg 0$. (d) Maximum correlation of radial scans versus the safety factor q_{95}. The bars indicate the range of maximum values obtained for a variation of the length of the time sub-windows used for the correlation analysis of 5 ms and 20 ms. (e) The time lags corresponding to the points of maximum correlations in (d).*

the radial gradient of the stationary plasma parameters – becomes important. They must not be not too short either, as otherwise the statistics is bad and slower components are not considered. An estimate for the errors of the maximal correlations can be estimated by using different time sub-windows of the same data for the correlation analysis. The bars in Fig. 3.7(d) are computed for two different time sub-window lengths of 5 and 20 ms.

3.3.4. Parallel propagation velocity

From the above presented measurements it is possible to obtain limits for the parallel propagation velocity $v_{||}$ of the fluctuations.

Let us first consider, whether the configurations with maximum correlation between two probe tips aligned parallel to the magnetic field are also those with the correlation maximum at time lag $\tau = 0$. If the maximum correlation is achieved at $\tau_s \neq 0$, an average parallel velocity of $v_{||} = L_c/\tau_s$ can be ascribed to the fluctuations. L_c is the connection length between the two probe tips. In Fig. 3.8 the maximum correlation is plotted versus the corresponding time lag τ for the connection length $L_c = 23\,\mathrm{m}$. The scatter of the time lag is clearly seen, and hence the direct estimation of τ_s is not possible. A mean value of $\overline{\tau}_s = (14 \pm 50)\,\mu\mathrm{s}$ is obtained by fitting a Gaussian to the data. The result is compatible with the fluctuations occurring simultaneously at the two probe tip positions. With $|\tau_{s,max}| = 64\,\mu\mathrm{s}$ the lower limit of the parallel velocity is $|v_{||,min}| \approx 3.6 \cdot 10^5\,\mathrm{ms}^{-1}$. For comparison, the Alfvén speed in the edge plasma is approximately $v_a \approx 2.6 \cdot 10^7\,\mathrm{ms}^{-1}$ and the electron thermal velocity $v_{th,e} \approx 1.9 \cdot 10^6\,\mathrm{ms}^{-1}$ (cf. Fig. 3.3).

3.3.5. Parallel wave number

The parallel wave number can be determined by the method described in Sec. 2.3.4. For a configuration with maximal correlation between two probe tips, which are located on exactly the same magnetic field line, the parallel wave number is zero. The question, whether the probes are indeed perfectly aligned, can only be answered by using a magnetic field line tracing code to project the position of the first probe into the poloidal plane of the second probe for a given configuration (Sec. 3.3.1).

In general, the projected position of the first probe deviates from the position of the second probe tip by a distance $d_\perp$. In previous studies conducted in other devices, small parallel wave numbers and hence small values of $d_\perp$ with respect to the connection length were observed (Sec. 3.1).

For the 23 m connection length on JET tokamak, a displacement of $d_\perp = 2.1\,\mathrm{cm}$ is obtained by field line tracing. Due to uncertainties in the position of the reciprocating probe head, in the plasma position (e.g. caused by the vertical

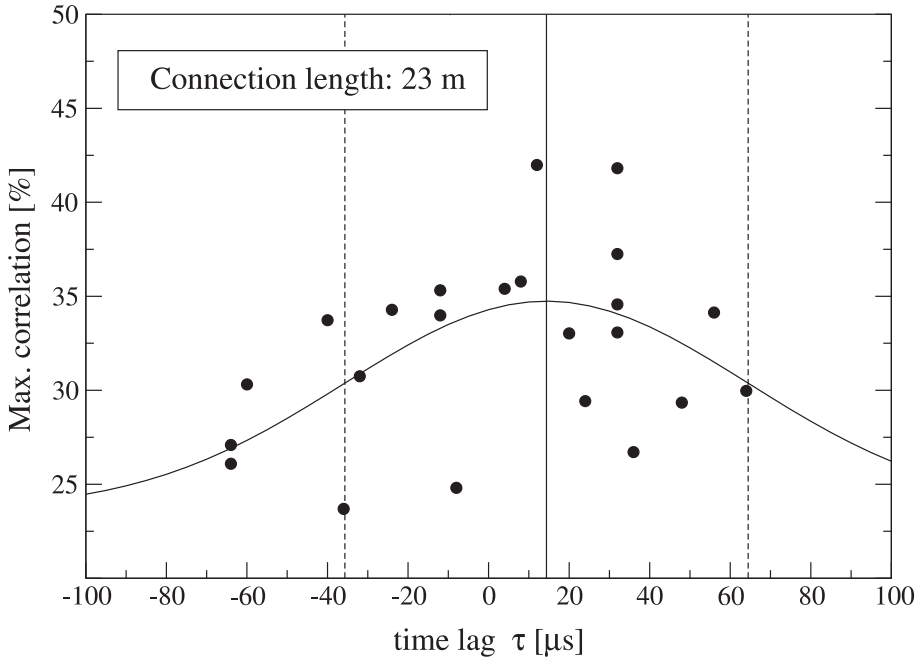

Figure 3.8.: *The maximal correlation of the radial scans is plotted versus the corresponding time lag τ for the connection length of 23 m. The solid curve is obtained by a fit to a Gaussian with offset, the vertical solid line denominates the mean $\overline{\tau} = 14\,\mu s$, the dashed lines the standard deviation. In the whole τ window of 10 ms, other high correlations in the range of 20—30% with time lags $|\tau| > 500\,\mu s$ are present (not shown). These are accidental correlations due to the short time window, compare Sec. 3.3.3.*

plasma instability) and in the calculation of the safety factor (see Figs. 3.5 and 3.6), $d_\perp$ is only known with an uncertainty $\Delta d_\perp = 2.8\,\mathrm{cm}$. The error analysis is made in more detail in App. A.2.

Within the simplified geometry of Fig. 2.7, probe 0 at position X_0 is associated with the outer divertor probe in the JET experimental set-up and X_1 is given by field line tracing. Position X_2 is the position of the reciprocating probe tip, at which the magnetic connection with the outer divertor probe is established. The maximum correlation is obtained at $\tau_s = 0$ (within the error bars for τ_s). Hence, the probes are aligned along a wave front, and the average wave vector is perpendicular to this wave front. The application of Eq. (2.22) is justified to compute the average parallel wave number $\overline{k}_\parallel$.

The missing average perpendicular wave number $\overline{k}_\perp$, can be estimated by Equations (2.19) and (2.20) from signals of two probe tips separated in perpendicular direction. There exists one probe tip at the outer vertical target which is separated from the tip at position X_0 by a distance of 1.5 cm in poloidal and 0.87 cm in radial direction. The value for the average perpendicular wave number estimated in this way is $\overline{k}_\perp = (0.71 \pm 0.09)\,\mathrm{cm}^{-1}$. The error is specified by the standard deviation of average perpendicular wave number estimates. Data is obtained from discharges with a safety factor $q_{95} = 2.73 \pm 0.03$.

Inserting these figures into Eq. (2.22), we find for the average parallel wave number $\overline{k}_\parallel = (0.065 \pm 0.095)\,\mathrm{m}^{-1}$ and, taking the errors into account, we can specify an upper boundary for the average parallel wavenumber $|\overline{k}_\parallel| < 0.16\,\mathrm{m}^{-1}$. Within the error bars, a vanishing parallel wave number is possible. The upper limit for the ratio between the average wave numbers parallel and perpendicular to the magnetic field is $|\overline{k}_\parallel/\overline{k}_\perp| < 0.0022$, which is a significantly lower limit than that of $|\overline{k}_\parallel/\overline{k}_\perp| < 0.01$ reported from other experiments [Endler 1999].

3.4. Parallel correlation study on JET tokamak: The short (0.75 m) and long (66 m) connection

3.4.1. Connection between divertor probes

For the other two connection lengths of 0.75 m and 66 m no radial scans were possible. The parallel connections are established between three different fixed probes, two located in adjacent modules of the outer divertor, and the third in the inner divertor.

For a connection length of 75 cm between two outer divertor probes in adjacent modules, a correlation of up to 82% was obtained (Fig. 3.9). Scanning the safety factor q_{95}, the correlation shows a broad maximum, since the poloidal dis-

placement of a field line is only small even for a large variation of q_{95}. However, the correlation might even be higher, because the field lines connecting these two probes may still be radially displaced. For the 66 m connection length between one inner and one outer divertor probe, the maximum observed cross-correlation is 41% (Fig. 3.9) at a safety factor $q_{95} \approx 2.63$. Since no finer scan was performed for this safety factor region, the maximum observed correlation of 41% should be seen as a lower limit only.

3.4.2. Comparison between different connection lengths on JET tokamak

Taking into account only the time window with the maximal correlation (and therefore the best alignment of the two probes), a comparison of cross-correlation, coherency and phase for the three different connection lengths (0.75 m, 23 m and 66 m) is possible.

In Fig. 3.10(a) the cross-correlation function versus the time lag τ and the coherency and the phase versus the frequency are plotted for the 0.75 m connection length. The coherency is high for frequencies up to 10 kHz and the phase is around zero over the complete frequency range, indicating that all frequency components are nearly in phase between each two probes. The same analysis for the optimal time window of the 23 m connection length is plotted in Fig. 3.10(b). The coherency is about 60 % at 1 kHz and is insignificant at frequencies of 10 kHz and above (as indicated by the stochastic phase in this frequency range). The maximum observed cross-correlation of 41% for the 66 m connection length (safety factor $q_{95} \approx 2.63$) is shown in Fig. 3.10(c). The monotonous change in phase up to ≈ 8 kHz indicates a slight misalignment, if one assumes that the highest correlation is obtained at zero phase shift (as was found in the measurements on other devices). Otherwise, the coherency and phase (as well as the correlation function) resemble the case of the 23 m connection length.

For comparison, the cross-correlation function, coherency and phase between two probe tips in the outer divertor are shown in Fig. 3.10(d). These two probes are separated 1.5 cm poloidally and 0.86 cm radially. The maximum of correlation is observed at non-zero time lag, in contrast to the previously discussed results from parallel correlation measurements. This is also observed in the cross-phase of Fig. 3.10(d).

3.4.3. The parallel wave number spectrum

An alternative approach to obtain information about the parallel wave number spectrum takes as a starting point the maximum amounts of cross-correlation parallel to the magnetic field for different connection lengths, as presented in

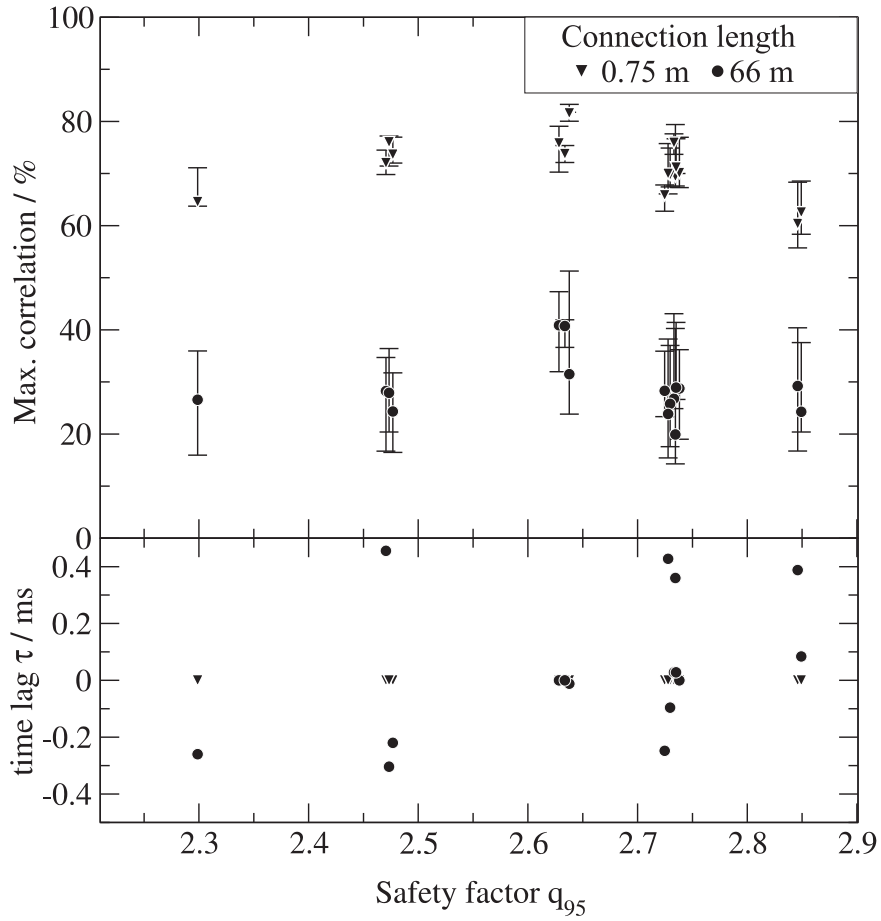

Figure 3.9.: *Top: Maximal observed cross-correlation versus safety factor q_{95} for the two connection lengths of 0.75 m (triangles) and 66 m (circles). Each point represents the correlation maximum in the τ-range $[-0.5\,ms, 0.5\,ms]$. The bars indicate the range of maximum values obtained for a variation of the length of the time sub-windows used for the correlation analysis between 5 ms and 20 ms. For the long connection the correlation is higher for $q_{95} \approx 2.63$. Bottom: The time lags τ_s corresponding to the correlation maxima plotted above. For the short connection length, $\tau_s = 0$ over the whole q_{95}-range. The long connection has $\tau_s = 0$ only for the observed maximum at $q_{95} \approx 2.63$.*

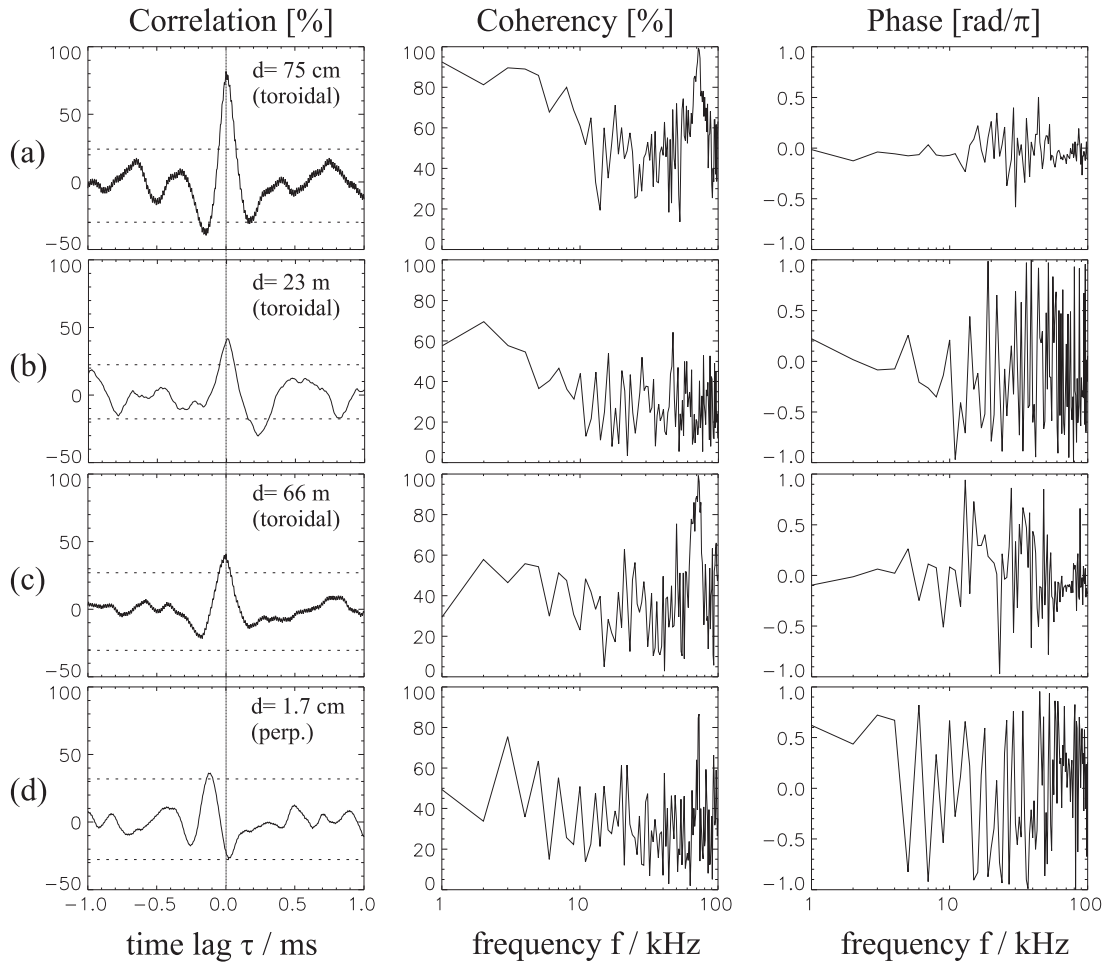

Figure 3.10.: *Comparison of the correlation functions, coherency and phase for the three established connection lengths of* 0.75 m *(a),* 23 m *(b) and* 66 m *(c) at JET and (d) for signals from two probe tips in the outer divertor (distance:* 1.5 cm *poloidal,* 0.87 cm *radial,* 0 cm *toroidal). The data used for the analysis in (b) is equivalent to data block 4 in Fig. 2.6. The dotted horizontal lines in the correlation diagrams in the left column indicate the maximal and minimal correlation on the whole* τ *window of* 10 ms *outside the displayed* τ*-range. For (a) and (c), an* 80 kHz *mode is prominent in the coherency. This is probably due to signal pick-up of the noise of a power supply and should have no effect on the correlations because of its low spectral power contribution. (JET discharges #46805, #46796, #46807, #46796)*

Fig. 3.10(a-c): On the one hand, when increasing the connection length from $L_c = 0.75$ m to $L_c = 23$ m, the correlation drops from $C_{max} > 82\%$ to $C_{max} \approx 42\%$. On the other hand it remains at $C_{max} \approx 41\%$ when moving on to $L_c = 66$ m.

This could be explained by assuming two fluctuation components with different parallel scale lengths $l_{\parallel,1}$ and $l_{\parallel,2}$. Let us assume – for simplicity and lack of more detailed information in toroidal direction – a Gaussian shape of the parallel correlation $C_{max}(x)$ with width $l_\parallel$,

$$C_{max}(x) = A \exp\left(-\frac{x^2}{l_\parallel^2}\right). \tag{3.2}$$

The Fourier transform ($\circ\!\!-\!\!\bullet$) of Eq. (3.2) is again a Gaussian that can be transformed in a similar mathematical form with the substitutions $\Delta k_\parallel \equiv 2/l_\parallel$ and $\tilde{A} \equiv A\, l_\parallel \sqrt{\pi}$:

$$A \exp\left(-\frac{x^2}{l_\parallel^2}\right) \circ\!\!-\!\!\bullet A\, l_\parallel \sqrt{\pi}\, \exp\left(-\frac{x^2\, l_\parallel^2}{4}\right) \equiv \tilde{A}\, \exp\left(-\frac{k^2}{(\Delta k_\parallel)^2}\right). \tag{3.3}$$

Hence, it is possible to calculate estimates for the scale lengths $\Delta k_\parallel$ of the parallel wave number spectra for the two assumed fluctuation components. However, nothing can be said about the actual mean wave numbers k_1 or k_2 of the fluctuation components. In Fig. 3.11(a) this idea is illustrated for one component with a width $l_{\parallel,1} = 200$ m and the other component with a width $l_{\parallel,2} = 15$ m.

Inserting two maxima of the cross-correlation $C_{max,i}$ at corresponding connection lengths $L_{c,i}$ (for $i = 1, 2$) into Eq. (3.2) and dividing these two equations we obtain

$$\frac{\phi_1}{\phi_2} = \frac{C_{max,1}}{C_{max,2}} = \exp\left(\frac{L_{c,2}^2 - L_{c,1}^2}{l_\parallel^2}\right). \tag{3.4}$$

Rearranging this for the parallel scale length yields

$$l_\parallel = \sqrt{\frac{L_{c,2}^2 - L_{c,1}^2}{\ln C_{max,1} - \ln C_{max,2}}}. \tag{3.5}$$

If one assumes an uncertainty of 5 % in the correlation shown in Fig. 3.10, the component with a long correlation length drops from at most $(C_{max,1} = 42 + 5)\%$ at $L_{c,1} = 23$ m to at least $C_{max,2} = (41 - 5)\%$ at $L_{c,2} = 66$ m, thus $l_{\parallel,long} > 120$ m. Inserting $l_{\parallel,long} = 120$ m, $L_{c,2} = 0.75$ m and the values for $L_{c,1}$ and $C_{max,1}$ from above in Eq. (3.4), one finds that the long correlation component would contribute at most 49% to the correlation at $L_c = 0.75$ m. Following the same reasoning, the component with short correlation length drops from at least 28% at $L_c = 0.75$ m to at most 10% at $L_c = 23$ m, yielding $l_{\parallel,short} < 23$ m. The widths

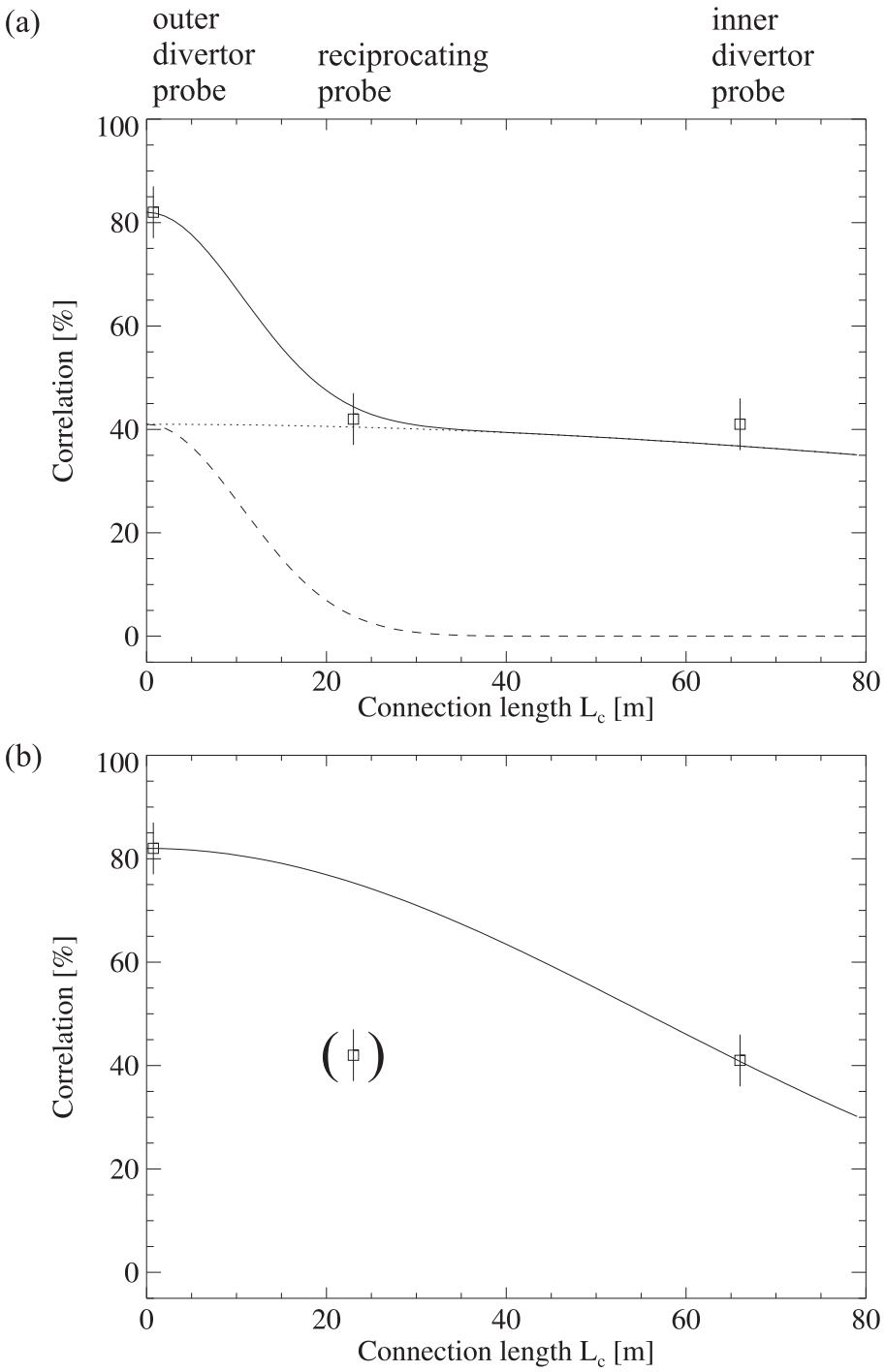

Figure 3.11.: *Maximum correlation versus the connection length. The squares denote the observed maximum values for the three available connection lengths on the JET tokamak. An error of 5 % is assumed for the experimental results. (a) The dotted curve is calculated from Eq. (3.2) with a parallel scale length* $l_{\parallel,1} = 200$ *m and an amplitude* $A_1 = 0.41$*. The dashed line is calculated the same way with* $l_{\parallel,2} = 15$ *m and* $A_2 = 0.41$*. The amplitudes of the two functions are chosen in a way that the sum (solid line) fits the experimental results for the* 0.75 *m connection. (b) Curve for a single fluctuation component according to Eq. (3.2) with* $l_{\parallel} = 79$ *m and* $A = 0.81$*.*

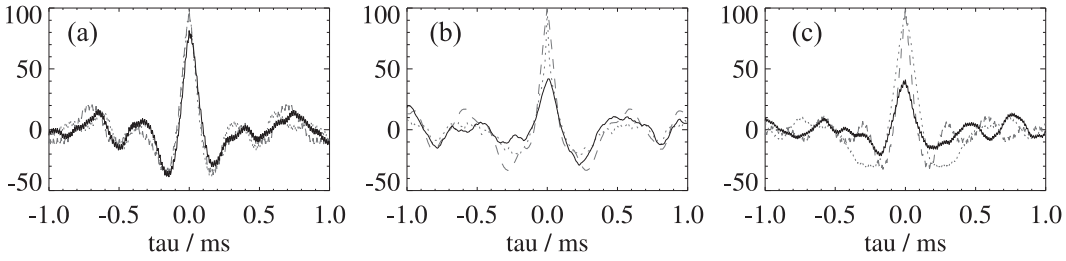

Figure 3.12.: *The cross-correlation (black) and the auto-correlation functions (grey) are plotted versus the time lag τ for the three available connection lengths on JET tokamak: (a) 0.75 m connection between two outer divertor probes. (b) 23 m connection between reciprocating (auto-correlation dotted) and outer divertor probe (auto-correlation dashed). (c) 66 m connection between inner (auto-correlation dotted) and outer divertor probe (auto-correlation dashed).*

of the parallel wave number distributions would be $\Delta k_{||,long} < 0.017\,\mathrm{m}^{-1}$ and $\Delta k_{||,short} > 0.09\,\mathrm{m}^{-1}$.

Another interpretation would be that there exists a component of the fluctuations which is only present in that part of the scrape-off layer which is represented by the reciprocating probe. Due to the normalization (2.17) of the cross-correlation function to the auto-correlation functions this would reduce the cross-correlation maximum at 23 m connection length with respect to the case where only one fluctuation component (with long parallel correlation length) was present. Under such assumption, one would estimate from Eq. (3.5) the parallel scale length $l_{||}$ from the cross-correlation maxima at 0.75 m and 66 m connection length to be $l_{||,long} = 79 \pm 13$ m [Fig. 3.11(b)]. This corresponds to a width of parallel wave number distribution $\Delta k_{||,long} = 0.025 \pm 0.005\,\mathrm{m}^{-1}$. In that case, nothing could be said about the parallel correlation length of the fluctuation component which would only be present in the region observed by the reciprocating probe.

In Fig. 3.12 the cross-correlation functions are shown with the corresponding auto-correlation functions for the three considered connection lengths on JET tokamak. As opposed to the presumption for single component model, the width of the auto-correlation functions differ only slightly from the width of the respective cross-correlation functions. Therefore, the assumption of two components in the parallel wave number spectrum seems to be more reasonable.

3.5. Consideration of the influence of errors on parallel correlation measurements on the JET tokamak

From preceeding discussions a parallel correlation length below 45% was obtained for a connection length of 23 m. For a longer connection length of 66 m, the observed maximum correlation does not further decrease. Basically, this is in agreement with the findings on Wendelstein 7-AS by Bleuel [1998] for a connection length of 35 m. However, it is important to identify any perturbative effects that could be responsible for this reduced correlation compared to the results obtained on various devices for connection lengths below 10 m and the 0.75 m connection length on the JET tokamak. In particular, the origin of the scatter in the results of the magnetic field line tracing (cf. Sec.3.3.1) must be considered.

3.5.1. Perturbations in the magnetic configuration

Results from the 66 m connection length parallel correlation measurements indicate, that a magnetic perturbation might be relevant for the interpretation of the results. One example for this can be seen in Fig. 3.13, showing the time evolution of cross-correlation (amplitude in grey scale) for the connection between the inner and outer divertor probes. The abscissa of this plot shows the time lag of the cross-correlation function, the ordinate denotes the division into time sub-windows of 10 ms length.

The decrease in correlation at $t = 70$—110 ms (marked by the digit ②) can be explained by the reciprocation of the top probe intersecting the connecting field line. However, there are variations in correlation to be seen along the time axis, which cannot be explained in simple terms (marked by digits ① and ③ in Fig. 3.13). The connected probes are stationary and the plasma conditions do not change either. Hence, the correlation function should be stationary as well.

In principle, perturbations in the magnetic configuration can cause a reduction in the magnitude and a change in the time lag of the correlation function. This is illustrated in Fig. 3.14. The changes in the magnetic configuration can only have an impact on parallel correlation measurements, if a magnetic field line starting at one of the outer divertor probes is displaced by the same poloidal distance at the position of the reciprocating probe as the typical poloidal scale length of the turbulence in the SOL (1—2 cm). In Fig. 3.15, a time series of the safety factor q_{95} is shown. The poloidal displacement of the field line is related to the safety factor q_{95}, compare Fig. 3.5. A change in q_{95} of 0.01 leads to a poloidal misalignment of a field line connecting an outer divertor probe and the reciprocating probe of 8 mm (Fig. 3.5).

The amplitude of the safety factor fluctuations in Fig. 3.15 is about 0.02. The

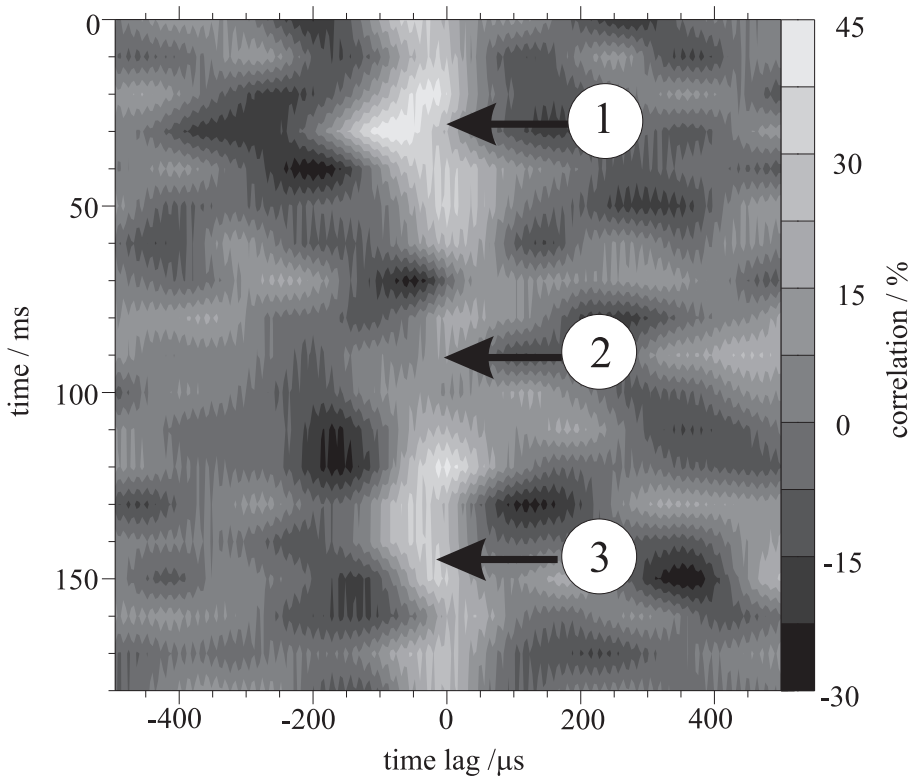

Figure 3.13.: *Time evolution of the cross-correlation of the established connection between one inner and one outer divertor probe (connection length: 66 m). ① and ③: Perturbations in plasma position and safety factor q_{95} could provide an explanation for the changes in correlation maximum and the discrepancies in the time lag. ②: The strong loss of correlation is due to the reciprocation of the probe head intersecting the connecting field line.*

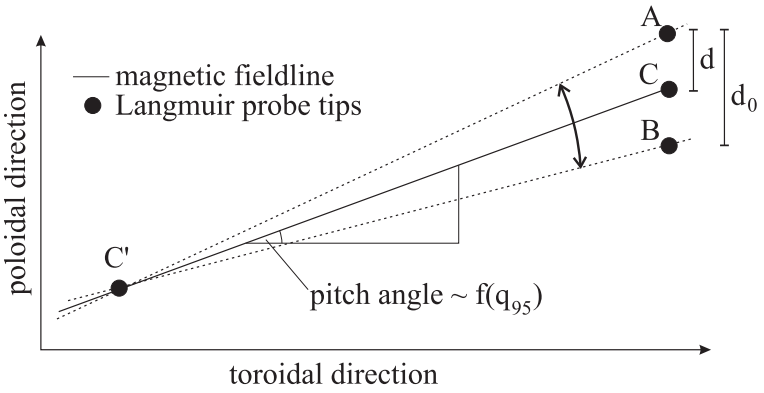

Figure 3.14.: *A reduction in the correlation could be caused by a (time-dependent) misalignment of the two probe tips. The arrow shows the poloidal displacement due to perturbations in the magnetic configuration. The pitch angle is a function of the safety factor q_{95}.*

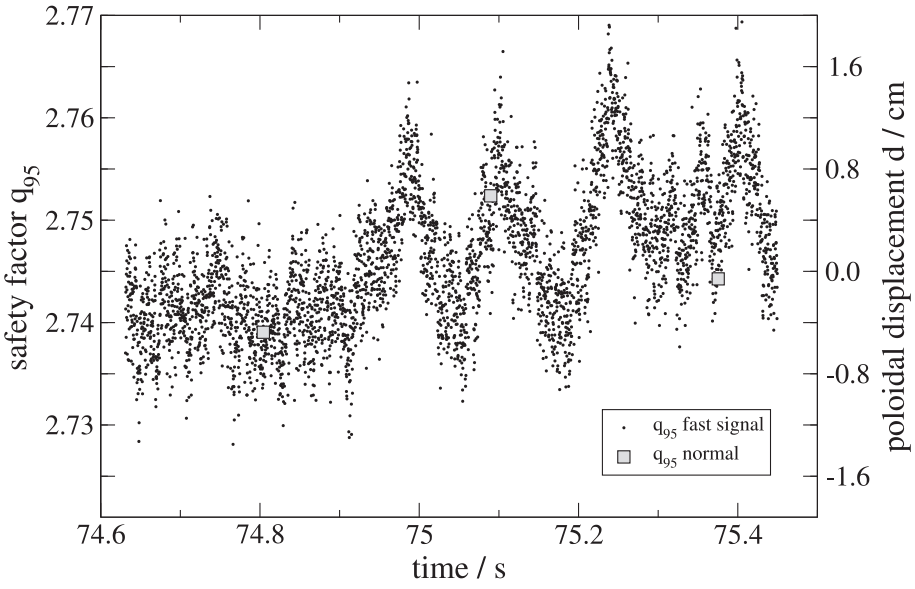

Figure 3.15.: *Time series of the safety factor. Black dots: safety factor signal q_{95} (calculated by the EFIT equilibrium reconstruction code) from a fast time window sampled with 5 kHz. Grey squares: q_{95} with default sample rate. Data from JET discharge #49729.*

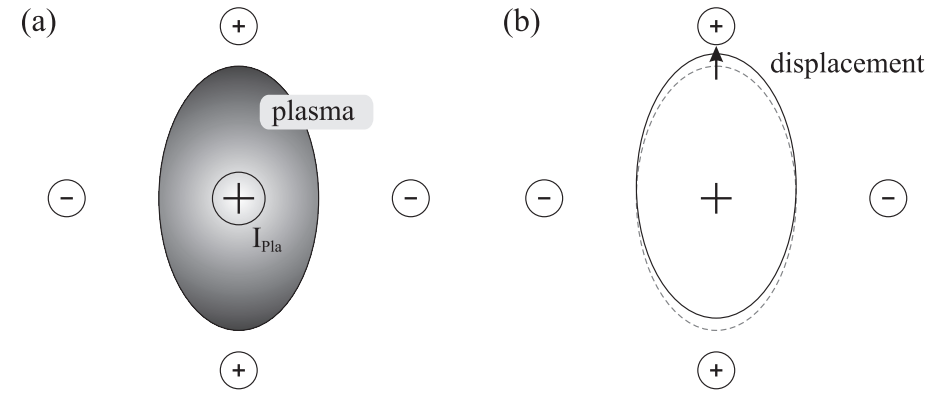

Figure 3.16.: *Two parallel currents in the same direction are attracted, whereas currents in opposite directions are repelled. This is the principle by that a tokamak plasma (carrying a strong toroidal current) can be elongated by means of external currents. (a) Poloidal sketch of the plasma shape with the direction of the plasma current I_{Pla} (+). The currents in the external coils force the plasma in its elongated shape. (b) The configuration is not stable: A small vertical displacement leads to an increasing force in the same direction as the displacement.*

corresponding poloidal shift of the connecting field line of 1.6 cm (cf. Sec. 3.3.1) is of the same size as the poloidal scale length of the fluctuations. In conclusion, the magnetic perturbations could indeed have a significant influence on the measurements.

3.5.2. The origin of the magnetic fluctuations

The vertical instability that occurs in elongated tokamak plasmas is the most likely reason for the perturbation in the magnetic configuration [Wesson 1997, chapter 6.15]. In tokamak plasmas, an elongation of the poloidal plasma shape is achieved by currents through external toroidal coils (Fig. 3.16). However, the elongated plasma equilibrium is not stable in the direction of the elongation. The external currents are feed-back regulated (the control parameter is the vertical plasma position) in order to account for any vertical plasma movement. The vertical instability typically evolves on a time scale in the order of one millisecond, depending on the plasma elongation and the resistivity of the wall [Wesson 1997, chapter 6.15].

There is a high correlation ($> 70\%$) between the vertical plasma position and the fluctuations of the safety factor in the frequency range below 1 kHz (Fig. 3.17). This time scale is consistent with the expectations for the vertical instability of the JET plasma [Perrone and Wesson 1981]. Since there is no correlation with the vertical instability on the faster time scale, one might suspect that the apparent fast magnetic flutter is just noise pick-up by the magnetic probes.

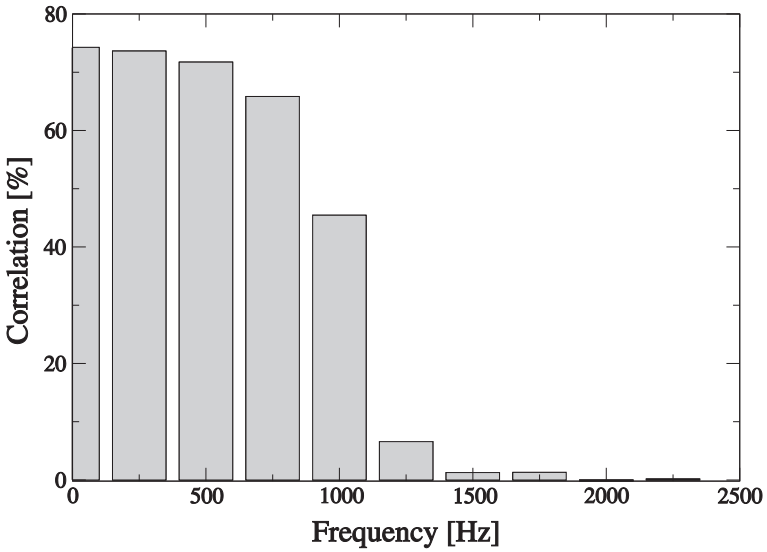

Figure 3.17.: *Correlation of the vertical plasma movement with the safety factor q_{95} calculated for different frequency bands.*

3.5.3. A simple perturbation model: basic model assumptions

During the parallel correlation studies the ion saturation current was collected in a 100 ms time window. Therefore, dynamics on a slower time scale than 100 ms are not important for this analysis. Magnetic fluctuations on a time scale from 10—100 ms could explain findings of the previous campaign, which were not understood so far, (Sec. 3.5.1 and Fig. 3.13).

Since the magnetic data were not collected with sufficiently high sampling rate during the discharges with fast Langmuir probe measurements, this hypothesis cannot be tested directly. Instead, a simple model is discussed for an estimation of the effect that the perturbations of the plasma position and safety factor could have on the parallel correlation measurements.

Basically, the changes to a fluctuation time series is calculated on the basis of the assumptions detailed below by Eq. (3.6). Then, the cross-correlation of this perturbed signal with the original signal can be compared with the results from the parallel correlation studies. If the simulated and the real cross-correlation show similar properties (especially comparable correlation maxima), the found reduction in correlation will most likely be caused by the perturbations in the magnetics.

Basic assumptions:

1. The fluctuations have a perfect correlation along the magnetic field lines (2d turbulence).

2. The fluctuations have a poloidal extent of 1.5 cm as suggested by the cor-

relation functions between poloidally displaced probe tips in the divertor.

3. The turbulence has no different properties in terms of scale length in radial and poloidal direction, so radial changes are not treated separately.

4. Fluctuations propagate poloidally owing to $\mathbf{E} \times \mathbf{B}$ plasma rotation. Dependent on the poloidal distance, the fluctuations arrive with a delay or in advance. This velocity v_θ of the poloidal plasma rotation is estimated from the two probes in the outer divertor which are separated by $d_0 = 1.5\,\mathrm{cm}$ poloidally and $0.87\,\mathrm{cm}$ radially. The time lag τ_0 of the cross-correlation function between the signals from these two probes is determined to be $\tau_0 = 120\,\mu\mathrm{s}$ and thus $v_p \approx 125\,\mathrm{m}/\mu\mathrm{s}$.

5. The fluctuations in a poloidal vicinity of a probe can be calculated by interpolation between the signals from two poloidally separated probes. The influence of each of the two signals is weighted by using different assumptions of the poloidal shape of the fluctuations[3].

The correlation between the signals measured by the two probes is assumed to depend on the poloidal distance only. Let $\tilde{f}_A(t)$ and $\tilde{f}_B(t)$ be the fluctuation signals at the probe tips A and B (Fig. 3.14), which are separated by a poloidal distance d_0. The signal at a probe C located between A and B would be given by

$$\tilde{f}_C(t) = g(d) \cdot \tilde{f}_A\left(t + \frac{d}{v_\theta}\right) + [1 - g(d)] \cdot f_B\left(t - \frac{d_0 - d}{v_\theta}\right), \quad \text{for } 0 \le d \le d_0. \tag{3.6}$$

In Eq. (3.6) the function $g(d)$ is the poloidal shape of the fluctuations and v_θ is the poloidal velocity. A perturbation in the magnetic configuration bends the field line, leading to a time dependent poloidal displacement $d = d(t)$.

3.5.4. Application of the model

In Fig. 3.18(a,b), the time evolution of the cross-correlation function between $f_A(t)$ and $f_C(t)$ is shown for two different interpolation functions

$$g_1(d) = \exp\left(-\frac{2 \cdot d^2}{\mathrm{cm}^2}\right) \quad \text{(Gaussian shape)} \tag{3.7}$$

and

$$g_2(d) = \exp\left(-\frac{|3 \cdot d|}{\mathrm{cm}}\right) \quad \text{(exponential shape)}. \tag{3.8}$$

[3]Measurements in different devices with poloidally highly resolved probe arrays show a Gaussian shape, cf. Fig. 2.4

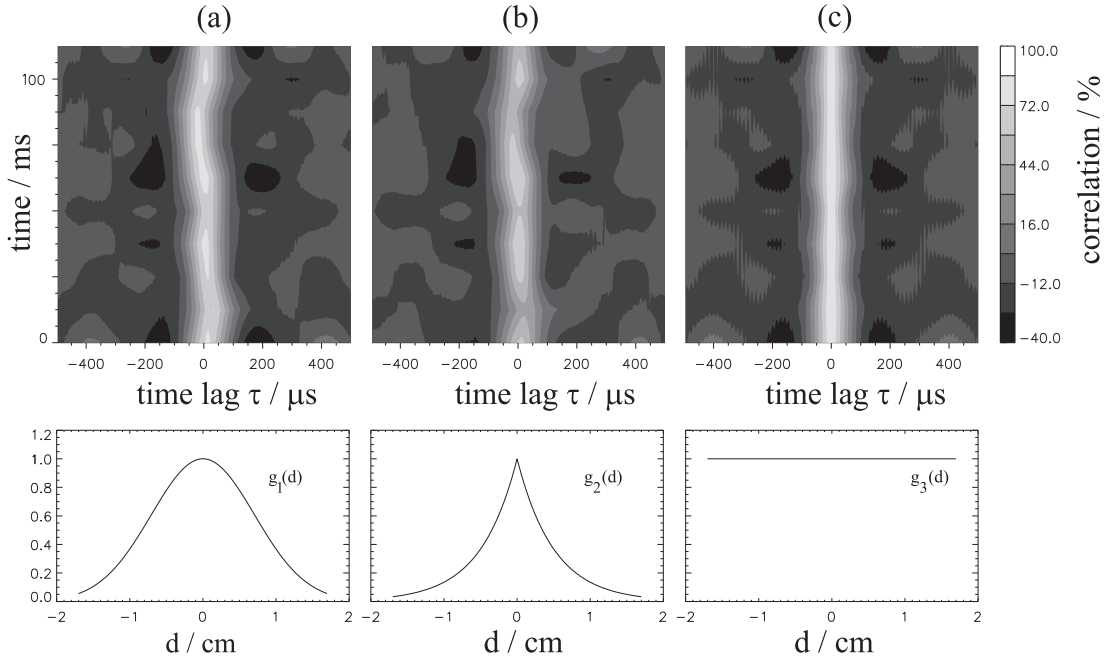

Figure 3.18.: *Time evolution of the cross-correlation between a probe signal $f_A(t)$ and a model signal $f_C(t)$ constructed according to Eq. (3.6) with the interpolation functions $g(d) = g_1(d)$ a Gaussian shape (a) and $g(d) = g_2(d)$ an exponential decay (b). The auto-correlation of f_A is given for comparison (c).*

The factors in these functions are chosen in a way that (within an error of 2%) $f_C(t) = f_A(t)$ for $d(t) = 0$ cm and $f_C(t) = f_B(t)$ for $d(t) = d_0 = 1.7\,\mathrm{cm}$. The Langmuir probe signals $f_A(t)$ and $f_B(t)$ are taken from JET discharge #46796. The magnetic field line displacement signal $d(t)$ used in the construction of $f_C(t)$ had to be taken from a different discharge with similar conditions (#49699), since no fast sampled magnetic signals were available during the parallel correlation study.

A reduction of the cross-correlation maximum to approximately $90 - 80\%$ is obtained for the correlation between $f_A(t)$ and $f_C(t)$ using $g_1(d)$ and a reduction of the maximum to 80—60% with the use of $g_2(d)$. The correlation plots qualitatively show similar perturbations to those found in experimental data (Fig. 3.13). For both poloidal shapes, the temporal shift in the time is in the order of $\tau = \pm 40\,\mu\mathrm{s}$. This is the same order of magnitude as the results from the experimental data (Fig. 3.13). However, the maximal correlations obtained by the simulation are still well above the correlations observed in the experiment for the connection lengths of 23 and 66 m. The assumption of an exponential shape of $g(d)$ in (b) should be seen as a worst-case scenario, not based on any physical evidence. The poloidal shapes found in other experiments like Caltech

tokamak [Zweben and Gould 1985] and Wendelstein 7-AS stellarator Bleuel [1998] resemble a Gaussian (cf. Sec. 2.2.3). Therefore, the reduction of the correlation caused by the perturbations in the magnetic configuration would be in the order of only 10—20%. The dramatic reduction in correlation below 50% at connection lengths larger than 20 m (Sec. 3.3) cannot be explained by these perturbations alone. According to this simple model, the major part of the reduction in correlation must have its origin in the genuine physical properties of the turbulence in the SOL.

3.6. Discussion

3.6.1. The reduction of parallel correlation

In summary the parallel correlation study on the JET tokamak gave the following experimental results: At short connection of 75 cm, a high correlation degree $\geq 80\%$ was obtained. At much longer connection lengths of 23 m and 66 m a reduction of the correlation below 50% is observed. A possible interpretation is that two distinctive components may contribute simultaneously to the parallel dynamics: One component is damped away within the connection of length $L_c \leq 20$ m, whereas the other component is damped at a much longer decay length parallel to the magnetic field, if at all, and could be attributed to a fluctuating convective cell with $k_{||} = 0$. This picture is supported by the fact, that the fluctuations at distant probes have virtually no phase shift. It is observed in the coherency and phase spectra [Fig. 3.10(a-c)], that only the low frequency part up to 10 kHz accounts for correlation.

The above interpretation relies very sensitively on the accuracy of the experimental results: If anything else rather than the inherent dynamics of the turbulence in the scrape-off layer is responsible for the correlation reduction along the magnetic field, this picture is clearly misleading. Therefore, other influences that might lead to de-correlation were carefully considered and discussed in Sec. 3.5. The analysis of a q_{95} signal revealed that the rather high noise level on the signal can be attributed to the vertical plasma movement at frequencies up to approximately 1 kHz. This movement is caused by the vertical instability, which occurs in elongated tokamak plasmas. It is found in a simple model, that the perturbation of the magnetic configuration due to the vertical instability can account for a minor part of the correlation reduction, only.

3.6.2. Influence of the X-point passage

The passage of the magnetic field line near the X-point of JET could also have an influence on the parallel correlation of the fluctuations: In numeric simulations

by Xu et al. [2000], a strong poloidal variation of the transport probably caused by resistive X-point modes were found. On JET it is not possible to establish a connection shorter than 23 m with a field line passing the X-point. Thus, a clear-cut experimental answer on this point cannot be given. However, the fact that the correlation is not further reduced at the long connection of 66 m (and the second passage of an X-point) does not support the numerically obtained findings by Xu et al. [2000]. This conclusion is also supported by previous studies on ASDEX [Rudyj et al. 1989, 1990; Rudyj 1990; Bleuel et al. 1996; Bleuel 1998].

3.6.3. What has been gained?

Coming back to the main questions raised in Sec. 3.1.3: From the parallel correlation experiments on the JET tokamak it seems to be likely that a significant reduction in cross-correlation below 50% for long connection lengths (23 m and 66 m in the case of JET and 32 m in the case of W7-AS) is indeed an inherent property of plasma boundary turbulence. Two previously proposed reasons for this reduction (Sec. 3.1) can already be excluded:

- Influence of magnetic curvature, i.e. passage of the connecting field line through regions of favorable magnetic curvature: The correlation obtained on JET tokamak for the 23 m outboard connection with the connecting field line embedded in the region of unfavorable magnetic curvature is below 50%. Moreover, the correlation is not further reduced for the 66 m connection, in which a significant fraction of the connecting field line is embedded in the favorable curvature region.

- Boundary conditions, i.e. confinement zone versus scrape-off layer: In the JET tokamak, measurements where exclusively performed in the SOL. Hence, the reduction of the correlation is not specific for the confinement zone. Moreover, the probes do not significantly change the boundary conditions in the scrape-off layer, as it might be the case for measurements with probes in the plasma core.

Let us consider the four heuristic models proposed for the fluctuation dynamics in parallel direction again (cf. Sec. 3.1.2). The time lags of the correlation maxima are practically zero for all three connection lengths on JET (Fig. 3.12). Hence, the model considering fluctuation events which preferably occur at a specific position alongside the magnetic field line can be excluded. The widths of the observed auto-correlation and cross-correlation functions are comparable (Fig. 3.12). This is expected for the heuristic model that considers filaments with a constant inclination with respect to the magnetic field.

Filament structures with zero parallel wave number are equivalent to the concept of convective cells. It was already pointed out in Sec. 1.3.4, that three-dimensional drift wave simulations suggest convective cells as a dominant mode,

however, for an unsheared magnetic field only [Biskamp and Zeiler 1995; Zeiler et al. 1996; Scott 1997a]. In the experiment, it was possible to estimate the limits for the average parallel wave number $0 \leq |\overline{k}_{\|}| < 0.16\,\mathrm{m}^{-1}$ for the 23 m connection length on JET. Hence, the observed parallel wave number is in qualitative agreement with the findings from numerical modeling. A detailed quantitative comparison between the experimental results and dedicated numerical drift wave simulation would be very interesting for a deeper insight into plasma edge turbulence.

3.6.4. Conclusions on parallel correlations in JET

The parallel correlation measurements of ion saturation current fluctuations conducted in JET tokamak revealed a significant decrease of correlation from $\geq 80\%$ for a connection length of 75 cm in the divertor to about 40% for a connection length of 23 m between divertor and SOL on top of the plasma along the low-field side of the torus. The decrease is due to a reduction of coherency at frequencies < 10 kHz (where most of the fluctuating power is located) from approximately 90% to less than 50%. For the longest achievable connection length of 66 m, no further reduction of the correlation level was observed, although the flux tube now passes the torus high-field side and, for a second time, the X-point. It appears, therefore, that there exists one component of the fluctuations with a correlation length parallel to the magnetic field of about 20 m, which cannot be treated appropriately in the framework of a two-dimensional model. As a matter of fact three dimensional dynamics are expected for drift waves. A second component of the fluctuations has a parallel correlation length greater than 70 m and a narrower frequency spectrum, which could be described within the scope of a two-dimensional model (although a three-dimensional treatment may be required to understand the origin of this long correlation length). The presence of a region of good magnetic curvature on the torus' high-field side has no influence on this second component.

Whether the X-point plays a role in the correlation suppression for increasing connection length (0.75—23 m) or not is hard to answer on the basis of experimental JET data. In conjunction with previous findings, e.g. on the ASDEX tokamak, such a one-to-one relationship is not very likely.

Estimates for the upper limits for the average parallel wave number were obtained to be $|\overline{k}_{\|}| < 0.16\,\mathrm{m}^{-1}$. The ratio between the average wave numbers parallel and perpendicular to the magnetic field is $|\overline{k}_{\|}/\overline{k}_{\perp}| < 0.0022$. Within the error bars, the obtained results are compatible with the common assumption of parallel wavenumber $\overline{k}_{\|} = 0$.

4. Active modification of turbulence

In this chapter results from experiments on the Wendelstein 7-AS stellarator are presented. The basic idea is to use external signals applied to the plasma as a new approach to turbulence diagnostics. The signals are introduced into the plasma edge by usual Langmuir probe tips. The plasma response is detected in poloidal direction as well as parallel to the magnetic field by other Langmuir probes. In this way, the parallel and the poloidal propagation of the perturbation signal can be observed and is set into the context of the background turbulence. As a first step, only one single external signal was injected into the plasma, mainly for studying the poloidal signal propagation. In a second step, phase-shifted signals were applied to a set of probe tips, allowing to introduce spatio-temporal signals into the plasma boundary.

The experiments on Wendelstein 7-AS stellarator discussed in the present work focus on active probe studies. A comprehensive characterization of the electrostatic turbulence in the plasma boundary of Wendelstein 7-AS by means of Langmuir probe diagnostics can be found in the thesis by Bleuel [1998]. A difference between these experiments and present ones is given by the recent installation of an island divertor [Grigull et al. 2001; Gadelmeier et al. 2001].

This chapter is organized as follows: In Section 4.1 the active probing results on the TEXT tokamak, the Keda Tokamak-5C and the MIRABELLE linear device are discussed. The experimental set-up on Wendelstein 7-AS and field line tracing calculations are described in Section 4.2. Parallel correlation studies on W7-AS follow in Section 4.3. The results from the two previous sections form the basis for the experiments conducted with an active probe set-up. The results are presented in Section 4.4 for the case of a single active signal and in Section 4.5 for the active feeding of spatio-temporal patterns on W7-AS. The results presented in this chapter are summarized and discussed in Section 4.6.

4.1. Results from other experiments

On the TEXT tokamak, experiments were conducted with the aim to modify the plasma edge turbulence by means of active probing [Uckan et al. 1993, 1995; Richards et al. 1994; Winslow et al. 1997, 1998]. In that series of experiments, two driver tips of a probe were operated with external signals in the frequency range of 10—250 kHz and voltages up to 60 V (AC) with an additional bias of

+50 V. The probe was located in the limiter shadow and each tip was capable of collecting currents up to 15 A. A floating potential signal picked up by a movable probe was amplified and fed back with a predefined phase-shift into two driver tips. Depending on gain and phase between the two driver probes, either a decrease of the fluctuation level in the respective flux tube of up to 50%, or an increase by a factor of 10 were reported by Richards et al. [1994].

Particularly interesting results with regard to the parallel dynamics of active signals in the plasma boundary were obtained with the following set-up on TEXT: One driver tip was connected to a sine signal (30 kHz) of a signal generator and the propagation of this signal in the plasma was studied with a poloidal probe array located at a certain toroidal distance (connection length 12 m). The signals are found to propagate parallel to the magnetic flux tube with a velocity close to the Alfvén velocity [Uckan et al. 1995]. However, a striking asymmetry of the parallel propagation was observed: For a set-up with reversed magnetic field and plasma current, no signal was detected. This asymmetry might simply be caused by an intersection of the flux tube with a limiter [Winslow et al. 1998].

Similar experiments conducted in the Keda tokamak 5C (KT-5C) reproduced this asymmetry of signal propagation parallel to the magnetic field (connection length of 3 m) [Kan et al. 1997]. The parallel velocity, however, was found to be much slower than the Alfvén velocity. There, the parallel asymmetry and the slow velocity of the signal propagation was interpreted to be closely related to the toroidal plasma current, i.e. the signal is assumed to be carried by the electron directional movement, only. This explanation cannot be valid for the TEXT experiments, since the signal propagation velocity was higher. Moreover, the signal was detected in the direction of the plasma current, whereas on KT-5C the signal was found to propagate in the opposite direction.

Taking this rather confused situation into account, a series of experiments on the Wendelstein 7-AS, to be discussed in this chapter, addresses the two main questions, i.e. the estimation of the propagation velocity of externally applied signals and possible asymmetries in the signal propagation.

A different aspect of the experiments is motivated by recent results from a laboratory plasma device: In the linear configuration MIRABELLE, a single drift mode could be selectively amplified on the expense of the initially broad turbulence spectrum by means of an open-loop synchronization [Schröder et al. 2001]. The experiments were carried out using an azimuthal octupole exciter electrode enclosing the plasma column, which permit the creation of a mode-structured perturbation field. Stabilization of a preselected drift mode was achieved for the case of the co-rotation of the perturbation field with the drift modes.

Such experiments have not yet been conducted in stellarators and tokamaks. Nonetheless, the plasma boundary of these devices allows one to introduce large probe arrays without significantly perturbing the plasma core. The application of spatio-temporal signals is a promising approach for gaining new insight into the

plasma boundary turbulence of stellarators and tokamaks. The waves launched that way can be seen as 'test waves' in a turbulent background analog to the picture of test charges in an electric field.

4.2. Set-up on Wendelstein 7-AS

The plasma discharge conditions and set-up for the experiments performed on the Wendelstein 7-AS stellarator will be described in this section. The main magnetic field was 2.5 T with no vertical field. The plasma was heated by 0.5 MW electron-cyclotron heating. The central temperature was 1.5 keV and the line average density was $1 \cdot 10^{19}\,\mathrm{m}^{-2}$.

4.2.1. The probe arrays

Two Langmuir probe arrays were used for the experiments. One array was located on the inboard side of module two and the other on the outboard side of the same module (see Fig. 4.1). The inner array consists of 24 probe heads covering the whole inner side of the flux surface with a poloidal probe distance of 2 cm. For technical reasons, only the probe heads in the lower half of the array where available during this experimental campaign. Two of the heads were fitted with probe triples (tip distance 2 mm) and on the other heads single probes were installed. In total, 16 probe tips on 12 probe heads (numbers [0] to [11]) of the inner array were available for data acquisition [Fig. 4.1(d)]. The radial position of the inner array was fixed to be approximately 1 cm outside the last closed magnetic flux surface. The outer probe array consists of 28 tips with a poloidal probe distance of 2.5 mm. Due to limitations of the number of channels of the data acquisition system, only 24 signals could be recorded from the probe tips with numbers [A] to [X] [Fig. 4.1(e)]. The outer array was mounted on a reciprocation system. During each discharge a radial scan of 10 cm was performed.

4.2.2. Magnetic alignment of the inner and outer probe array

By adjusting the magnetic configuration (in particular the rotational transform ι), it was possible to align some tips of the inner and outer probe arrays along a magnetic flux tube. Fig. 4.2 shows the result from numerical field line tracing calculations for the rotational transform $\iota = 0.40$ at two different poloidal cross-sections (see below). The magnetic flux surfaces (solid lines) are plotted in the $R - Z$ plane and the LCFS is marked by the dashed curve.

Fig. 4.2(a) shows the poloidal cross-section at the toroidal angle $\Phi = 46.6°$, where the outer reciprocation probe is installed. The area highlighted by the grey box is magnified in Fig. 4.2(c). The position of the poloidal probe array

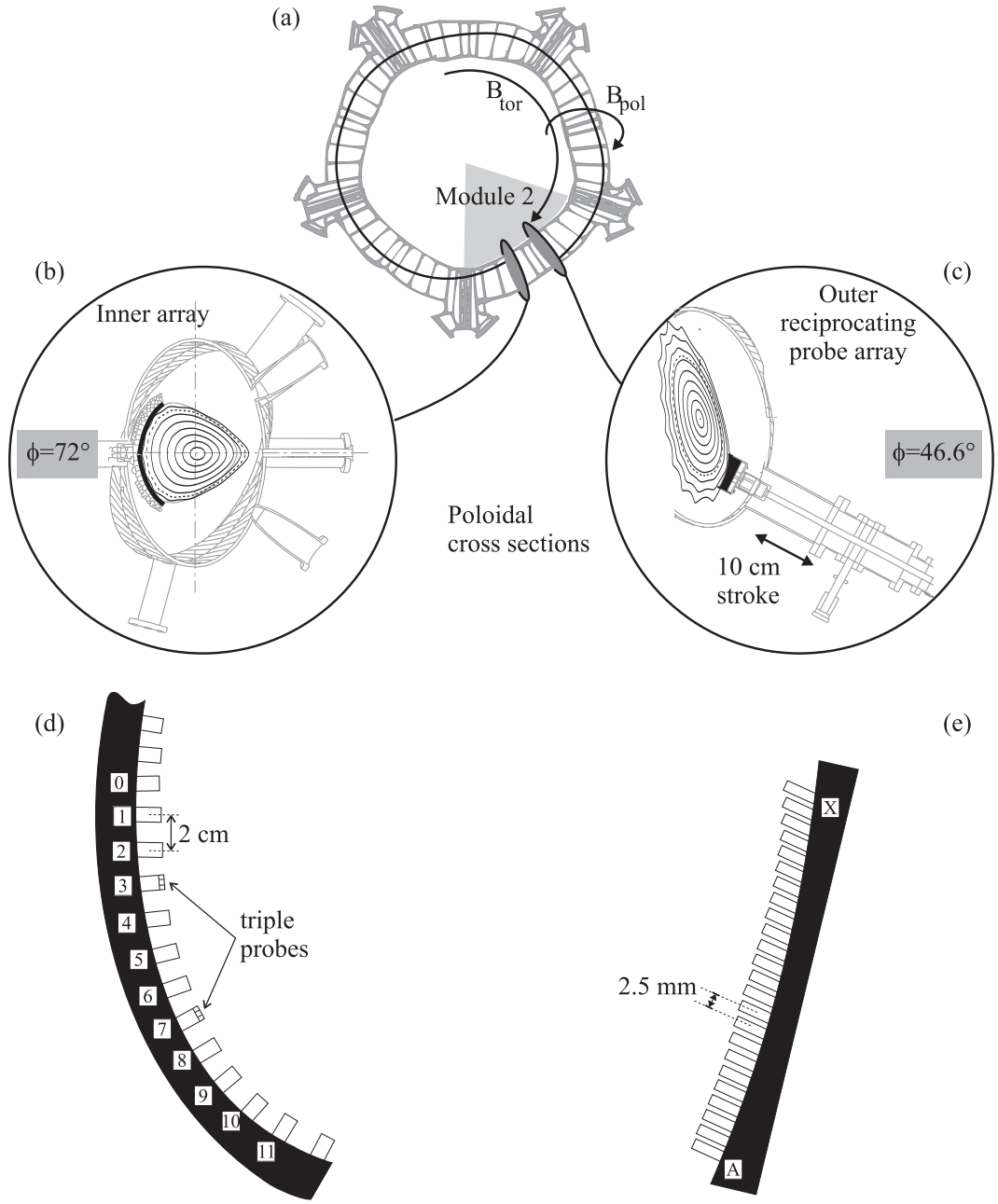

Figure 4.1.: *Experimental set-up on Wendelstein 7-AS. (a) The top view of the torus and the positions of the probe arrays. The inner array is installed at a toroidal angle of 72° and the outer reciprocating probe is located at a toroidal angle of 46.6°. The insets (b) and (c) show the poloidal cross sections of the inner and the outer probe array (colored in black). The shapes of both arrays are aligned to the magnetic flux surfaces. The dashed line denominates the position of the separatrix. (d) Sketch of the inner probe array and the numbering of the probe heads. (e) Sketch of the outer reciprocating probe array and the numbering of the probe tips.*

is sketched in grey. The starting positions for the field line tracing are chosen according to the poloidal positions of the measuring probe tips [A] to [X] during a reciprocation of the outer probe array. These starting positions (denoted by open squares) thus form a two-dimensional field in the poloidal cross-section. This field is marked by ⓪.

In Fig. 4.2(b) the poloidal cross-section at the toroidal angle $\Phi = 72°$ (where the inner probe array is located) is plotted. The field line tracing maps the array of starting positions ⓪ at the toroidal angle $\Phi = 46.6°$ along the magnetic field lines (black arrows). The number of toroidal turns is indicated by the numbers in circles, ① to ④. The area highlighted by the grey box is magnified in Fig. 4.2(d). The inner array is plotted in grey and the positions of the probe heads are denoted by filled black circles. After one toroidal turn (①) the starting positions are mapped onto the probe heads [3] [4] [5] of the inner array (open squares). According to the field line tracing for the rotational transform $\iota = 0.40$ probe head [3] of the inner array is connected by a magnetic field line to probe tip [A] of the outer array for a certain radial position of the outer probe head. Probe tip [X] is mapped between heads [5] and [6] of the inner array. The squares at the inner probe array displayed in light grey [Fig. 4.2 (b) and (d)] would not actually denote a connection to the outer array, since the corresponding field lines are intersected by in-vessel components (the divertor or baffle target plates).

4.2.3. Active probing techniques

The modulation signals are introduced into the plasma edge via Langmuir probes of the outer array. This method provides a rather flexible set-up, since it is possible to apply the signals to a subset of probe tips (active probes) only and use the remaining probe tips as ordinary Langmuir probes. The disadvantage is that the allowable currents through the probe tips have to be below a certain threshold in order to avoid damage on the probe tips. The maximum current per probe tip is 1 A. Since the used amplifier units have an output current of 2 A per channel, each of the six amplifiers was applied to drive one pair of probe tips. For the creation of wave signals, the output of three phase-locked signal generators and their inverse output are used. This way, six sine signals with a fixed phase relation can be generated. As shown in Fig. 4.3, it is possible to feed a spatially propagating wave signal (at a selectable frequency) to the outer probe array. The phase-shift $\Delta\varphi$ was selected to be 60°, −60° or 0°. For a phase-shift $\Delta\varphi = 60°$ and $\Delta\varphi = -60°$, the propagation is in opposite direction. The output shows only temporal variation but no spatial propagation of the signals for $\Delta\varphi = 0°$. The voltages and currents of the active and passive probes were synchronously sampled at 2.5 MHz.

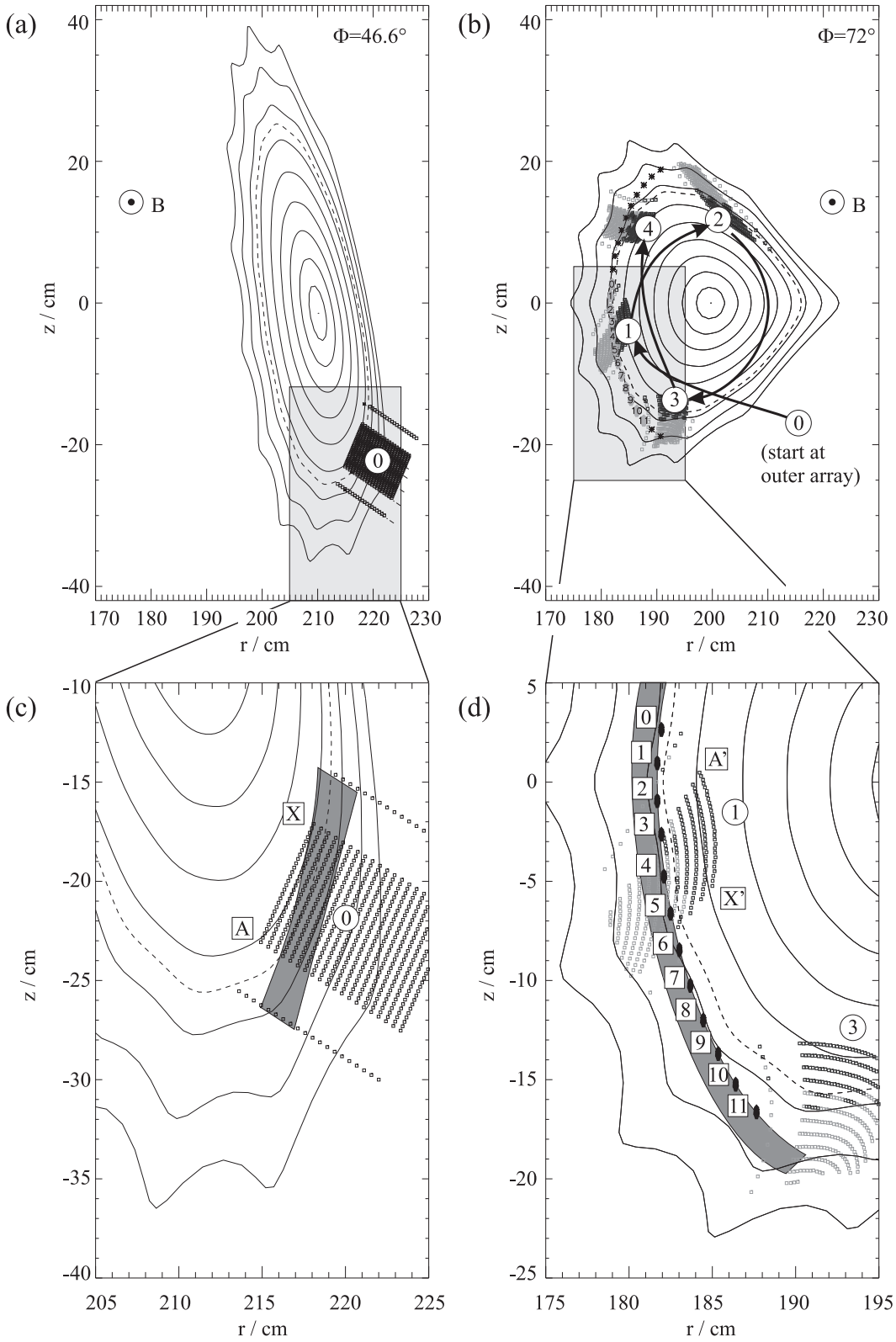

Figure 4.2.: *Results from field line tracing opposite to the toroidal magnetic field for a magnetic configuration with a rotational transform $\iota = 0.40$. Detailed description in the text.*

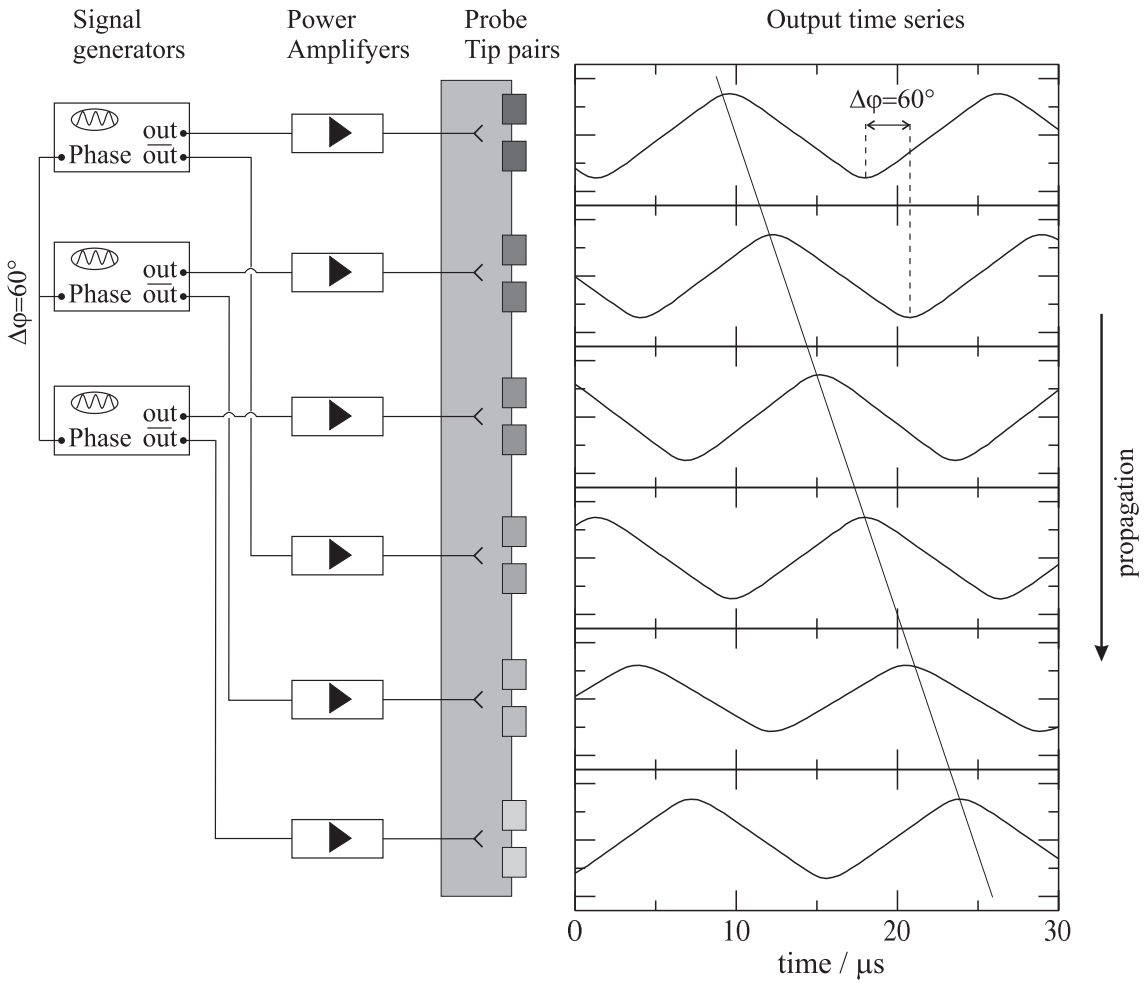

Figure 4.3.: *Output time series from three phase-locked signal generators with a phase-shift of $\Delta\varphi = 60°$ between each signal. The direct output (out) and the inverse output ($\overline{out}$) of the three signal generators are amplified and applied to six probe tip pairs. Thus, a wave pattern is generated which propagates along the poloidal array. The propagation direction is given by the sign of the phase-shift.*

4.3. Parallel correlation measurements on Wendelstein 7-AS

Experiments on the Wendelstein 7-AS stellarator with all probe tips of inner and outer array assessing floating potential were performed in order to check the agreement between parallel correlation measurement and the (vacuum) field line tracing.

4.3.1. Parallel correlation between inner and outer array probes

Fig. 4.4(a) shows the cross-correlation between tips of the inner array (0 to 11) with tips from the outer array (A to X) for a time lag $\tau = 1.2\,\mu$s. For this time lag, the maximum cross-correlation was observed. The data is filtered with a 10 kHz high-pass before the correlation analysis. From the contour of maximum correlation (marked by a white ellipse in Fig. 4.4), the mapping between the tips on the outer probe array onto the tips of the inner array can be determined. The tips from the outer array map on the tip numbers 3 4 5 6 of the inner array. This finding is in good agreement with the result from vacuum field line tracing (compare Sec. 4.2.2).

The correlation amplitude has comparatively low value (23% only). This might be due to the 10 kHz high-pass filter, which is used to damp a low-frequent perturbation in the data: Without high-pass filtering, all tips from the inner array seem to have a correlation of about 50 % with the tips from the outer array [Fig. 4.5(a)]. A closer look at the data reveals an oscillatory signal in the low-frequency range of 1—5 kHz which dominates the auto- and cross-correlation functions [compare Fig. 4.5(b)]. This signal is found on both the tips of the inner and the outer probe array. If the reciprocating probe array is on a position far outside, the signal vanishes. This finding suggests that the low-frequent signal is due to an actual plasma mode. The mode is detectable on the outer probe array as well as on the inner array with zero time lag which indicates a global plasma mode. The origin of this phenomenon is not yet resolved and requires further investigation. For the further analysis within the scope of this work, it is sufficient to filter the data with a 10 kHz high-pass. This limit frequency is well below the frequencies used for the active probe set-up described in the following sections.

4.3.2. Parallel wave number on Wendelstein 7-AS

The maximum correlation is found for approximately zero time lag. We can estimate the parallel wave number by Eq. (2.22). Field line tracing (Fig 4.2) yields a

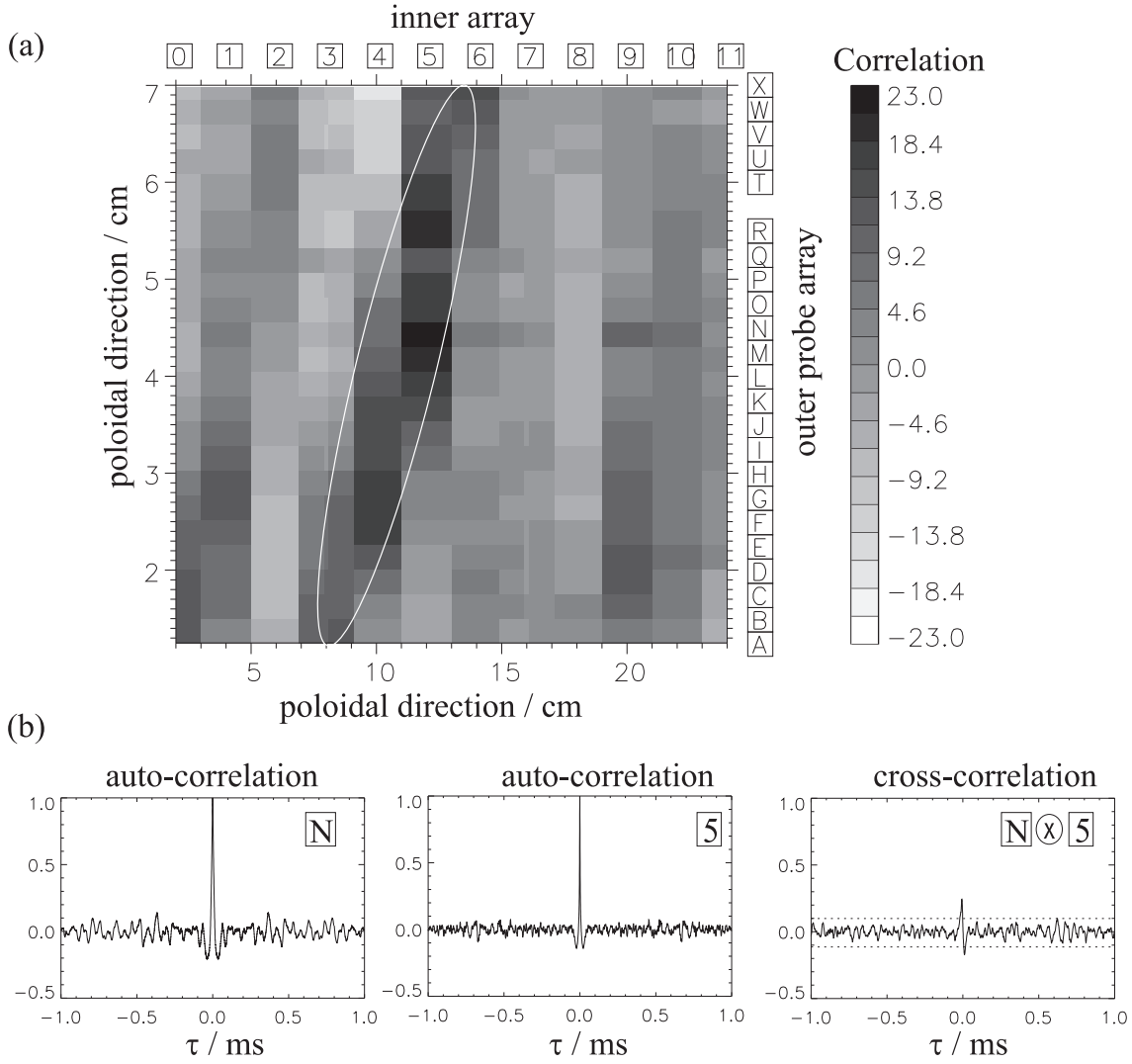

Figure 4.4.: *Data filtered with 10 kHz high-pass before the correlation analysis. (a) Cross-correlation between the signals from the probe tips of the inner array (horizontal axis) and the signals from the probe tips of the outer array (vertical axis). Probes* 3 *and* 7 *of the inner array are triple probes. The correlation for time tag* $\tau = 1.2\,\mu s$ *is shown in grey scale. The white line is drawn to guide the eye. (b) The auto-correlation of the outer probe tip* 5*, the auto-correlation of the inner probe tip* N *and the cross-correlation between the respective tips is plotted versus time lag* τ*. Data from W7-AS discharge #50196.*

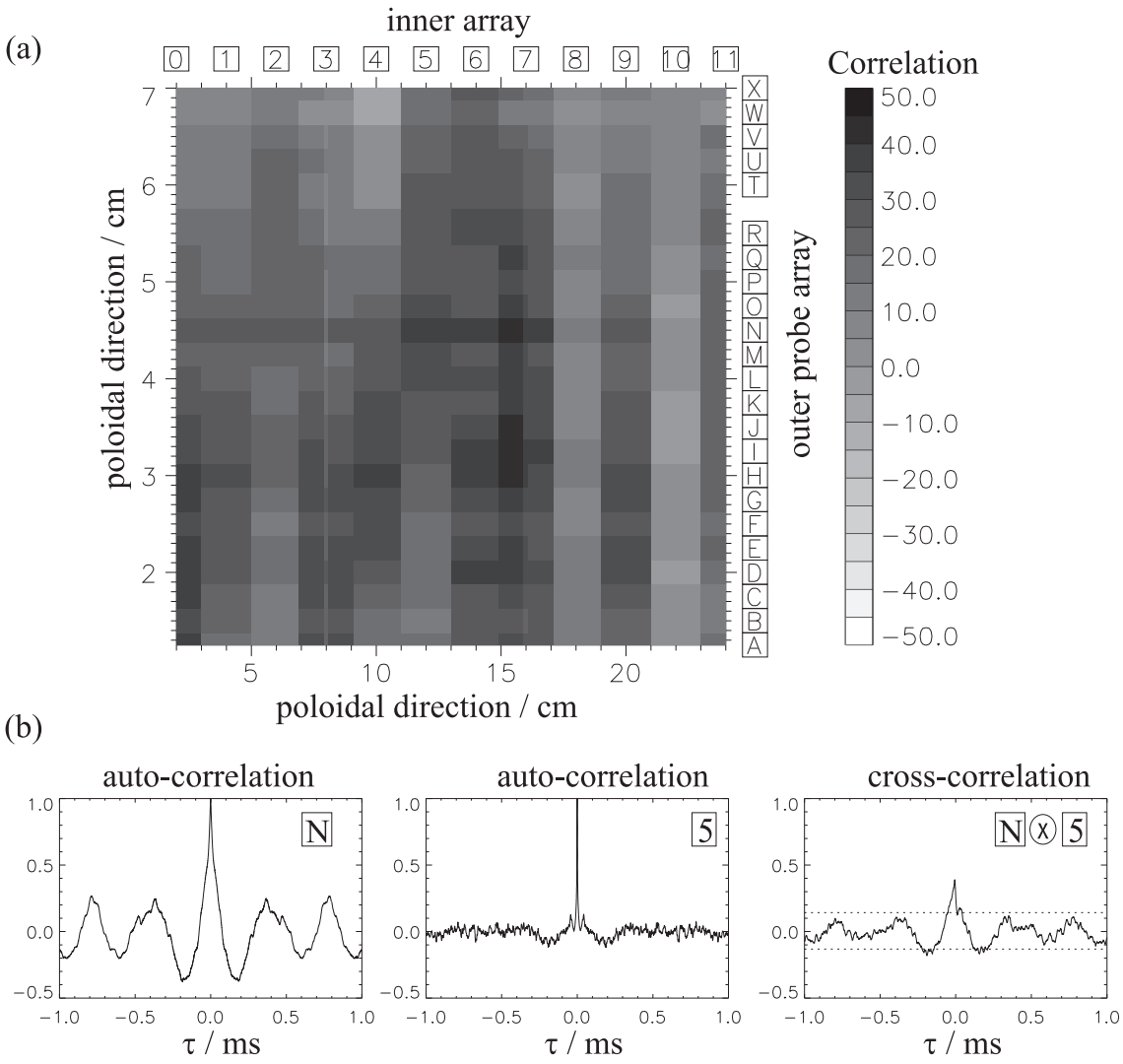

Figure 4.5.: *(a) Cross-correlation between the signals from the probe tips of the inner array (horizontal axis) and the signals from the probe tips of the outer array (vertical axis). The correlation for time tag $\tau = 1.2\,\mu s$ is shown in grey scale. (b) The auto-correlation of the outer probe tip* $\boxed{5}$*, the auto-correlation of the inner probe tip* $\boxed{N}$ *and the cross-correlation between the respective tips is plotted versus time lag τ. In comparison with Fig. 4.5(b), the low-frequent oscillation is clearly seen. Data from W7-AS discharge #50196.*

parallel mapping of tip N to the toroidal plane of the inner array onto a position that is approximately half between probes 4 and 5. The maximum correlation was experimentally found between the probes N and 5 of the outer and inner probe array (Fig. 4.4). The poloidal displacement between the magnetic displacement and the experimental finding from parallel correlation measurements is thus $d_\perp \approx 1\,\mathrm{cm}$. The error in estimating the absolute probe positions with respect to the magnetic field is less than 1 cm.[1] Including this systematic error, we get $d_\perp = 1 \pm 1\,\mathrm{cm}$.

The average poloidal wave number $\overline{k}_\theta$ is estimated by means of the lock-in technique (Sec. 2.2.5). Only frequencies greater or equal 10 kHz are considered for the averaging. The values for the average poloidal wave number from four discharges with identical magnetic configuration and the same radial positions of the reciprocating array are shown in Tab. 4.1. The average poloidal wave number observed for discharge #50196 is negative compared to the other discharges. Nonetheless, all four discharges show the same parallel connections as discussed in the previous subsection (Fig. 4.4). It was previously observed, that a velocity shear layer exists near the last closed flux surface for certain discharge conditions [Bleuel 1998, Sec. III.2.1], which is characterized by a reversal of the poloidal velocity of the fluctuations. It might be the case that the radial position of the reciprocating array during discharge #50196 differs slightly from the other three discharges. Since the measurements are performed near the velocity shear region, a radial displacement of a few mm can give significantly different perpendicular wave numbers. We exclude the value for the perpendicular wave number obtained from discharge #50196 and get the mean and standard deviation from the remaining values in Tab. 4.1: $\overline{k}_\theta = (59.1 \pm 5.4)\,\mathrm{m}^{-1}$.

Discharge	$\overline{k}_\theta$ / m^{-1}
50196	-16.5
50232	51.7
50233	64.5
50234	61.2

Table 4.1.: *Average poloidal wave numbers for four quasi-identical discharges.*

Inserting the figures for the average perpendicular wave number $\overline{k}_\theta$, the perpendicular displacement $d_\perp$ and the connection length $L_c = 12\,\mathrm{m}$ into Eq. (2.22), we get the average parallel wave number $\overline{k}_\parallel \approx (0.05 \pm 0.05)\,\mathrm{m}^{-1}$. The upper limit for the ratio between the average wave numbers parallel and perpendicular to the magnetic field is $\overline{k}_\parallel / \overline{k}_\theta < 2 \cdot 10^{-2}$. This result for the average parallel wavenumber is in good agreement with previous measurements on W7-AS: Bleuel [1998]

[1] Only the poloidal displacement is taken into account, since the outer probe head performs a radial scan during the reciprocation.

estimated an average parallel wave number of $k_{||} = 0 \pm 0.03\,\mathrm{m}^{-1}$ for a connection length of 32 m. The obtained values for the parallel wave number on W7-AS and for the 23 m connection length on JET tokamak (Sec. 3.3.5) are all in agreement with $k_{||} = 0$ within the error bars.

4.4. Single point coupling

4.4.1. Set-up and basic features

For the experiments subsequently described, only a single probe tip of the outer array was driven by an external signal. A sine signal with a frequency of 60 kHz and a peak-to-peak voltage of 80 V was applied. The other tips were measuring floating potential. The voltage amplitude of the external signal is approximately 3–4 times the amplitude of the floating potential fluctuations.

Time series and the corresponding power spectra of fluctuations recorded by probe tips in the vicinity of the active probe are plotted in Fig 4.6. The time series show no evidence for any influence of the active signal. The power spectral densities, however, reveal a peak at 60 kHz (the driver frequency). Also, the higher harmonic at 120 kHz is observed by the probe tip directly below the active probe. The turbulent underground of the spectrum does not show any deviations compared to the auto-power spectrum of the floating potential signal without driver signal, cf. Fig. 4.7. The frequency region we focus our interest is very narrow and centered around the driver frequency.[2] Inspecting the heights of the peaks in the different spectra there is an apparent asymmetry: The spectra from tips below the active tip show the peak over a much larger poloidal extend than the spectra from the tips above.

Further analysis concentrates on the 60 kHz region. The coherency lock-in technique (Sec. 2.2.5) is a particularly valuable tool for the analysis of these data.

4.4.2. Advanced analysis: active and passive probes

From passive measurements many characteristics of the turbulence can already be derived, like scale length and drifts. These are briefly described for a comparative analysis. The signal of one of the outer array probes at the poloidal position defined as 0 cm is taken as reference for the coherency analysis. The coherency is calculated between the signals from all other probes and the signal from the reference probe. Fig. 4.8(a) shows the resulting coherency and phase for the 60 kHz frequency component, plotted versus the poloidal probe separation. From this

[2]Non-linear coupling to modes at other frequencies is not observed. This is also shown by bi-coherency analysis.

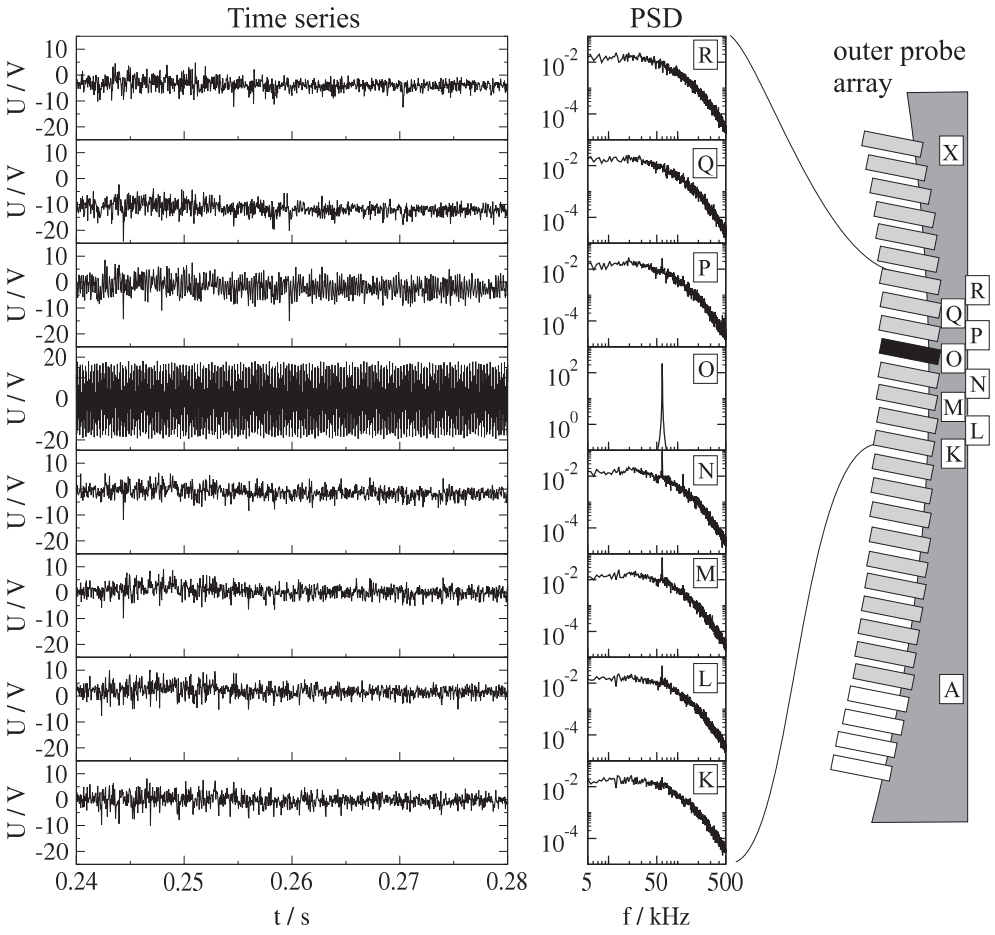

Figure 4.6.: *Raw signals and corresponding power spectral densities for the external 60 kHz signal (black tip, [O]) and the floating potential signals (grey tips) on the 28 pin outer probe head. Data from W7-AS discharge #50212.*

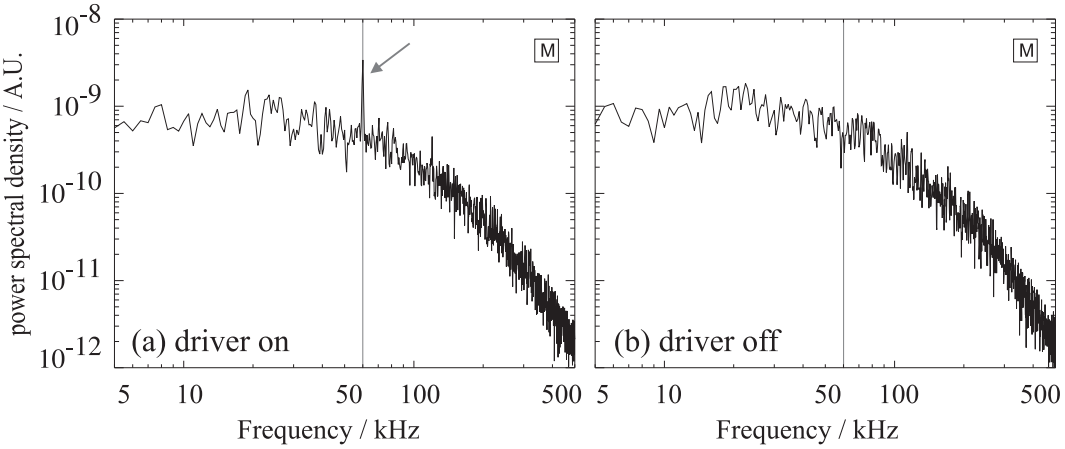

Figure 4.7.: *Power density spectrum of the floating potential signal detected by the outer array probe tip* $\boxed{M}$*. (a) With 60 kHz driver signal and (b) without driver signal on probe tip* $\boxed{O}$ *of the outer array. Data from W7-AS discharges #50212 and #50197.*

plot a poloidal scale length of approximately 1.4 cm (full width at 50% coherency) for the 60 kHz frequency component is estimated. In the vicinity of the reference probe, the slope of the phase curve indicates a poloidal drift with a phase velocity $v_p \approx 4000\,\mathrm{ms}^{-1}$, corresponding to a local wave number $k_\theta = 200\,\mathrm{m}^{-1}$. This drift is in the direction of the ion-diamagnetic drift (compare Fig. 1.6) and the poloidal $\mathbf{E} \times \mathbf{B}$-rotation of the plasma, the latter due to the radial electric field in the scrape-off layer.

Fig. 4.8(b) shows the result of the same analysis as above for the case that a 60 kHz sine signal with a peak-to-peak voltage of 80 V is applied to the reference probe tip. This leads to a significant modification of the poloidal signal propagation: Firstly, an asymmetry of the level of coherency with respect to the reference tip is observed, namely in the direction of the $\mathbf{E} \times \mathbf{B}$-rotation. Secondly, the poloidal scale length is slightly broadened to approximately 1.8 cm (full width at 50% coherency). Finally, the local wave number is increased to $k_\theta \approx 200\,\mathrm{m}^{-1}$. At the other frequency components, no significant changes are observed. For a similar set-up on TEXT (toroidal probe separation 12 m and driver frequency 30 kHz), a similar asymmetry and a smaller phase velocity were reported [Richards et al. 1994], in agreement with our results.

4.4.3. Single active probe on the inner probe array

One particularly interesting result of the active probing experiments on TEXT is the observed signal propagation asymmetry parallel to the magnetic field. The set-up described above with a single active probe on the outer array yields no clear

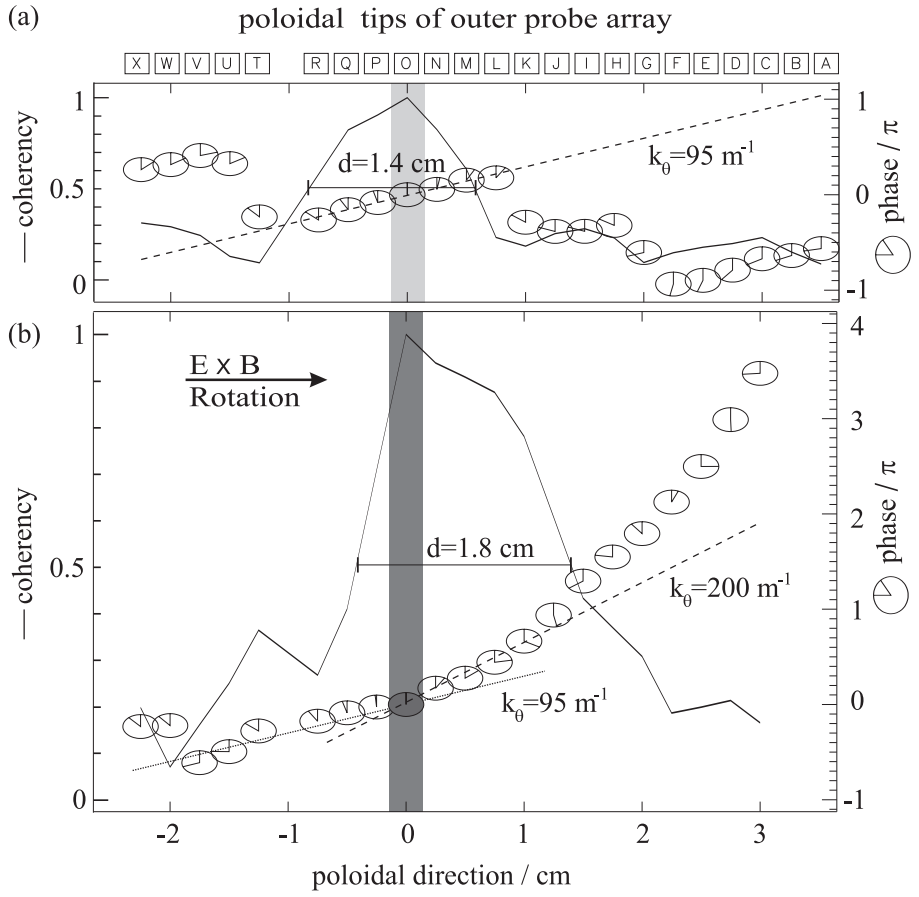

Figure 4.8.: *The coherency (solid lines) and phase (clocks) at the frequency of 60 kHz versus the poloidal position given by the probe tips (*$\boxed{A}$ *–* $\boxed{X}$*) of the outer array. The grey bar indicates the probe tip taken as reference for the coherency analysis (poloidal position 0 cm). (a) No external signal. The dashed line is a fit to the slope of the phase indicating a poloidal wave number* $k_\theta \approx 95\,\mathrm{m}^{-1}$*. (b) The reference probe is driven with a sine signal of 60 kHz. The phase is generally restricted to a range* $[-\pi, \pi]$*. Here, the phase is plotted without this constraint by adding* 2π *at points of discontinuity to guide the eye. The dashed line is a fit to the slope of the phase indicating the poloidal wave number* $k_\theta \approx 200\,\mathrm{m}^{-1}$*. The dotted line shows the poloidal wave number from (a). Data from W7-AS discharges #50197 and #50212.*

trace at the probes of the inner array. This might be due to the comparatively large probe distance on the inner array of 2 cm. The signals propagating from the active probe of the outer probe array to the inner array might not come close to any of the probe tips. The situation is improved for another set-up with a single active probe on the inner array. The probe tips on the inner array are larger, which allows one to draw higher currents leading to a higher signal amplitude. Furthermore, the outer probe array provides a good poloidal resolution of 0.25 cm tip distance.

A sinusoidal signal with a peak-to-peak amplitude of 80 V and a frequency of 60 kHz was applied to tip 6 of the inner array. The plasma response was detected at the toroidal distant outer probe array by means of the lock-in technique introduced above, compare Fig. 4.9. A maximum coherency of $C_{max} \approx 50\%$ is found between the reference probe tip 6 and probe tip P of the outer array. The poloidal region of high coherency is fairly broad and the phase is steadily increasing. A linear best fit yields the local wave number $k_\theta \approx 220\,\mathrm{m}^{-1}$.

The conjecture that the observed coherency and phase patterns are indeed caused by the active drive on the inner array is supported by the following findings. A discharge with identical plasma parameters but different rotational transform $\iota = 0.39$ (instead of $\iota = 0.40$) was investigated. The active signal ($f = 60\,\mathrm{kHz}$ and $U_{ss} = 80\,\mathrm{V}$) was again supplied to the inner array probe tip 6. The coherency and phase pattern observed for the same radial position for $\iota = 0.39$ [Fig. 4.9(b)] qualitatively remains the same if compared to the plot for $\iota = 0.40$ [Fig. 4.9(a)]. It is important to note, however, that the maximum coherency is found at a different probe tip I of the outer array. This systematic displacement of about 1 cm of the maximum corresponds very well to the change expected from the field line tracing for a change of rotational transform from $\iota = 0.39$ to $\iota = 0.40$.

The plasma response to a locally injected driver signal is clearly not locally restricted but is also observed far away parallel to the magnetic field. However, the coherency as well as the power spectral density of the injection signal is significantly reduced by the turbulent background fluctuations. Similar findings were reported for experiments on TEXT tokamak [Richards et al. 1994].

A finite propagation speed of the driver signal parallel to the magnetic field is expected for the actively coupled signals. This velocity can be estimated from the phase difference between the applied and the signal detected with the outer probe array. The phase difference at the maximum coherency is for both discharges $\Delta\varphi_{max} \approx 0.5\,\pi$. It should be kept in mind, however, that the propagation speed derived from the phase difference is not unique, since the injected signal is periodic. It is thus possible that the actual phase difference is larger by integer multiples of 2π. Hence, only the upper value for the signal propagation speed can be estimated. The maximum parallel phase velocity of the signal is given by

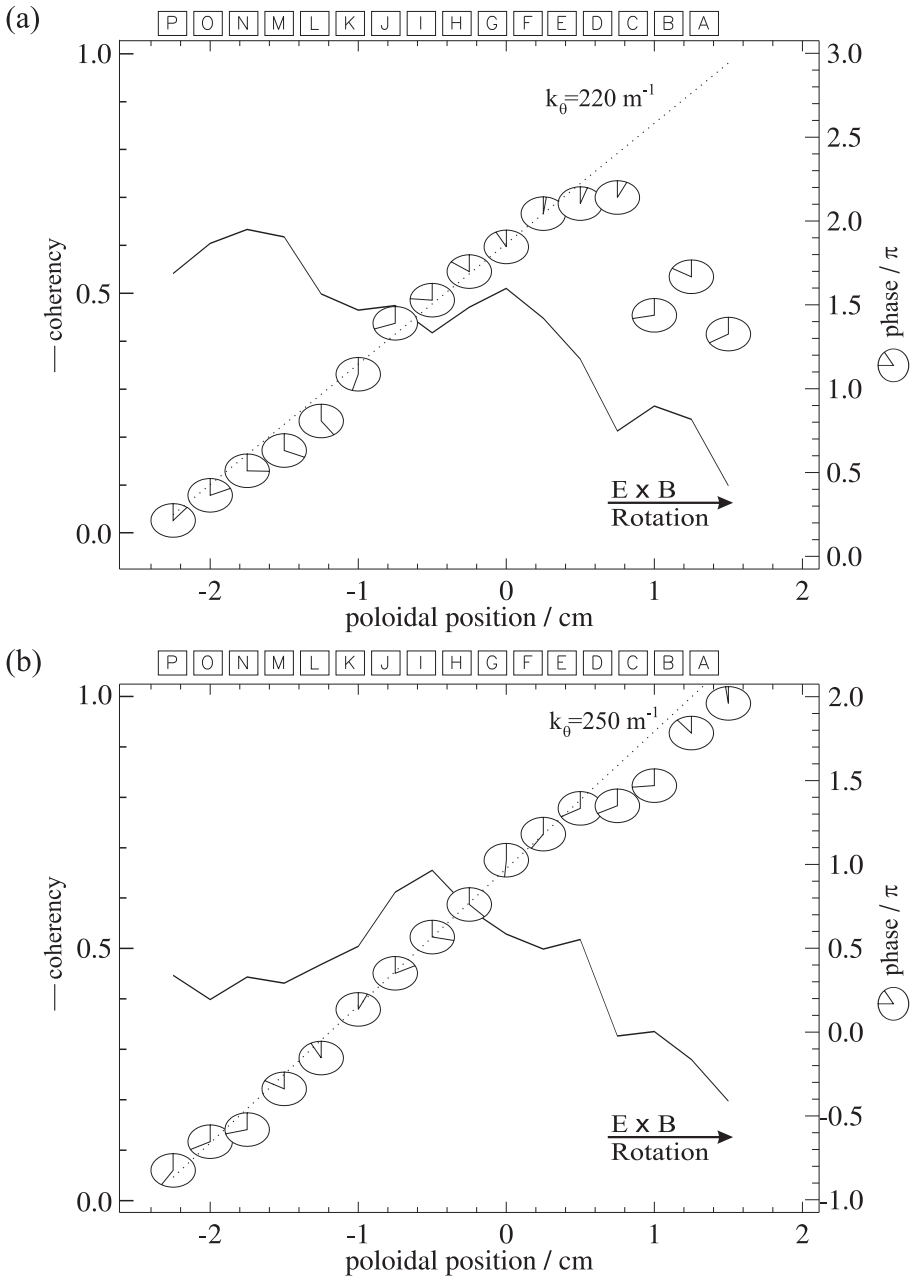

Figure 4.9.: *The coherency (solid lines) and phase (clocks) at the frequency of 60 kHz versus the poloidal position given by the probe tips of the outer array. The reference for the lock-in analysis is the 60 kHz signal applied to tip number* $\boxed{6}$ *of the inner array. (a) Rotational transform* $\iota = 0.40$*. The highest coherency is observed at tips* $\boxed{N}$ *and* $\boxed{M}$ *of the outer array. (b) Rotational transform* $\iota = 0.39$*. The highest coherency is observed at the* $\boxed{I}$ *tip of the outer array. Data from W7-AS discharges #50237 and #50239.*

the equation

$$v_{||\,max} = \frac{\omega L_c}{\Delta\varphi_{max}}\,. \tag{4.1}$$

The connection length is $L_c = 12\,\mathrm{m}$ for both discharges. Inserting the figures in Eq. (4.1) we obtain a maximum phase velocity of $v_{||\,max} \approx 2.9 \cdot 10^6\,\mathrm{ms}^{-1}$. This is one order of magnitude lower than the Alfvén velocity $v_A \approx 2 \cdot 10^7\,\mathrm{ms}^{-1}$ for the given discharge conditions[3]. The electron thermal velocity $\overline{c}_e = 3 \cdot 10^6\,\mathrm{ms}^{-1}$ (for an electron temperature $T_e = 20\,\mathrm{eV}$) is in a good agreement with $v_{||\,max}$.

4.5. Wave coupling

4.5.1. Set-up and observations in poloidal direction

Six phase-shifted sine signals were applied to a subset of six pairs of probe tips. The phase shift between two poloidally neighboring probe-pairs was set to $\Delta\varphi = 60° = \pi/3$. Between each active probe pair, one probe was operated to measure floating potential. In total, the six probe-pairs cover one complete (interpolated) sine-cycle [Fig. 4.10(a)]. With such a set-up, it is possible to impose a poloidally propagating spatio-temporal pattern – a sine-wave –on the turbulent plasma background. With respect to the $\mathbf{E} \times \mathbf{B}$-rotation, a co- and a counter-propagation of the sine-wave can be chosen by sign reversal of the phase shift [Fig. 4.10 (b) and (c)]. The driver frequency f_0 can be selected in a range of 1 – 100 kHz. In Fig. 4.10 the driver frequency is $f_0 = 30\,\mathrm{kHz}$ and in Fig. 4.11 $f_0 = 60\,\mathrm{kHz}$. The driver wave number k_θ^* is determined by distance $\Delta d = 0.75\,\mathrm{cm}$ and phase $\Delta\varphi = \pi/3$ between two successive active probe pairs, $k_\theta^* = \Delta\varphi/\Delta d \approx 140\,\mathrm{m}^{-1}$. For comparison: The mean poloidal wave number of the background turbulence was determined to be $\overline{k}_\theta = (59.1 \pm 5.4)\,\mathrm{m}^{-1}$. Due to the limited base length of the outer probe array a better match of the driver wave number to the dynamics of turbulent structures is not possible.

The coherency between the signals from the intermediate passive probe tips and the applied signals is near 100 % for co- and counter-propagation. In the case of co-propagating wave-patterns [Figs. 4.10(b) and 4.11(a)] the phases of active and passive signals are almost perfectly aligned over the whole range of poloidal probe tips of the outer array. This indicates a good coupling of the turbulent plasma background with the applied wave patterns.

The situation is different for the counter-propagating case [Figs. 4.10(c) and 4.11(c)], where the phases at the passive tips enclosed by the active probe-pairs (tips S P M J G) are not locked to the applied signals very well (so-called

[3] W7-AS plasma parameters: deuterium plasma with magnetic field $B = 2.5$ T, density $n = 5 \cdot 10^{18}\,\mathrm{m}^{-3}$ and temperature $T_e = 20\,\mathrm{eV}$

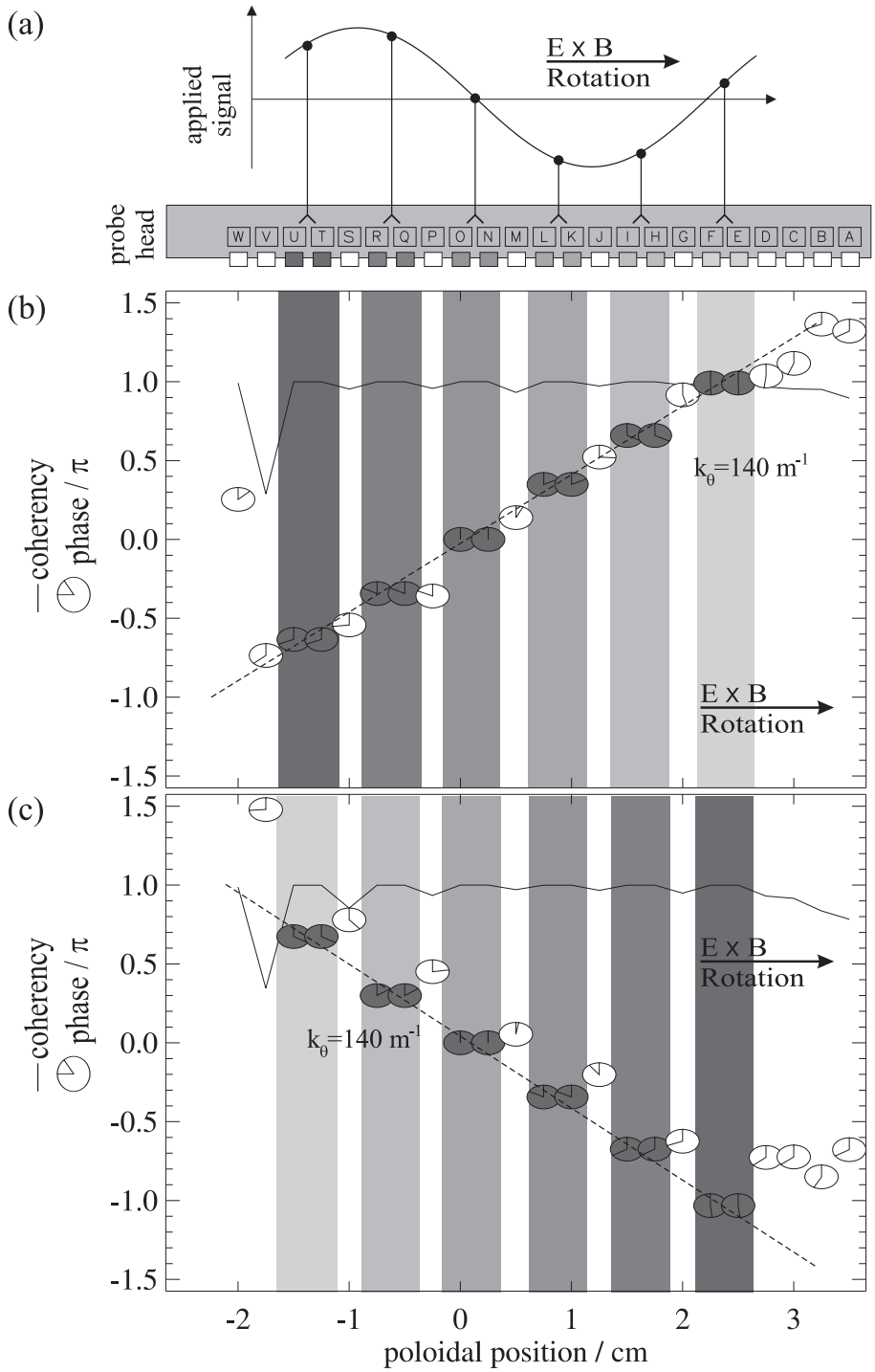

Figure 4.10.: *(a): To each of the 6 pairs of the active probe tips (marked in grey as opposed to the (passive) floating potential tips in white) sine signals with a phase shift of* $60° = \pi/3$ *rad and a frequency of 30 kHz are supplied. (b) Co-rotating sine wave. From the plot of the phase versus poloidal position, the direction of the wave (to the right, co-rotating with* $\mathbf{E} \times \mathbf{B}$*-rotation) and the imposed wave number* $k_\theta^* = 140\,\mathrm{m}^{-1}$ *can be estimated. Coherency and phase values are relative to the probe-pair at poloidal position 0 cm. (c): Counter-rotating sine wave (with respect to the* $\mathbf{E} \times \mathbf{B}$*-rotation). Data from W7-AS discharges #50297 and #50299.*

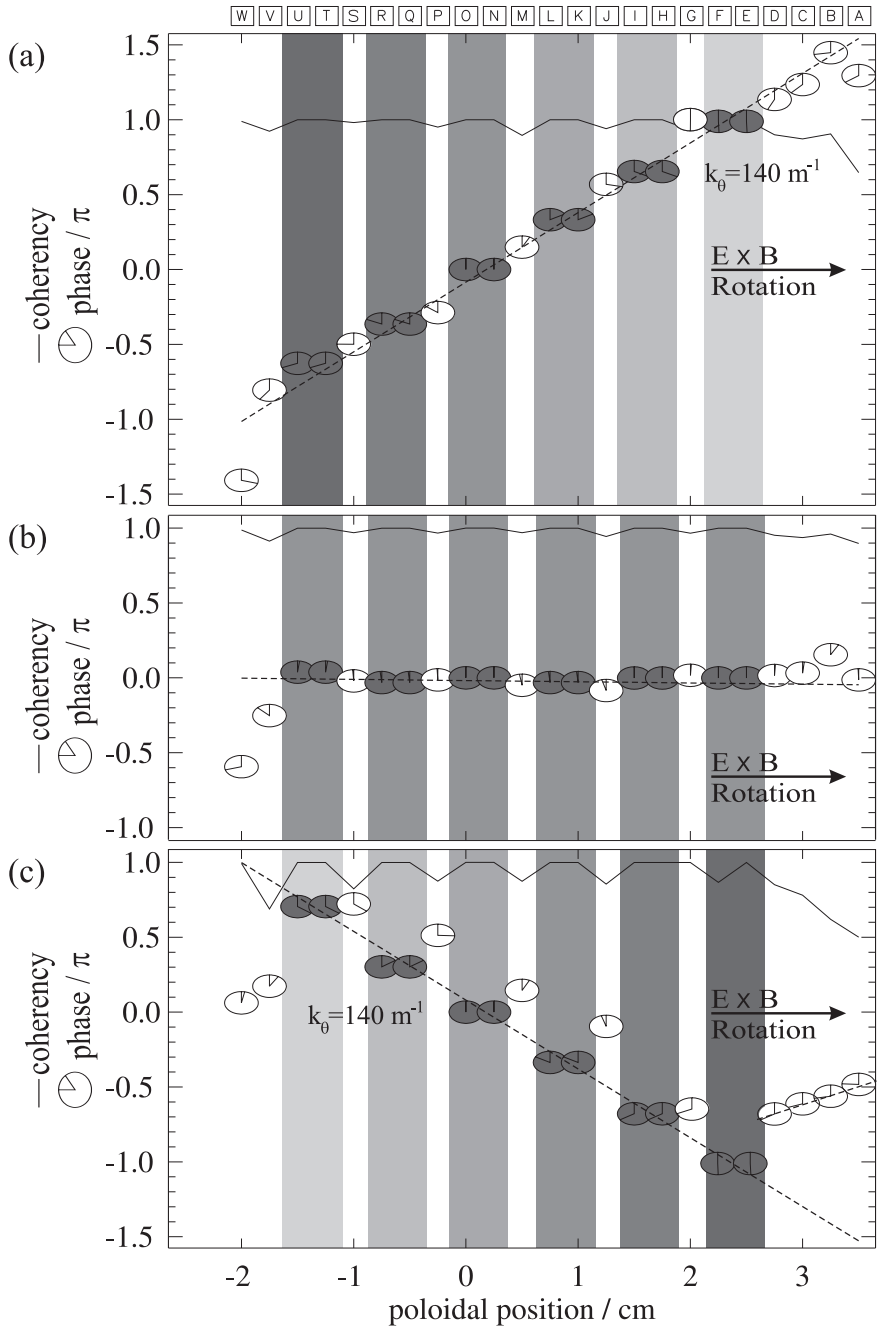

Figure 4.11.: *Same plots as in Fig. 4.10, but for 60 kHz driver frequency. Coherencies and phase values are relative to the probe-pair at poloidal position 0 cm. (a) Co-rotating sine wave (with respect to the* $\mathbf{E} \times \mathbf{B}$*-rotation). (b) Zero phase-shift between the applied signals. (c) Counter-rotating sine wave. Data from W7-AS discharges #50295, #50308 and #50296.*

phase slippage).[4] Moreover, outside the active probing region (probe tips D to A), the direction of the phase velocity changes to that of the background $\mathbf{E} \times \mathbf{B}$-rotation right away. For the case of $\Delta\varphi = 0$ [Fig. 4.11(b)] the phase slippage is not observed. From these findings it is reasonable to conclude, that there is a better coupling between the turbulent background plasma and the co-propagating wave pattern than with a counter-propagating wave pattern. Basically, this is in agreement with the observations on the MIRABELLE device, where a strong suppression of low-frequency drift modes was found for co-rotating external signals, whereas a counter-rotating signals did not influence the turbulent plasma dynamics [Schröder et al. 2001].

4.5.2. Observations in parallel direction: Active probes driven by a purely temporal signal

The active probe set-up with sine signals applied to six probe-pairs of the outer array without phase shift [Fig. 4.11(b)] is discussed here in some more detail. The driver signals are also detected on the inner probe array (connection length 12 m), as shown in Fig. 4.12. High coherencies between the input signal and the floating potential signals measured by the probes of the inner array are found at tips 3 4 5 6. The maximum coherency of approximately 70% is observed at probe 4. These basic findings are in a good agreement with the results from the (passive) parallel correlation measurements (Sec. 4.3).

As previously observed, the signal influence on the background plasma turbulence is limited to the driver frequency. Even though the phase between the driver signals is zero, a small change in phase is found for the probes 4 5 6 of the inner array, which – according to the field line tracing – have a magnetic connection to the driver probes [cf. Fig. 4.12]. This could be the effect of a (poloidal) misalignment of the inner probe array with respect to the flux tubes, which magnetically connect these probes with the driver probes of the outer array: If we consider a poloidal wave number of the signal in the order of $k_\theta \approx 200\,\mathrm{m}^{-1}$ as would be expected from the results discussed in Sec. 4.4.3, a poloidal displacement of $d = 0.5\,\mathrm{cm}$ would lead to a systematic phase-shift of $\Delta\varphi = k_\theta\, d \approx 0.3\,\pi$.

We note here, that the signal propagation parallel to the magnetic field do not show an asymmetry as reported for experiments on TEXT and KT-5C (cf. Sec. 4.1), since we find the signals injected at the inner probe array on probe tips of the outer array and vice versa for the injection of signals at the outer probe array. For both set-ups, the parallel signal propagation is in a good agreement

[4] Phase slippage was also observed in spatio-temporal synchronization experiments on the linear KIWI device for a counter-injection of wave signals [Block et al. 2001]. It was suggested, that this phenomenon is due to a spatio-temporal periodic pulling.

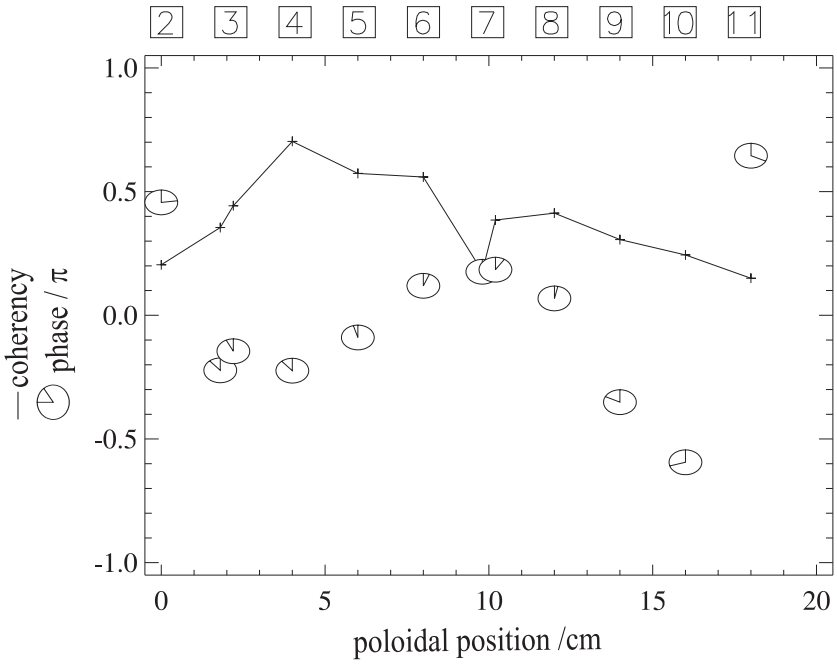

Figure 4.12.: *Cross-coherency (solid line) and phase (clocks) between the driver signal (sine, 60 kHz) on the outer array as reference and the signals from the probe tips of the inner array. Data from W7-AS discharge #50308.*

with the field line tracing calculations.

4.5.3. Parallel propagation of wave signals

The sine-waves which are imposed on the turbulent plasma background by the six probe-pairs of the outer array, can be detected over a distance of 12 m by the probe tips of the inner array. In Fig. 4.13 the coherency and phase between one driver signal and the floating potential measured by the tips 2 to 11 of the inner probe array for three different driver frequencies (30, 45 and 60 kHz) are plotted. The imposed waves are co-propagating with respect to the $\mathbf{E} \times \mathbf{B}$-rotation of the plasma in Fig. 4.13(a-c). The highest coherencies are observed on probe tip 2 for all three driver frequencies. Although the discharge conditions were the same for all the discharges presented in this chapter, the maximum coherency seems to be systematically shifted by approximately 2 cm in the direction of the $\mathbf{E} \times \mathbf{B}$-rotation, when compared to the set-up with a purely temporal coupling ($\Delta\varphi = 0$, cf. Fig. 4.12). For technical reason, the probe tips 0 and 1 were not available for the experiments, so that no more data is at hand to support this suspicion. For all three driver frequencies, the slopes of the phases of the probes 2 3 4 represent the imposed wave number $k_\theta^* = 140\,\mathrm{m}^{-1}$ reasonably well. The

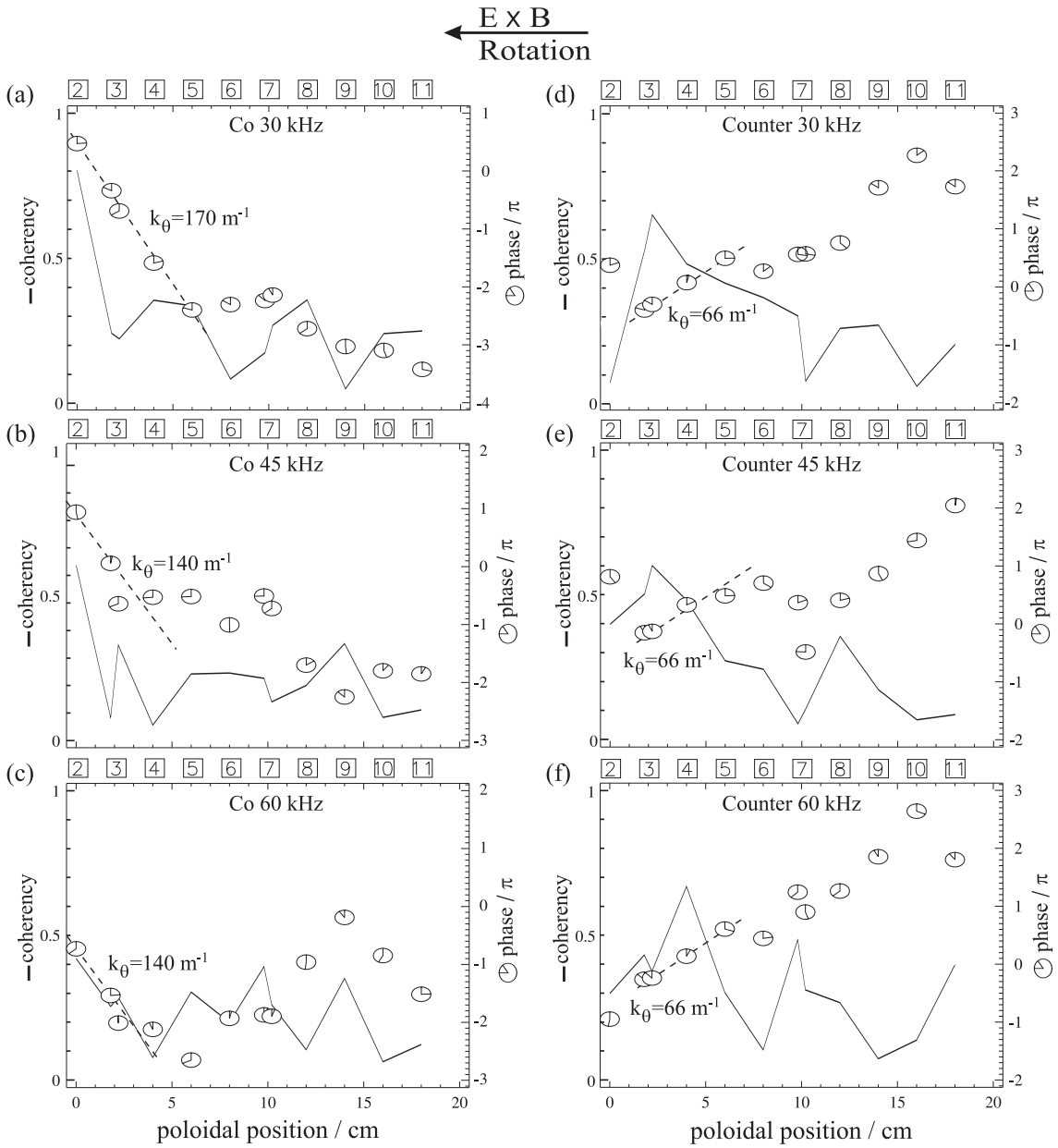

Figure 4.13.: *Cross-coherency (solid line) and phase (clocks) between one driver signal on the outer array as reference and the signals from the probes of the inner array (2 to 11). (a) 30 kHz, (b) 45 kHz and (c) 60 kHz co-propagation and (d) 30 kHz, (e) 45 kHz and (f) 60 kHz counter-propagation of the imposed sine waves. The dashed lines denote fits to the phases in regions of high coherency. Data from W7-AS discharges #50297, #50296, #50306, #50299, #50305, #50310.*

maximum coherency decreases linearly from 30 kHz to 60 kHz.

The results for counter-propagating imposed waves for three driver frequencies are shown in Fig. 4.13(d-f). The maximum coherency is found on probe 3 for driver frequencies of 30 and 45 kHz, and on probe 4 for a driver frequency of 60 kHz. This is in good agreement with the region of high coherency for the purely temporal coupling (Fig. 4.12). The poloidal wave number $k_\theta = 66\,\mathrm{m}^{-1}$, as obtained from the slopes of the phases when considering probes 3 4 5, is not compatible with the imposed poloidal wave number $k_\theta^* = 140\,\mathrm{m}^{-1}$. This observation supports the previously established finding, that the coupling strength of counter-propagating waves is less than that of co-propagating waves.

4.6. Discussion

In experiments on W7-AS, sinusoidal signals injected into the background plasma turbulence are observed to propagate parallel and perpendicular to the magnetic field. The signals are detected in parallel direction on the same probes of the distant array as expected from the parallel correlation measurements of background turbulence. An exception is found for the application of wave signals, which co-propagate with respect to the $\mathbf{E} \times \mathbf{B}$-rotation of the plasma (see below). An asymmetry of signal propagation (cf. Sec. 4.1) as reported for similar experiments on TEXT and KT-5C – both tokamaks – are not observed in W7-AS: A sine signal in the drift-frequency range below 100 kHz injected at the outer probe array was observed on the inner probe array and vice versa for a signal injection at the inner probe array. A possible explanation for the observed propagation asymmetry in experiments on the tokamaks could be an intersection of the connecting flux tube for one of the two set-ups.

On W7-AS, the parallel signal propagation speed $v_{||} \approx 2.9 \cdot 10^6\,\mathrm{ms}^{-1}$ is found to be of the order of the electron thermal velocity. As a matter of fact, such a velocity is expected for drift waves. On KT-5C a phase velocity of $v_{||} \approx 5 \cdot 10^5\,\mathrm{ms}^{-1}$ was reported, which is much slower than the Alfvén velocity $v_A \approx 3 \cdot 10^6\,\mathrm{ms}^{-1}$ and the electron thermal velocity $\overline{c}_e \approx 2 \cdot 10^6\,\mathrm{ms}^{-1}$ for the respective discharge conditions, but faster than the ion sound velocity $c_s \approx 4 \cdot 10^4\,\mathrm{ms}^{-1}$ [Kan et al. 1997]. It was proposed, that the signal propagation velocity could be determined by the velocity $v_{Iplas} = 5.5 \cdot 10^5\,\mathrm{ms}^{-1}$ of the electrons carried by the induced toroidal plasma current. We note here, that a poloidal misalignment of the two toroidally distant probe tips can result in an over-estimation of the phase difference between driver signal and detected signal (Sec. 4.5.2). Especially for probe arrays with a small base length (like in the experiments on the KT-5C tokamak) or a large probe tip separation (like for the inner array on the W7-AS stellarator) this can result in an estimate of the parallel propagation velocity, which is systematically

too small.[5]

In previous experiments on Wendelstein 7-AS, where short current pulses with a bandwidth of 5 MHz were applied to the plasma edge, a propagation parallel to the magnetic field of these disturbances with Alfvén velocity was found [Geier 1997; Geier and Niedermeyer 1998]. For the signal injection experiments with frequencies below 100 kHz, the signal propagation speed is significantly below the Alfvén velocity. However, similar experiments in the TEXT tokamak yield a signal propagation speed compatible with the Alfvén velocity [Uckan et al. 1995; Winslow et al. 1998]. A parametric study of the plasma parameters during signal injection experiments, i.e. the magnetic field, plasma density and temperature, would be helpful to clarify this issue.

Experiments in the linear low-temperature device MIRABELLE showed the possibility of a mode-selective stabilization of drift wave turbulence by means of an open-loop synchronization [Schröder et al. 2001]. In these proof-of-principle experiments, the synchronization of the plasma turbulence to the imposed waves was strongly dependent on the matching of applied the spatio-temporal wave pattern to the dynamics of the turbulent structures. In the experiments on the W7-AS – the first such experiments in a magnetized hot plasma – the overall influence of the signals on the plasma turbulence is found to be limited to a narrow frequency region around the driver frequency. Although a synchronization of the turbulence to the external wave pattern was not possible in these experiments, a difference of a co- and counter-propagation of the signal patterns with respect to the $\mathbf{E} \times \mathbf{B}$-rotation of the background plasma turbulence is observed. The coupling strength of the imposed waves to the turbulent plasma background seems to be improved for the co-propagation.

For a co-propagation of the imposed waves with the $\mathbf{E} \times \mathbf{B}$-rotation, the imposed wave number is observed parallel to the magnetic field over a distance of 12 m. As a matter of fact, the parallel propagation seems to be altered by a systematic shift of 2 cm in the direction of the $\mathbf{E} \times \mathbf{B}$-drift. Thus, the imposed wave pattern is not localized to the injection area, but has a non-local dynamic. For a counter-propagation of the imposed waves, phase-slippage is observed. At the distant probe neither the wave number of the imposed wave, nor a spatial shift is observed at the distant probe. All these findings are compatible with an improved coupling of the co-propagating waves with respect to counter-propagating waves.

The coupling strength of the imposed waves to the background plasma turbulence might be improved by an optimization of the spatially imposed structure, i.e. a better match of the imposed wave number to the dynamics of turbulent structures and a larger injection region. However, whether the stabilization of a single drift mode in a tokamak or stellarator plasma is achievable at all, remains

[5] In the present study, the parallel propagation speed was estimated for a set-up with the outer probe array used as distant detection array.

an open question. A major difference between turbulence in low- and high-temperature plasmas is the different scale of the turbulence, cf. Eq. (1.14). The turbulence scale is larger in low-temperature plasmas (like in the MIRABELLE device), and only a few exciter plates enclosing the whole plasma column are necessary for imposing waves with a good match with the wave numbers in the plasma. The coverage of an entire poloidal cross-section with exciter plates in a high-temperature plasma is presumably more effective in terms of coupling strength. Due to the smaller scale of the turbulence and the larger poloidal cross-section of the plasma, the installation of a suitable exciter set-up would be a major technical challenge. Moreover, such installation is not possible for a divertor configuration, since the exciter plates would act as a poloidal limiter and reduce the favorable properties of the divertor configuration. Further optimization of frequency and wave vector of the imposed waves is probably a promising approach for achieving a significant and systematic influence of turbulence.

5. Summary and Conclusions

The present experimental work investigates plasma turbulence in the edge region of magnetized high-temperature plasmas. A main topic is the turbulent dynamics parallel to the magnetic field, where hitherto only a small data basis existed, especially for very long scale lengths in the order of ten of meters. A second point of special interest is the coupling of the dynamics parallel and perpendicular to the magnetic field. This anisotropic turbulent dynamics is investigated by two different approaches. Firstly, spatially and temporally high-resolution measurements of fluctuating plasma parameters are investigated by means of two-point correlation analysis. Secondly, the propagation of signals externally imposed into the turbulent plasma background is studied. For both approaches, Langmuir probe arrays were utilized for diagnostic purposes.

Correlation measurements along the confining magnetic field over very long connection lengths of up to 66 m in the JET tokamak clearly indicate the existence of greatly elongated fluctuation structures. Within the error bars, these structures are perfectly aligned with the magnetic field and their wave number parallel to the magnetic field vanishes ($k_{\|} = 0$). Moreover, the correlation time lag is $\tau \approx 0$, which supports a filament-like fluctuation structure. Three different connection lengths were achieved for the parallel correlation study on the JET tokamak. The correlational degree for a short connection length of 0.75 m is greater than 80%. For much longer connection lengths of 23 m and 66 m, the correlation degree is reduced to approximately 40%. This reduction in correlation for long connection lengths cannot be appropriately treated in the framework of a two-dimensional model. A conceptual interpretation of these observations is the co-existence of two different fluctuation components. One component has a correlation length parallel to the magnetic field below 20 m and the other component a correlation length greater than 70 m.

The dynamics perpendicular to the magnetic field is already known to be dominated by the rotation of the entire plasma due to a stationary radial electric field. This could be studied particularly well in the Wendelstein 7-AS stellarator, by actively driven sine signals coupled to the turbulent background. The signals propagate parallel and perpendicular to the magnetic field and are phase-sensitively detected by means of a lock-in type technique. In poloidal direction an asymmetry of the signal propagation in direction of the background plasma drift is observed. A propagation asymmetry parallel to the magnetic field, as previ-

ously reported for similar experiments in tokamaks [Uckan et al. 1995; Kan et al. 1997], was not found in W7-AS. One might speculate, that in those experiments the connecting magnetic field line was intersected by some obstacle. In contrast to background turbulence, the parallel signal propagation time is non-zero seems to be in agreement with a propagation at electron thermal velocity.

As a more advance approach, spatio-temporal wave patterns were injected into the turbulent edge of the hot magnetized plasma. Such a technique was recently used in a magnetized low-temperature plasma and a strong influence on the plasma turbulence, i.e. a mode-selective synchronization, was found [Schröder et al. 2001]. On the contrary, in Wendelstein 7-AS stellarator the imposed waves do not show a dramatic effect on the plasma turbulence. The reason is probably the different (i.e. smaller) characteristic scale length of the turbulence in hot plasmas compared to the typical scale length of turbulence in low-temperature plasmas. Nonetheless, an interesting wave coupling phenomenon is observed: The coupling strength relies on the match of the imposed waves to the dynamics of turbulent structures. If the propagation direction of the imposed waves is parallel to the propagation direction of the background plasma, improved coupling is observed. This finding underlines the importance of the background plasma rotation for future attempts of controlling the plasma edge turbulence. Further optimization of frequency and wave vector of the imposed waves is probably a promising way for achieving a significant and systematic influence of turbulence.

Taking into account the present experimental state-of-the-art, for a deeper insight into the mechanism of the plasma edge turbulence of magnetized high-temperature plasmas a joint effort of numerical modeling and experimental results is a valuable approach. Such a cooperation should cover the explanation of the correlation observations as well as the experiments on signal injection into background turbulence. A quantitative comparison between the results presented in this work and a dedicated numerical drift wave simulation would be a significant step forward to a better understanding of plasma edge turbulence.

A. Appendix

A.1. Phase relation between fluctuations for maximum average particle transport

The fluctuations in potential, density and temperature have to be linked with each other for a non-zero net transport at time scales much longer than the fluctuation time scales. Let us consider a linear wave with frequency ω and wave number $\mathbf{k}$. The density fluctuations $\tilde{n}$ and the potential fluctuations $\tilde{\Phi}$ are assumed be phase-shifted by a constant angle α,

$$\tilde{n} = n_0 \exp[i(\mathbf{k}\cdot\mathbf{x} - \omega\, t)] \tag{A.1}$$

$$\tilde{\Phi} = \Phi_0 \exp[i(\mathbf{k}\cdot\mathbf{x} - \omega\, t + \alpha)]\,. \tag{A.2}$$

The dependence of α on the average particle flux can easily be calculated.

$$\begin{aligned}
\langle\tilde{\mathbf{\Gamma}}\rangle &= \langle\tilde{n}\,\tilde{\mathbf{v}}_E\rangle \\
&= \mathcal{R}e\left(\int_0^{T_0} \tilde{n}^*(t)\,\tilde{\mathbf{v}}(t)_E\,dt\right) \\
&= \mathcal{R}e\left(\int_0^{T_0} \tilde{n}^*(t)\,\frac{-(\nabla\tilde{\Phi}(t))\times\mathbf{B}}{B^2}\,dt\right) \\
&= \mathcal{R}e\left(\int_0^{T_0} \tilde{n}^*(t)\,\frac{-\tilde{\Phi}(t)\,i\mathbf{k}\times\mathbf{B}}{B^2}\,dt\right)
\end{aligned} \tag{A.3}$$

Only the real part $\mathcal{R}e()$ contributes to the average particle flux $\langle\tilde{\mathbf{\Gamma}}\rangle$. ΔT is the averaging time. The potential can be expressed in terms of the density,

$$\tilde{\Phi} = \frac{\Phi_0}{n_0}\tilde{n}\,\exp[i\alpha]\,. \tag{A.4}$$

Inserting Eq. (A.4) in Eq. (A.3) we obtain

$$\begin{aligned}
\langle\tilde{\mathbf{\Gamma}}\rangle &= \mathcal{R}e\left(\frac{-i\mathbf{k}\times\mathbf{B}}{B^2}\,\frac{\Phi_0}{n_0}\exp[i\alpha]\int_0^{T_0}\tilde{n}^*(t)\,\tilde{n}(t)\,dt\right) \\
&= \mathcal{R}e\left([\sin(\alpha) - i\cos(\alpha)]\,\frac{\mathbf{k}\times\mathbf{B}}{B^2}\,\frac{\Phi_0}{n_0}\int_0^{T_0} 1\,dt\right) \\
&= \sin(\alpha)\,\frac{\mathbf{k}\times\mathbf{B}}{B^2}\,\frac{\Phi_0}{n_0}\,T_0\,.
\end{aligned} \tag{A.5}$$

Hence, the average particle transport reaches a maximum for a phase-shift of $\pi/2$ between density and potential fluctuations. It should be noted here, that the phase applies for spatial as well as temporal phase-shifts. For a discussion of polychromatic fluctuations, cf. Ref. [Powers 1974].

A.2. Error analysis for the parallel wave number estimation for the 23 m connection length on JET tokamak

In figure 3.4 the field line tracing result for a 23 m connection between the outer divertor probe and the top reciprocating probe in the JET tokamak is plotted. The field line tracing code (ORBITB) has as a fixed stop condition, that the radial coordinate of the field line is equal to the reciprocating probe position R_{probe} within a certain box in toroidal and z-direction around the probe position. The actual poloidal displacement $d_\perp$ between the calculated field line and the top probe is estimated from the poloidal and toroidal component of the magnetic field at the probe position (B_{pol} and B_{tor}), the radial coordinate R_{probe} and the difference Δtor between the calculated end position (toroidal component) and the toroidal position of the reciprocating probe:

$$d_\perp = \Delta tor \cdot \frac{B_{pol}}{B_{tor}} \cdot R_{probe} = 1.87 \text{ cm}. \tag{A.6}$$

The error of $d_\perp$ can be estimated the following way: The relation between the poloidal displacement $d_\perp$ and the safety factor q_{95} is determined by the fit

$$d_\perp = a_{fit} \cdot q_{95} \,(+\text{arbitrary Offset}), \tag{A.7}$$

see figure 3.5. Hence, the total relative error of the poloidal displacement $r(d_\perp)$ is given by the sum of the relative errors of a_{fit} and q_{95},

$$r(d_\perp) = r(a_{fit}) + r(q_{95}). \tag{A.8}$$

- The linear regression of equation (A.7) yields $a_{fit} = 82$ cm and the associated absolute error $\sigma(a_{fit}) = 20$ cm. The relative error is $r(a_{fit}) = \sigma(a_{fit})/a_{fit} \approx 24\%$.
- The uncertainty of q_{95} is considered by the doubled standard deviation (95 % confidence interval) of the safety factor, $\sigma(q_{95}) = 0.028$. The change in safety factor is given by $\Delta q_{95} = d_\perp/a_{fit} = 0.023$. The relative error is $r(q_{95}) = \sigma(q_{95})/\Delta q_{95} \approx 121\%$.

Inserting these figures in equation (A.8) yields an estimate for the total error $r(d_\perp) = 135\%$, respectively $\Delta d_\perp = 2.8$ cm.

Bibliography

R. Balbin, C. Hidalgo, M.A. Pedrosa, I. Garcia-Cortes, and J. Vega. Measurement of density and temperature fluctuations using a fast-swept langmuir probe. *Rev. Sci. Instrum.*, 63(10):4605, 1992.

J. M. Beall, Y. C. Kim, and E. J. Powers. Estimation of wavenumber and frequency spectra using fixed probe pairs. *J. Appl. Physics*, 53(6):3933, 1982.

R. D. Bengtson, D. L. Winslow, and D. W. Ross. Fluctuation Measurements With two Separated Probe Arrays on the Same Flux Tube. *Contrib. Plasma Phys.*, 38:104, 1998. Special Issue.

E. Bertolini et al. Current Engineering Issues and Further Upgrading of the JET Tokamak. *JET-P*, 97(49), 1997.

P. Beyer, S. Benkadda, X. Garbet, and P.H. Diamond. Nondiffusive transport in tokamaks: Three-dimensional structure of bursts and the role of zonal flows. *Phys. Rev. Letters*, 85:4892, 2000.

R.J. Bickerton. Magnetic turbulence and the transport of energy and particles in tokamaks. *Plasma Phys. Controlled Fusion*, 39:339, 1997.

H. Biglari, P.H. Diamond, and P.W. Terry. Influence of sheared poloidal rotation on edge turbulence. *Phys. Fluids B*, 1:109, 1990.

D. Biskamp, P.H. Diamond, X. Garbet, Z. Lin, J. Nührenberg, and R.N. Rogers. Conference report: First principle based transport theory. *Nucl. Fusion*, 40: 873, 2000.

D. Biskamp and A. Zeiler. Nonlinear Instability Mechanism in 3D Collisional Drift-Wave Turbulence. *Phys. Rev. Letters*, 74(5):706–709, 1995.

J. Bleuel. *Elektrostatische Turbulenz am Plasmarand des Stellarators Wendelstein 7-AS*. PHD-thesis, Technische Universität München, 1998. IPP report III/235, Max-Planck-Institut für Plasmaphysik, Garching.

J. Bleuel, M. Endler, H. Niedermeyer, G. Theimer, and W7-AS Team. Structure of the edge fluctuations in the W7-AS stellarator. In M. Schittenhelm, R. Bartiromo, and F. Wagner, editors, *24th EPS Conference on Controlled*

Fusion and Plasma Physics (Berchtesgaden), volume 21A, page 1613. The European Physical Society, 1997.

J. Bleuel, G. Theimer, M. Endler, L. Giannone, H. Niedermeyer, ASDEX, and W7-AS Teams. The Edge Turbulence in the W7-AS Stellarator: 2d Characterisation by Probe Measurements. In D. Gresillon, A. Sitenko, and A. Zagorodny, editors, *23rd EPS Conference on Controlled Fusion and Plasma Physics (Kiev)*, volume 20C part II, page 727. The European Physical Society, 1996.

D. Block, A. Piel, Ch. Schröder, and T. Klinger. Synchronization of drift waves. *Phys. Rev. E*, 63:6401, 2001.

A. Boileau. Tokamak plasma biasing. *Nucl. Fusion*, 33:165, 1993.

A. H. Boozer. What is a stellarator? *Phys. Plasmas*, 5:1647, 1998.

N. Bretz. Diagnostic instrumentation for microturbulence in tokamaks. *Rev. Sci. Instrum.*, 68:2927, 1997.

K.H. Burrell. Effects of ExB velocity shear and magnetic shear on turbulence and transport in magnetic confinement devices. *Phys. Plasmas*, 4:1499, 1997.

A. W. Carlson. Two-point estimation of the spectral density function with finite separation and volume. *J. Appl. Physics*, 70:4033, 1991.

B.A. Carreras. Transport mechanisms acting in toroidal devices: a theoretician's view. *Plasma Phys. Controlled Fusion*, 34:1825, 1992.

C. Chatfield. *The analysis of time series.* Chapman and Hall, 5th edition, 1996.

F. F. Chen. Electric probes. In R. H. Huddlestone and S. L. Leonard, editors, *Plasma Diagnostic Techniques*, page 113. Academic Press, 1965.

F. F. Chen. *Plasma Physics and Controlled Fusion.* Plenum Press, 1984.

L. Chen and C.Z. Cheng. Drift-wave eigenmodes in toroidal plasmas. *Phys. Fluids*, 23:2242, 1980.

S. J. Davies, S. K. Erents, A. Loarte, H. Y. Guo, et al. The JET Reciprocating Probe Systems - Performance and Data Analysis. *Contrib. Plasma Phys.*, 36:117, 1996. Special Issue.

J. F. Drake, A. Zeiler, and D. Biskamp. Nonlinear Self-Sustained Drift-Wave Tubulence. *Phys. Rev. Let.*, 75:23, 1995.

M. Endler. *Experimentelle Untersuchung und Modellierung elektrostatischer Fluktuationen in den Abschälschichten des Tokamak ASDEX und des Stellarators Wendestein 7-AS.* PHD-thesis, Technische Universität München, 1994. IPP report III/197, Max-Planck-Institut für Plasmaphysik, Garching.

M. Endler. Turbulent SOL transport in stellarators and tokamaks. *J. Nucl. Mater.*, 266-269:84, 1999.

M. Endler, K. Giannone, H. McCormick, et al. Turbulence in the SOL of ASDEX and W7-AS. *Physica Scripta*, 51:610, 1995.

G. Fiksel, R.D. Bengtson, M. Cekic, D. Den Hartog, et al. Measurement of magnetic fluctuation-induced heat transport in tokamaks and RFP. *Plasma Phys. Controlled Fusion*, 38:a213, 1996.

N.J. Fisch. Theory of current drive in plasmas. *Rev. Mod. Phys.*, 59:175, 1987.

U. Frisch. *Turbulence: the legacy of A.N. Kolmogorov.* Cambridge University Press, 1995.

F. Gadelmeier, Y. Feng, P. Grigull, L. Giannonne, J. Kisslinger, et al. Conditions for island divertor operation in the W7-AS stellarator. In C. Silva, C. Varandas, and D. Campbell, editors, *28th EPS Conference on Controlled Fusion and Plasma Physics (Madeira)*, volume 25A, page 2085. The European Physical Society, 2001.

A. Geier. *Transientes Verhalten von Langmuirsonden in einem magnetisierten Plasma.* diploma-thesis, Technische Universität München, 1997. IPP report III/224, Max-Planck-Institut für Plasmaphysik, Garching.

A. Geier and H. Niedermeyer. Transient behaviour of langmuir probes in a magnetized plasma. *Contrib. Plasma Phys.*, 38:86, 1998. Special Issue.

L. Giannone, R. Balbin, H. Niedermeyer, M. Endler, G. Herre, C. Hidalgo, A. Rudij, G. Theimer, and Ph. Verplanke. Density, Temperature and potential fluctuation measurements by swept Langmuir probe technique in Wendelstein 7-AS. *Phys. Plasmas*, 1:3614, 1994.

R. J. Goldston and P. H. Rutherford. *Introduction to Plasma Physics.* IOP Publishing Ltd, 1995.

P. Grigull, K. McCormick, J. Baldzuhn, R. Burhenn, R. Brakel, et al. First island divertor experiments on the w7-as stellarator. *Plasma Phys. Control. Fusion*, 43:a175, 2001.

R.A. Gross. *Fusion Energy.* A Wiley-Interscience publication, 1984.

O. Grulke, T. Klinger, M. Endler, A. Piel, and the W7-AS Team. Analysis of large scale fluctuation structures in the scrape-off layer of the Wendelstein 7-AS stellarator. *Phys. Plasmas*, 8:5171, 2001.

P.N. Gudzar et al. Effect of magnetic shear on dissipative drift-wave instabilities. *Phys. Rev. Letters*, 40:1566, 1978.

A.A. Harms, K.F. Schoepf, G.H. Miley, and D.R. Kingdon. *Principles of Fusion Energy.* World Scientific Publishing, 2000.

A. Hasegawa and K. Mima. Stationary spectrum of strong turbulence in magnetized nonuniform plasma. *Phys. Rev. Letters*, 39:205, 1977.

C. Hidalgo. Edge turbulence and Anomalous Transport in Fusion Plasmas. *Plasma Phys. Control. Fusion*, 37:A53, 1995.

F.L. Hinton and R.D. Hazeltine. Theory of plasma transport in totoidal confinement systems. *Rev. Mod. Phys.*, 48:239, 1976.

S.P. Hirshman and K. Molvig. Turbulent destabilization and saturation of the universal drift mode in a sheared magnetic field. *Phys. Rev. Letters*, 42:648, 1979.

P. Horowitz and W. Hill. *The Art of Electronics.* Cambridge University Press, 2nd edition, 1990.

W. Horton. Drift waves and transport. *Rev. Mod. Phys.*, 71:735, 1999.

K. Itoh and S.-I. Itoh. The role of the electric field in confinement. *Plasma Phys. Controlled Fusion*, 38:1, 1996.

F. Jenko. *Numerische Modellierung von stoßfreier Driftwellenturbulenz.* Dissertation, MPI Garching, 1998.

F. Jenko and B.D. Scott. Effect of nonlinear electron landau damping in collisionless drift-wave turbulence. *Phys. Rev. Letters*, 80:4883, 1998.

F. Jenko and B.D. Scott. Numerical computation of collisionless drift wave turbulence. *Phys. Plasmas*, 6:2418, 1999.

B.B. Kadomtsev. *Tokamak plasma: A complex physical system.* IOP publishing, 1992.

Z. Kan, W. Yi-zhi, W. Shu-de, L. Wan-dong, Y. Chang-xuan, and X. Zhi-zhan. Modification of plasma edge fluctuationd using electrostatic probes in keda tokamak-5c. *Phys. Plasmas*, 4:2237, 1997.

M. Keilhacker, A. Gibson, C. Gormezano, P.J. Lomas, P.R. Thomas, et al. High fusion performance from deuterium-tritium plasmas in JET. *Nucl. Fusion*, 39:209, 1999.

A. Kendl. *Driftwellen in Helias-Konfigurationen.* Dissertation, TU München, 2000.

M. Kikuchi. Prospects of a stationary tokamak reactor. *Plasma Phys. Controlled Fusion*, 35:b39, 1993.

T. Klinger, Chr. Schröder, D. Block, F. Greiner, A. Piel, G. Bonhomme, and V. Naulin. Chaos control and taming of turbulence in plasma devices. *Phys. Plasmas*, 8:1961, 2001.

D. Lafrance, R. Huan, B.L. Stansfield, et al. Modification of the internal electric field by biasing of the divertor plates in the Tokamak de Varennes (TdeV). *Phys. Plasmas*, 4:3644, 1997.

P. C. Liewer. Measurements of Microturbulence in Tokamaks and Comparison with Theories of Turbulence and Anomalous Transport. *Nucl. Fusion*, 25: 543, 1985.

G. F. Matthews, S. J. Davies, and R. D. Monk. Technical Performance of Fixed Langmuir Probe Systems in the JET Pumped Divertor. *Contrib. Plasma Phys.*, 36:29, 1996. Special Issue.

G.F. Matthews. Tokamak plasma diagnostics by electrical probes. *Plasma Phys. Controlled Fusion*, 36:1595, 1994.

J.R Myra, D.A. D'Ippolito, X.Q. Xu, and R.H. Cohen. Resistive modes in the edge and scrape-off-layer of diverted tokamaks. *Phys. Plasmas*, 7:4622, 2000.

K. Nishikawa and M. Wakatani. *Plasma Physics.* Springer-Verlag, 3rd edition, 1999.

D. P. O'Brian, L. L. Lao, E. R. Solano, et al. Equilibrium analysis of iron core tokamaks using a full domain method. *Nucl. Fusion*, 32(8):1351, 1992.

H.L. Pécseli. *Fluctuations in Physical Systems.* Cambridge University Press, 2000.

M.R. Perrone and J.A. Wesson. Stability of axixymmetric modes in JET. *Nucl. Fusion*, 21:871, 1981.

U. Pfeiffer, M. Endler, J. Bleuel, H. Niedermeyer, G. Theimer, and W7-AS Team. Density, Temperature and Potential Fluctuation Measurements with Multiple Fast Swept Langmuir Probes on W7-AS. *Contrib. Plasma Phys.*, 38: 134, 1998. Special Issue.

K. Pinkau and U. Schumacher. Kernfusion mit magnetisch eingeschlossenen Plasmen. *Physik in unserer Zeit*, 13(5):138, 1982.

E.J. Powers. Spectral techniques for experimental investigation of plasma diffusion due to polychromatic fluctuations. *Nucl. Fusion*, 14:749, 1974.

W.H. Press, S.A. Teukolsky, W.T. Vetterling, and B.P. Fannery. *Numerical recipies in C.* Cambridge University Press, 2nd edition, 1992.

P.-H. Rebut, R. J. Bickerton, and B. E. Keen. . *Nucl. Fusion*, 25:1011, 1985.

C. Riccardi, C. Bevilacqua, G. Chiodini, and M. Fontanesi. Effect of edge biasing on electrostatic fluctuations and particle transport in a nonfusion magnetoplasma. *Phys. Plasmas*, 7:1459, 2000.

B. Richards, T. Uckan, A.J. Wootton, and B.A. Carreras others. Modification of tokamak edge turbulence using feedback. *Phys. Plasmas*, 1(5):1606, 1994.

Ch. P. Ritz, E.J. Powers, T. L. Rhodes, R. D. Bengtson, et al. Advanced plasma fluctuation analysis techniques and their impact on fusion research. *Review of Scientific Instruments*, 59(8):1739, 1988.

M.N. Rosenbluth and C.L. Longmire. Stability of plasmas confined by magnetic fields. *Annals of Physics*, 1:120, 1957.

D.W. Ross. On standard forms for transport equations and fluxes. *Plasma Phys. Controlled Fusion*, 12:155, 1989.

D.W. Ross and S.M. Mahajan. Are drift-eigenmodes unstable? *Phys. Rev. Letters*, 40:325, 1978.

A. Rudyj. *Untersuchung transportrelevanter Fluktuationen in der Randschicht von ASDEX.* PHD-thesis, Technische Universität München, 1990. IPP report III/160, Max-Planck-Institut für Plasmaphysik, Garching.

A. Rudyj, R. D. Bengtson, A. Carlson, L. Giannone, M. Krämer, H. Niedermeyer, Ch. P. Ritz, N. Tsois, and the ASDEX Team. Investigation of low-frequency fluctuations in the edge plasma of ASDEX. In S. Segre, H. Knoepfel, and E. Sindoni, editors, *16th EPS Conference on Controlled Fusion and Plasma Physics (Venice)*, volume 13B part I, page 27. The European Physical Society, 1989.

A. Rudyj, A. Carlson, M. Endler, L. Giannone, H. Niedermeyer, and G. Theimer. Structure of Density Fluctuations in the edge plasma of ASDEX. In G. Brifford, Adri Nijsen-Vis, and F. C. Schüller, editors, *17th EPS Conference on Controlled Fusion and Plasma Heating (Amsterdam)*, volume 14B part III, page 1464. The European Physical Society, 1990.

Chr. Schröder, T. Klinger, D. Block, A. Piel, G. Bonhomme, and V. Naulin. Mode selective control of drift wave turbulence. *Phys. Rev. Letters*, 86(25): 5711, 2001.

M. Schubert. PHD thesis: Fast-swept Langmuir probes on Wendelstein 7-AS, 2002.

B. Scott. Self-sustained collisional drift-wave turbulence in a sheared magnetic field. *Phys. Rev. Letters*, 65:3289, 1990.

B. Scott. The mechanism of self-sustainment in collisional drift wave turbulence. *Phys. Fluids B*, 4:2468, 1992.

B. Scott. Three-dimensional computation of collisional drift wave turbulence and transport in tokamak geometry. *Plasma Physics and Controlled Fusion*, 39 (3):471, 1997a.

B. Scott. Three-dimensional computation of drift Alfvén turbulence. *Plasma Phys. Control. Fusion*, 39:1635, 1997b.

B.D. Scott. ExB shear flow and electromagnetic gyrofluid turbulence. *Phys. Plasmas*, 7:1845, 2000.

B.D. Scott. *Low frequency fluid drift turbulence in magnetized plasmas.* Habilitation thesis, Heinrich Heine University Düsseldorf, 2001. IPP report 5/92.

A.K. Sen. Remote feedback stabilization of tokamak instabilities. *Phys. Plasmas*, 1:1479, 1994.

D.E. Smith and E.J. Powers. Experimental determination of the spectral index of a turbulent plasma from digitally computed power spectra. *Phys. Fluids*, 16:1373, 1973.

L. Spitzer. The stellarator concept. *IEEE transactions on plasma science*, PS-9: 130, 1981. Reprint from Phys. Fluids 1958, p. 253.

P.C. Stangeby. The plasma sheath. In Post and Behrish, editors, *Physics of plasma-wall interactions in controlled fusion*, number 131 in NATO ASI, page 41. Plenum press, N.Y., 1986.

P.C. Stangeby. *The Plasma boundary of magnetic fusion devices*. IOP publishing, 2000.

U. Stroth. A comparative study of transport in stellarators and tokamaks. *Plasma Physics and Controlled Fusion*, 40(1):9, 1998.

E. Teller, editor. *Fusion*, volume 1. Academic Press, Inc., London, 1981.

P.W. Terry. Suppression of turbulence and transport by shear flow. *Rev. Mod. Phys.*, 72:109, 2000.

G. Theimer. *Charakterisierung transportrelevanter turbulenter elektrostatischer Fluktuationen in der Abschälschicht des Tokamaks ASDEX mittels Darstellung als Superposition von raum-zeitlich lokalisierten Ereignissen*. PHD-thesis, Technische Universität München, 1997. IPP report III/223, Max-Planck-Institut für Plasmaphysik, Garching.

K.I. Thomassen. Feedback stabilization in plasmas. *Nucl. Fusion*, 11:175, 1971.

K.T. Tsang, J. C. Catto, P. J.and Whitson, and J. Smith. 'Absolute universal instability' is not universal. *Phys. Rev. Letters*, 40:327, 1978.

T. Uckan, B. Richards, R.D. Bengson, B.A. Carreras, et al. Active probing of plasma edge turbulence and feedback studies on the Texas experimental tokamak (TEXT). In J. A. Costa Cabral, M. E. Manso, F. M. Serra, and F. C. Schüller, editors, *20th EPS Conference on Controlled Fusion and Plasma Physics (Lisbon)*, volume 17C, part II, pages II–635. The European Physical Society, 1993.

T. Uckan, B. Richards, R.D. Bengson, B.A. Carreras, et al. Plasma edge turbulence probing and feedback control and stabilization experiments. *Nucl. Fusion*, 35(4):487, 1995.

F. Wagner. Collisional transport and neo-classical aspects in toroidal confinement. In K.H. Spatschek and J. Uhlenbusch, editors, *Contributions to high-temperature plasma physics*, chapter 2. Akademie Verlag, 1994.

F. Wagner and U. Stroth. Transport in toroidal devices – the experimentalists view. *Plasma Phys. Control. Fusion*, 35:1321, 1993.

M. Wakatani. *Stellarator and Heliotron Devices*, volume 95 of *International Series of Monographs on Physics*. Oxford Univ.Press, 1998.

M. Weinlich. *Elektrostatische Sonden in starken Magnetfeldern*. PHD-thesis, Technische Universität München, 1995. IPP report 5/64, Max-Planck-Institut für Plasmaphysik, Garching.

J. Wesson. *Tokamaks*. Oxford University Press, 2nd edition, 1997.

R.R. Weynants and G. van Oost. Edge biasing in tokamaks. *Plasma Phys. Controlled Fusion*, 35:b177, 1993.

R.R. Weynants, G. van Oost, G. Bertschinger, J. Boedo, et al. Confinement and profile changes induced by the presence of positive or negative radial electric fields in the edge of the TEXTOR tokamak. *Nucl. Fusion*, 32:837, 1992.

D. L. Winslow, R. D. Bengtson, B. Richards, and W. A. Craven. Determination of field line location and safety factor in TEXT-U. *Rev.Sci. Instrum.*, 68 (1):396, 1997.

D. L. Winslow, R. D. Bengtson, B. Richards, and A.J. Wootton. Propagation of a disturbance created by a probe in electron collection. *Phys. Plasmas*, 5 (3):752, 1998.

A.J. Wootton, B.A. Carreras, H. Matsumoto, K. McGuire, W. Peebles, Ch.P. Ritz, P.W. Terry, and S.J. Zweben. Fluctuations and anomalous transport in tokamaks. *Phys. Fluids B*, 2:2879, 1990.

X.Q. Xu, R. H. Cohen, G.D. Porter, et al. Turbulence studies in tokamak boundary plasma turbulence with realistic divertor geometry. *Nucl. Fusion*, 40 (3):731, 2000.

A. Zeiler. *Tokamak edge turbulence*. Habilitation thesis, University of Ulm, 1999. IPP report 5/88.

A. Zeiler, D. Biskamp, and J. F. Drake. Three-dimensional collisional drift-wave turbulence: Role of magnetic shear. *Phys. Plasmas*, 3(11):3947, 1996.

A. Zeiler, D. Biskamp, J. F. Drake, and B. N. Rogers. Transition from resistive ballooning to η_i driven turbulence in tokamaks. *Phys. Plasmas*, 5(7):2654, 1998.

A. Zeiler, J. F. Drake, and D. Biskamp. Electron temperature fluctuations in drift-resistive ballooning turbulence. *Phys. Plasmas*, 4(4):991, 1997.

S. Zoletnik, M. Anton, M. Endler, S. Fiedler, M. Hirsch, K. McCormick, J. Schweinzer, and the W7-AS Team. Density fluctuation phenomena in the scrape-off layer and edge plasma of Wendelstein 7-AS stellarator. *Phys. Plasmas*, 6(11):4239, 1999.

S.J. Zweben and R.W. Gould. Structure of edge-plasma turbulence in the Caltech tokamak. *Nucl. Fusion*, 25:171, 1985.

Acknowledgment

First of all I want to thank Prof. Dr. Thomas Klinger who established the contact to IPP and – together with Dr. Michael Endler and Prof. Dr. Friedrich Wagner – made the research project at JET as well as a PHD-position at IPP possible.

I thank Dr. Johannes Bleuel for the introduction into the work at the JET-site and to the Cotswolds. The international mixture of young and experienced scientists made up an inspiring atmosphere at JET – despite a lot of leaving parties in 1999. Many thanks to my colleagues at JET for their scientific feedback, especially to Dr. Alexi Chankin and Dr. Guy Matthews. The short-bread breaks after lunch have been very enjoyable. I acknowledge the discussions with Dr. Filippo Sartori, Dr. Vladimir Drozdov, Dr. Geraint Lloyd and Dr. Sergei Gerasimov about the vertical instability, magnetics and the EFIT code at JET. I don't want to forget my landlord Martin Saczak, who provided the very basics: His house was home during my stay and his help to overcome severe difficulties with my car is gratefully acknowledged.

During the experimental campaigns on Wendelstein 7-AS in Garching I could count on the assistance of Martin Schubert, Stefan Baeumel, Stefan Siche, Peter Böhm and Hans Scholz. I thank Nils Basse for the possibility to create backups of the experimental data (which summed up to more than 20 CDs) at his PC. Furthermore, I acknowledge the discussions on drift wave turbulence with Dr. Alexander Kendl. I would like to thank my co-doctorands Martin Schubert, Francesco Volpe, Nils Basse and Stefan Baeumel for the hospitality and the visits to the Biergarten :-).

In Greifswald I enjoyed sharing the flat with my co-doctorand Christian Franck and the discussions about various physical and technical problems and ideas. Also, Aniela Angelow should not be unmentioned for her accompany, support and bringing the bright side into life. These both and Dr. Martin Schmidt agreed to do the exhausting proof-reading. The coffee-break has been very pleasant owing to the colleagues in Greifswald.

Finally, I gratefully acknowledge the discussions on data analysis with Dr. Andreas Dinklage, Dr. Volker Naulin (Risø) and Dr. Michael Endler. I am much obliged to Prof. Dr. Thomas Klinger for the inspirations, discussions and his continuing interest from the beginning to the end of this thesis.